

POLITECNICO DI MILANO
Scuola di Ingegneria Industriale e dell'Informazione
Corso di Laurea Magistrale in Ingegneria Aeronautica



Stability of the flow in a channel with grooved wall

Relatore: Prof. Franco AUTERI

Tesi di Laurea di:
Enrico DE DONATI
matricola 813798

Anno accademico 2014 - 2015

Abstract

This work concerns the linear stability analysis of the flow in a channel with a grooved wall. The geometry of the grooves is designed in order to combine the drag reduction effects of riblets and SH surfaces. The incompressible Navier-Stokes equations, used to model the fluid, have been simplified exploiting the streamwise invariance of the problem and then linearized around the base flow solution. The system representing the eigenvalue problem has been obtained by introducing into the equations wavelike disturbances of the velocity and pressure fields. The discretization of the problem with the Finite Element Method has been performed using the FEniCS package, while the ARPACK library has been exploited to compute the eigensolutions. The results have been validated by comparison with the solution of the Orr-Sommerfeld equation. The critical Reynolds number of the flow in a channel with rectangular and triangular grooves of different amplitude and wavelength has been identified. It has been found that both geometries promote instability with greater intensity as the wall roughness increases. Approximate neutral curves have been drawn for the least stable mode. A qualitative analysis of the base flow over a fully SH surface has also been performed. The interface between the two fluids, air and water, has been modelled with the Young-Laplace equation, which has been solved numerically combining a shooting method with a Newton iterative method.

Keywords: linear stability analysis, hydrodynamic instability, channel flow, Navier-Stokes, Young-Laplace, superhydrophobic surfaces, riblets, grooves, FEniCS

Sommario

Questo lavoro riguarda l'analisi di stabilità lineare della corrente in un canale con una parete scanalata. La geometria delle scanalature è definita in modo da combinare gli effetti di riduzione di resistenza delle riblets e delle superfici SH. Le equazioni di Navier-Stokes incomprimibili, utilizzate per modellare il fluido, sono state semplificate sfruttando l'invarianza del problema nella direzione lungo la corrente e successivamente linearizzate attorno alla soluzione del flusso base. Si è ricavato il sistema che rappresenta il problema agli autovalori inserendo nelle equazioni perturbazioni ondulatorie dei campi di velocità e pressione. Il problema è stato poi discretizzato con il metodo degli Elementi Finiti utilizzando il pacchetto FEniCS e le autosoluzioni sono state calcolate sfruttando le funzionalità della libreria ARPACK. La soluzione dell'equazione di Orr-Sommerfeld ha costituito il riferimento per la validazione del programma. Si è calcolato il numero di Reynolds critico della corrente in un canale con scanalature rettangolari e triangolari di diversa ampiezza e lunghezza d'onda osservando che entrambe le geometrie favoriscono l'instabilità, in misura maggiore all'aumentare della rugosità della parete. Sono state anche tracciate le curve neutre approssimate per il modo meno stabile. Si è inoltre portata a termine un'analisi qualitativa del flusso base sopra una parete completamente SH. L'interfaccia tra i due fluidi, aria e acqua, è stata modellata con l'equazione di Young-Laplace, risolta numericamente combinando un metodo di shooting con un metodo iterativo di Newton.

Parole chiave: analisi di stabilità lineare, instabilità idrodinamica, corrente nel canale, Navier-Stokes, Young-Laplace, superfici superidrofobiche, riblets, scanalature, FEniCS

I wish to thank my supervisor, Professor Franco Auteri, for the time he dedicated to me and for his precious and attentive guidance throughout this work. I could appreciate the breadth of his knowledge and the value of his teaching ability. I also would like to thank Stefano Pedraglio for his essential help in the development of the code. I wish to thank all my friends who shared with me all these years at Politecnico, particularly Alessandro, Luca and Francesca, with whom I started my academic career. I also wish to thank Paolo for all the numerous beneficial discussions and Nicola and Matteo for their long and precious friendship since high school. A special thanks goes to my family that always supported me in every decision made during these years.

Je voudrais remercier aussi Francesco et Marco du Politecnico di Torino, Simone, Emanuele, Valerio et Francesca de l'Università La Sapienza et Yoshiaki du Kyushu Institute of Technology pour un année exceptionnel au Supaero de Toulouse, le soutien réciproque pendant ce parcours difficile et pour le fructueux échange des idées. Un remerciement particulier va au M. le professeur Eric Poquillon.

Contents

1	Introduction	13
1.1	Wetting dynamics of superhydrophobic surfaces	15
1.2	Possible applications of SH surfaces	17
1.3	Stability of the flow over riblets	19
1.4	The present work	21
2	Mathematical formulation	23
2.1	Navier-Stokes equations	23
2.1.1	Boundary conditions	24
2.1.2	Base flow	24
2.1.3	Linearization of the Navier-Stokes equations	25
2.2	Linear stability analysis	26
2.3	Young-Laplace equation	27
2.3.1	Approximation without gravity	28
2.3.2	Complete equation	29
2.4	Dimensional analysis	30
3	Numerical formulation	33
3.1	Solution of the Young-Laplace equation	33
3.2	Finite Element Method	36
3.3	Eigenvalue problem for the water flow	38
3.4	Software architecture	39
3.4.1	FEniCS library	39
3.4.2	Other libraries	40
4	Validation of the code	41
4.1	Poisson problem	41
4.1.1	Poiseuille flow	42
4.1.2	Poisson problem with two subdomains	43
4.1.3	Test with air bubble	46
4.2	Eigenvalue problem	46
4.2.1	Eigensolutions	46
4.2.2	Sensitivity to channel width and mesh refinement	49
5	Results	53
5.1	Eigenvalue tracking	53
5.2	Flow in a channel with SH geometry	56

5.2.1	Boundary layer analogy	56
5.2.2	Rectangular grooves	57
5.2.3	Triangular grooves	59
5.3	Neutral curve	59
5.4	Eigenfunctions	64
5.5	SH channel base flow	71
6	Conclusions and future work	75
A	Orr-Sommerfeld equation	79
B	UFL code	81
C	Estratto in italiano	83
C.1	Formulazione matematica	83
C.2	Formulazione numerica	84
C.3	Validazione	84
C.4	Risultati e conclusioni	85
	Bibliography	87

List of Figures

1.1	Examples of drag reduction applications.	13
1.2	Water droplets on lotus leaf.	14
1.3	Contact angle for different surfaces. Hydrophobic surface $\theta > 90^\circ$, hydrophilic surface $\theta < 90^\circ$	16
1.4	Wenzel (a) and Cassie (b) wetting states. Figure taken from Latthe <i>et al.</i> [25].	16
1.5	Variation of the growth rate of disturbances as function of the grooves amplitude S_L , disturbance streamwise wavenumber $\delta = 1.02$ and $Re = 6500$. Figure taken from Moradi and Floryan [32].	20
1.6	Neutral curves in the $(Re - \delta)$ plane. Groove wavenumbers $\beta = 0.2, 4.22, 10$ respectively. Figure taken from Moradi and Floryan [32].	20
2.1	Geometry of the problem and reference system.	25
2.2	Air bubble equilibrium.	28
2.3	Geometric parameters of a channel with rectangular grooves.	30
2.4	Geometric parameters of a channel with triangular grooves.	30
3.1	Solution for half of the groove obtained with the <i>Mathematica</i> software. . .	35
3.2	Bubble interface visualized inside a groove of unitary span.	35
4.1	Comparison of the computed flow with the analytical solution of the Poiseuille flow.	42
4.2	Solution to the Poisson equation for the water flow with only one subdomain.	44
4.3	Solution to the Poisson equation for the water flow computed in two subdomains.	44
4.4	Comparison between the velocity profiles of the water flow in the grooved channel obtained with a single or two subdomains. The black dashed line shows the fake interface location.	45
4.5	Comparison between the velocity profiles of the water flow without air bubble and with air bubble. The black dashed line shows the interface location.	45
4.6	Comparison of the eigenvalues spectrum computed with the Orr-Sommerfeld software and the software developed for the present work.	47
4.7	Comparison of the real part of the eigenfunction \hat{v} computed with the Orr-Sommerfeld software and the software developed for the present work. . . .	48

4.8	Comparison of the imaginary part of the eigenfunction \hat{v} computed with the Orr-Sommerfeld software and the software developed for the present work.	48
4.9	Eigenvalue spectra computed with different channel-section widths. Shift ξ_A and $k = 100$	50
4.10	Eigenvalue spectra computed with different shifts. Channel with $L = 0.5$ and $k = 100$	50
4.11	Value of the growth rate of the dominant eigenvalue computed with different meshes.	51
4.12	Value of the phase velocity of the dominant eigenvalue computed with different meshes.	51
5.1	Dominant eigenvalue for rectangular grooves of different amplitude and $\lambda = 0.02$. $Re = 5772$ and $\kappa = 1.02$	54
5.2	Dominant eigenvalue for triangular grooves of different amplitude and $\lambda = 0.01$. $Re = 5772$ and $\kappa = 1.02$	54
5.3	Growth rate of the dominant eigenvalue as a function of the wall roughness. $Re = 5772$ and $\kappa = 1.02$	55
5.4	Phase speed of the dominant eigenvalue as a function of the wall roughness. $Re = 5772$ and $\kappa = 1.02$	55
5.5	Eigenvalue spectra for the channel flow with longitudinal rectangular grooves for different roughness values.	60
5.6	Eigenvalue spectra for the channel flow with longitudinal triangular grooves for different roughness values	61
5.7	Growth rate of the most unstable eigenvalue as a function of the Reynolds number for several roughness values. Rectangular grooves. $\kappa = 1.02$	62
5.8	Growth rate of the most unstable eigenvalue as a function of the Reynolds number for several roughness values. Triangular grooves. $\kappa = 1.02$	62
5.9	Neutral curve in the $(Re - \kappa)$ plane for rectangular grooves of roughness $d = 0.02$ and $d = 0.05$. The black dashed line represents the approximate neutral curve of the channel with smooth walls.	63
5.10	Neutral curve in the $(Re - \kappa)$ plane for triangular grooves of roughness $d = 0.02$ and $d = 0.05$. The black dashed line represents the approximate neutral curve of the channel with smooth walls.	63
5.11	Profile of the normalized wall-normal component \bar{v}_r taken at the midspan line of the section. Rectangular grooves (blue) and triangular grooves (red). Roughness $d = 0.01$ (dotted line), $d = 0.02$ (dashed line), $d = 0.05$ (solid line), $d = 0.1$ (dashed-dotted line). The black dashed line shows the groove-tip height.	65
5.12	Profile of the normalized streamwise component \bar{w}_r taken at the midspan line of the section. Rectangular grooves (blue) and triangular grooves (red). Roughness $d = 0.01$ (dotted line), $d = 0.02$ (dashed line), $d = 0.05$ (solid line), $d = 0.1$ (dashed-dotted line). The black dashed line shows the groove-tip height.	65
5.13	Magnitude of the normalized eigenfunction $\bar{\mathbf{u}}_r$. Rectangular grooves with $d = 0.01$ and $\lambda = 0.02$	66

LIST OF FIGURES

5.14	Magnitude of the normalized eigenfunction $\bar{\mathbf{u}}_{\mathbf{r}}$. Rectangular grooves with $d = 0.02$ and $\lambda = 0.04$	66
5.15	Magnitude of the normalized eigenfunction $\bar{\mathbf{u}}_{\mathbf{r}}$. Rectangular grooves with $d = 0.05$ and $\lambda = 0.1$	67
5.16	Magnitude of the normalized eigenfunction $\bar{\mathbf{u}}_{\mathbf{r}}$. Rectangular grooves with $d = 0.1$ and $\lambda = 0.2$	67
5.17	Magnitude of the normalized eigenfunction $\bar{\mathbf{u}}_{\mathbf{r}}$. Triangular grooves with $d = 0.01$ and $\lambda = 0.01$	68
5.18	Magnitude of the normalized eigenfunction $\bar{\mathbf{u}}_{\mathbf{r}}$. Triangular grooves with $d = 0.02$ and $\lambda = 0.02$	68
5.19	Magnitude of the normalized eigenfunction $\bar{\mathbf{u}}_{\mathbf{r}}$. Triangular grooves with $d = 0.05$ and $\lambda = 0.05$	69
5.20	Magnitude of the normalized eigenfunction $\bar{\mathbf{u}}_{\mathbf{r}}$. Triangular grooves with $d = 0.1$ and $\lambda = 0.1$	69
5.21	Normalized eigenfunction components \bar{u}_r , \bar{v}_r and \bar{w}_r for rectangular and triangular grooves with $d = 0.1$ near the grooved wall.	70
5.22	Spanwise stations reference used for plotting the velocity profiles for rectangular grooves.	71
5.23	Spanwise stations used for plotting the velocity profiles for triangular grooves.	71
5.24	Velocity profiles in a channel with SH rectangular grooves. Profiles taken at station V (blue solid line) and station T (cyan dashed line). The black dashed line shows the grooves tip height.	72
5.25	Velocity profiles in a channel with SH triangular grooves. Profiles taken at station V (blue solid line) and station T (cyan dashed line). The black dashed line shows the grooves tip height.	72
5.26	Magnification of the velocity profiles near the grooved wall (rectangular grooves). Comparison between the single-phase flow (red) and the multi-phase flow (blue). Profiles taken at station V (solid line), station H (dashed-dotted line), station E (dashed line) and station T (dotted line).	73
5.27	Magnification of the velocity profiles near the grooved wall (triangular grooves). Comparison between the single-phase flow (red) and the multi-phase flow (blue). Profiles taken at station V (solid line), station E (dashed-dotted line) and station T (dotted line).	73

List of Tables

- 2.1 Buckingham theorem summary. 32
- 4.1 Characteristics of the meshes used to test the convergence of the leading eigenvalue. CPU time refers only to the eigenvalue solver and it does not take into account the CPU time needed for the base-flow computation and matrix assembly. 49
- 5.1 Average speed for different ship types and the white shark with the corresponding channel roughness. 57
- 5.2 Reference table of dimensional problems and corresponding dimensionless parameters. 58

Chapter 1

Introduction

A tremendous amount of fuel is consumed each year by both air and water vehicles and gas and liquid transmission through pipelines in order to overcome drag. This is the main reason why drag reduction is today one of the most important field of research in fluid-dynamics engineering. Even a slight decrease in drag could lead to remarkable economical returns, due to lower operational costs of pipelines and vehicles, and also to environmental benefits, due to the reduced quantity of burned fuel and emitted greenhouse gases.



(a) Submarine



(b) Pipeline

Figure 1.1: Examples of drag reduction applications.

Drag is the force produced by a fluid that counteracts the relative motion of a solid and can be divided into two main categories: pressure drag, mainly due to the body shape and relative position to the incoming flow, and skin-friction drag. In the last few years the exploitation of superhydrophobic surfaces (SH) to reduce the latter has gained increasing attention. Superhydrophobicity is obtained reducing the liquid-solid contact area by trapping gas bubbles in the blemishes of the surface roughness. The result is a composite liquid-gas-solid interface which produces lower shear stress thus reducing skin friction drag. Macroscopically, the composite interface can be described by the slippage of the flow on wall surfaces which is quantified by the slip length l : a higher slip length leads to higher slip and therefore lower shear stress. Besides skin-friction drag reduction, man-made SH surfaces have aroused interest also for various other potential applications, such as anti-icing, self-cleaning and anti-fouling.

The exploitation of SH surfaces has been inspired by nature, as often happens for technological innovations. The work of Barthlott and Neinhuis [1] explains the peculiar properties of the surface of the lotus leaf. The epidermal cells of the lotus leaf form papillae that act as a micro-structured roughness. On such papillae a very dense layer of epicuticular waxes acting as a nano-structured roughness is superimposed. By virtue of this double-hierarchical roughness, the contact angle between water droplets and the leaf is very high. If the surface is tilted, even with a slight angle, water droplets begin to roll off the leaves, and so collect and remove dirt from the surface demonstrating the self-cleaning effect. Due to this property, the lotus is considered a symbol of purity in some Asian religions. Therefore the non-sticking properties of SH surfaces have been called *Lotus effect*.

The relation between the roughness structure of the surface and its self-cleaning and water-repellency properties is confirmed by the other examples provided to us by nature. The legs of the water strider, *Gerris remigis*, have been studied with SEM techniques [18]: they are covered by numerous oriented needle-shaped setae and on each of them nanoscale grooves are evident. As a consequence of this dual-scale roughness the contact angle is very high and the leg does not pierce the water until a dimple of depth is formed allowing this insect to walk on the water surface.

Investigations on the gecko, *Lucasium steindachneri*, revealed that the particular structure of its skin has self-cleaning properties which helps with the contamination conditions that the gecko will typically encounter in its semi-arid habitat, such as cyclic exposure to soil particles, bacteria and fungi [48].



Figure 1.2: Water droplets on lotus leaf.

Mimicking the lotus leaf, further studies have demonstrated that the best water-repellent properties of the SH surfaces are obtained in the Cassie state of wetting [34]. The metastability of this wetting state increases the complexity of the problem [29] and raises the necessity of fluid-dynamics stability studies to investigate different scenarios.

One of this scenarios is the enhancement of the drag reduction effects of riblets. Riblets are longitudinal grooves on the bounding surfaces of the flow. Various studies and experiments, such as the ones performed by García-Mayoral and Jiménez [19, 20], have demonstrated beyond doubt the existence of an appreciable overall drag reduction. If we add a nano-structured roughness and fill the grooves with air, the riblets can be transformed in a SH surface, consequently improving their performance in drag reduction.

However, the development of this concept requires a preliminary in-depth study of the stability of the flow above longitudinal grooves.

This introduction is dedicated to the description of wetting dynamics of SH surfaces, well explained in reviews [2] and [38], and possible applications. Furthermore, a brief description of the available results on the stability of flow over riblets is given.

1.1 Wetting dynamics of superhydrophobic surfaces

When a drop of water is placed on a solid surface, a sessile drop forms in a shape similar to a sphere sectioned by the solid wall. The process of wetting is the spreading of liquid onto the solid surface: its dynamics is determined by all three materials involved, i.e. the solid, the liquid and the gas. The contact angle θ is defined as the angle between the solid-liquid and the liquid-gas interfaces, measured in the liquid. It is the main parameter used to describe wetting properties of a system. The surface is considered *superhydrophobic* if $\theta > 150^\circ$, otherwise is considered hydrophobic only if $\theta > 90^\circ$ and hydrophilic if $\theta < 90^\circ$.

The contact angle is determined by the balance of the forces acting on the three-phase contact line, that can be macroscopically considered the region including molecules of all three phases. It is important to underline that the following considerations are valid only in the static situation, that is when the spreading of the liquid has reached an equilibrium state. The description of the dynamic problem is much more complex and requires the introduction of a specific mathematical model, as well explained by Shikhmurzaev [43].

In the static situation, the forces acting on the three-phase contact line are the surface tensions associated with the three interfaces of the problem, that is solid-liquid, solid-gas and liquid-gas. Surface tension can be interpreted as a two-dimensional equivalent of pressure that acts to contract the interface. The surface tension coefficient γ represents the magnitude of the force per unit length acting on a line. Introducing γ_{SG} , γ_{LG} and γ_{SL} , the three surface tensions, the static contact angle is determined by the Young equation:

$$\gamma_{SG} = \gamma_{LG} \cos \theta + \gamma_{SL}. \quad (1.1)$$

Gao and McCarthy [17] stress the fact that surface tension is often confused with the surface free energy, which can be considered the work required to increase the surface area. In an equilibrium state these two quantities are mathematically equivalent but they must not be thought as interchangeable.

The definition of superhydrophobicity based only on the static contact angle is not sufficient to identify the surfaces of interest for the present research. In particular, we are interested in those surfaces capable, like the lotus leaf, of lowering the ability of drops to stick to surface itself and therefore causing their rolling off even with a slight inclination.

The non-sticking properties of the surface depend strongly on the roughness morphology and can be observed through the contact angle hysteresis. When a solid surface is tilted, a liquid drop on it starts to move, with an advancing contact line (downhill) and a receding contact line (uphill) at the same time. Before the actual rolling over begins, the shape of the drop is deformed: on the downhill side the maximum contact angle is reached while on the uphill side the contact angle tends to its minimum value [16]. The contact angle hysteresis is the difference between the maximum contact angle, or advancing contact angle, and the minimum contact angle, or receding contact angle. Non-adhesiveness of the surface is associated with low contact angle hysteresis.

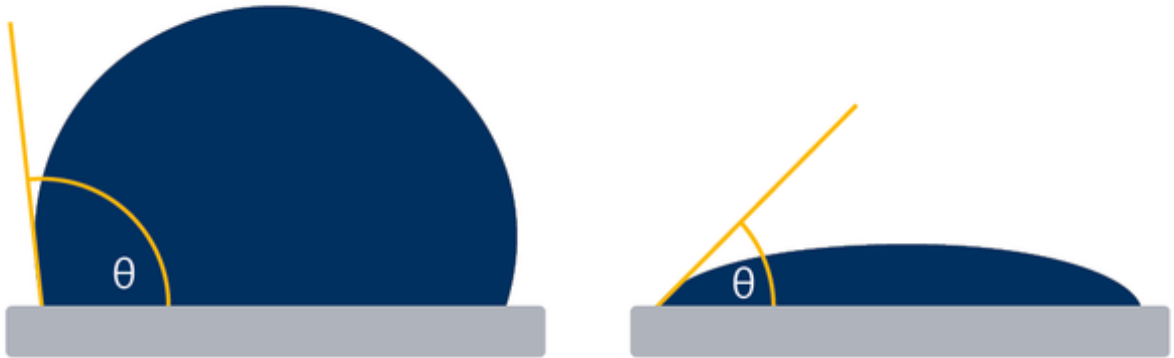


Figure 1.3: Contact angle for different surfaces. Hydrophobic surface $\theta > 90^\circ$, hydrophilic surface $\theta < 90^\circ$.

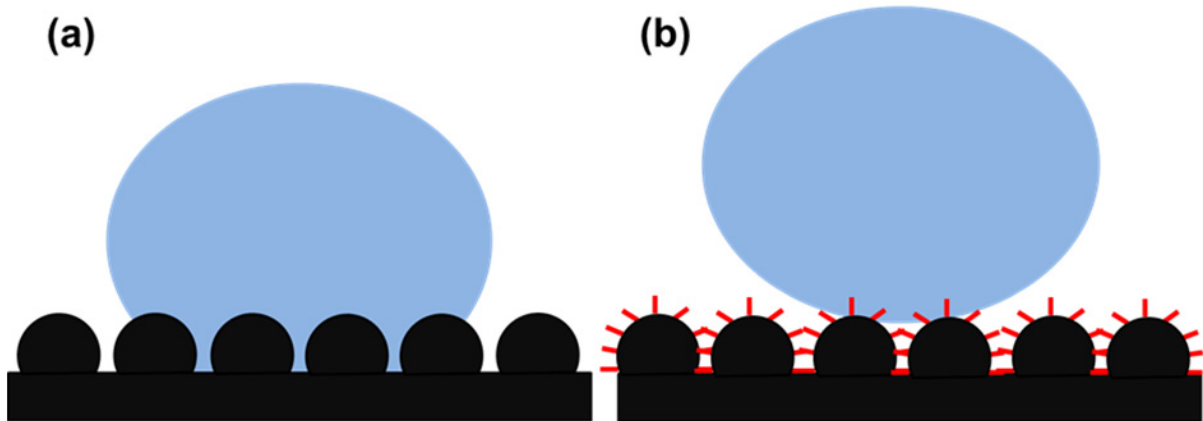


Figure 1.4: Wenzel (a) and Cassie (b) wetting states. Figure taken from Latthe *et al.* [25].

There are two wetting states water drops can assume on SH surfaces. In the Wenzel state, the surface is completely wetted and the droplet pins to the surface, whereas in the Cassie state, the droplet wets the surface only partially and air pockets form between the surface and the water droplet.

It has been demonstrated that the desired non-sticking properties of SH surfaces appear in the Cassie state of wetting, which can be obtained by replicating the structure of the lotus leaf with a double-hierarchical roughness [34]. The micro-structured roughness is required to trap air bubbles, on the other hand the nano-structured roughness enhances the static contact angle and reduces its hysteresis [26].

Unfortunately, the Cassie state of wetting on SH surfaces is metastable [29], therefore it exists a critical pressure for which there is a forced irreversible transition to the Wenzel state. Sheng and Zhang [42] examined the transition of the air layer on an immersed lotus surface. The hydraulic pressure must be kept under the critical value to guarantee the low-friction properties of SH surfaces immersed in water. The main function of the double-hierarchical roughness is increasing the energy barrier between these two states, therefore increasing the stability of the Cassie state [49].

The main difficulty to transfer these results into engineering applications relies in the present lack of efficient fabrication methods for superhydrophobic surfaces with a stable Cassie state of wetting.

1.2 Possible applications of SH surfaces

Inspired by the lotus-leaf structure, many fabrication methods for SH surfaces have been developed during the last few years. However, although effective in enhancing the rolling motion of the droplets, they were not properly designed to increase the effective slip of liquids flowing on the surface. Lee and Kim [26] explained that every manufacturing method aimed at the production of SH surfaces with low skin-friction drag must satisfy two requirements. First, nano-structures must be imposed into the micro-structures. Second, nano-structures must not affect geometrical parameters other than increasing the contact angle. Lee and Kim were successful in achieving the objectives about slip length and contact angle maintaining a stable condition by generating nano-structures only on the sidewalls, thus preserving the geometrical parameters of the micro-structure.

SH surfaces have seen growing interests in the last few years mainly for their potential application in aeronautical and naval industries for drag reduction. Zhang *et al.* [51] carried out an interesting experiment where they compared the underwater speed of two types of submarine models, normal and treated with a superhydrophobic coating. For the same power supply, the average velocities of the superhydrophobic submarine were always higher.

In addition to drag reduction, in naval industry, SH surfaces could be exploited for solving the biofouling phenomena, which is a problem of significant importance. Biofouling is the bio-accumulation of marine organisms on the surface of submerged or semi-submerged objects, both artificial and natural. It is inevitable because the marine environment has a unique bio-diversity. The process can be divided into different stages, from accumulation of dissolved organic materials to the growth of macro-algal and animal fouling [24]. As a consequence of biofouling, the shaft power required to push a ship at a certain speed increases with respect to the clean configuration or, on the other hand, for the same power

the speed that can be reached is lower. With his experiments, Schultz [41] found that the resistance penalty increases with the severity of fouling up to 89% for heavy calcareous fouling compared to a smooth hull. The application of anti-fouling (AF) is therefore a necessity and maintenance is required since a deteriorated coating can also induce resistance penalty. In the 1960s the self-polishing copolymer tributyl tin (TBT) paints were introduced and they have been used until the 2000s due to their perfect anti-fouling ability and their durability. However TBT paints have been discovered to be highly toxic even in low concentrations and to be persistent in the marine environment. Eventually TBT have received a worldwide ban on their application on ship hulls in 2003. This is the reason why alternative, environmental-friendly, effective anti-fouling systems are being sought for the last few years. SH surfaces may represent an appealing solution to this problem.

SH surfaces could be exploited also in another important problem affecting the aeronautical and naval transportation, that is icing. Icing is caused by the impact of super-cooled water droplets onto a solid surface and it is notorious for the rupture of power lines and the stall of aircraft wings. Until now the research on anti-icing systems focused on the removal of already formed ice. Indeed, currently used ice removal techniques are effective but require a power supply. The experiments of Cao *et al* [8] demonstrated that SH surfaces could be used as a passive anti-icing device by reducing or eliminating water accumulation on the solid surface before water freezes. Further studies have been carried out by Boinovich and Emelyanenko [5] which focused on the delay of frost formation on SH surfaces and on the durability of the icephobic properties of SH coatings. However, all these researches have been carried out under natural freezing environments or in climate-controlled rooms. In their experiments, Wang *et al* [46] added an important factor present in the actual freezing weather conditions of operating aircraft or power lines during rainstorms: the wind action. The SH coating showed anti-icing properties depending on the temperature and the wind velocity. The studies on anti-icing properties of SH surfaces seem promising, nevertheless Farhadi *et al* [13] observed significant limitations about the durability and their performance in humid conditions. After many icing/de-icing cycles, the anti-ice performance of the coatings deteriorates and when water condenses on surface roughness, SH surfaces lose their ice-repellency. Given all these considerations, further research is required before SH surfaces can be considered valuable candidate to develop passive anti-icing systems.

Apart from these problems in the transportation industry, SH surfaces have the chance to be employed in diverse, but not less worthy of attention, projects. Yan *et al* [50] successfully developed a miniature water-walking robot mimicking the locomotion system of the water strider. The tested prototype was able to stably walk quickly and make turns at different gaits on the water surface justifying the recent interest in the design of micro/miniature water-walking robots and their potential to carry out different aquatic tasks such as water quality monitoring or aquatic search and rescue.

All the possible applications described so far focus on the exploitation of the water-repellency aspect of SH surfaces. It is also interesting to investigate the possible applications derived from the self-cleaning aspect of man-made surfaces which mimic the lotus leaf [3]. In biotechnology, one is interested in controlling droplets containing biologically relevant molecules; because droplets on SH surfaces have very low contact area they can easily be moved with an external field, for example electrical, thus making possible the development of droplet-based actuation mechanisms. Other more practical applica-

tions take place in the household-commodity sector introducing self-cleaning windows or graffiti-resistant house walls. The main problem yet to be overcome is the durability: in outdoor applications the surfaces lose their self-cleaning properties too rapidly to justify the higher initial investment.

1.3 Stability of the flow over riblets

The drag reducing properties of riblets are nowadays clear and indisputable. The overall effect of the riblets is the result of two contrasting actions: a linear mechanism of drag reduction due to the different response of the grooved surface to a viscous flow and a nonlinear mechanism of drag increase mediated by a growth of the characteristic scale of turbulence. While the first effect is quantitatively predictable on a theoretical basis, the second effect is more complicated to predict due to insufficient knowledge on how riblets influence flow stability and transition.

Luchini and Trombetta [28] discovered that the effect of the grooves upon a two-dimensional instability can be represented by boundary conditions of the inner problem applied in the equivalent origin of the y -axis. The evolution of the Tollmien-Schlichting waves can still be described through the standard Orr-Sommerfeld equation, with modified boundary conditions and modified velocity profile. The effect of the riblets is a reduction of both critical and transition Reynolds number, therefore the instability is promoted and not retarded. The drag reduction cannot be attributed to retardation of transition but rather do a direct effect on the developed turbulent flow. Luchini and Trombetta also tried to understand if the evolution of the instability waves is exerted by the modification of the mean flow or by effect of the modified boundary condition. They discovered that the effect of the boundary condition produces critical Reynolds numbers similar to the total ones and that the effect of the mean flow is smaller and of the opposite sign. Therefore the slight increase of instability can be ascribed to a balance of the destabilizing effect of the excess flow rate and stabilizing effect of the changed mean flow profile.

Following the studies of Luchini and Trombetta, Ehrenstein [12] investigated the stability of the flow over semicircular riblets and confirmed that the laminar channel flow over riblets is more unstable than the Poiseuille profile with smooth walls. Using a Chebyshev collocation to discretize the linearized Navier-Stokes equations and the Arnoldi's method to compute the eigenvalues, he found that the deepest riblets have the most unstable eigenvalues. Even though the spanwise component of the perturbation is very small, it is not negligible inside the grooves and hence the primary instability mechanism is responsible for the appearance of spanwise periodic patterns.

The study of Moradi and Floryan [32] confirmed Ehrenstein results and showed that the role of the grooves in the instability process depends on their shape and amplitude. In particular, studying sinusoidal grooves, they found that the grooves may either stabilize or destabilize the flow depending on the groove wavenumber, with transition occurring at $\beta \approx 4.22$ and being independent on the groove amplitude.

The geometry of the grooves and the disturbances superposed on the base flow have been expressed in terms of Fourier series, therefore an analysis of how many Fourier modes needed in the numerical solution was necessary. The eigenvalue problem has been solved with various techniques.

All the results described above were obtained with the disturbance wavenumber $\delta =$

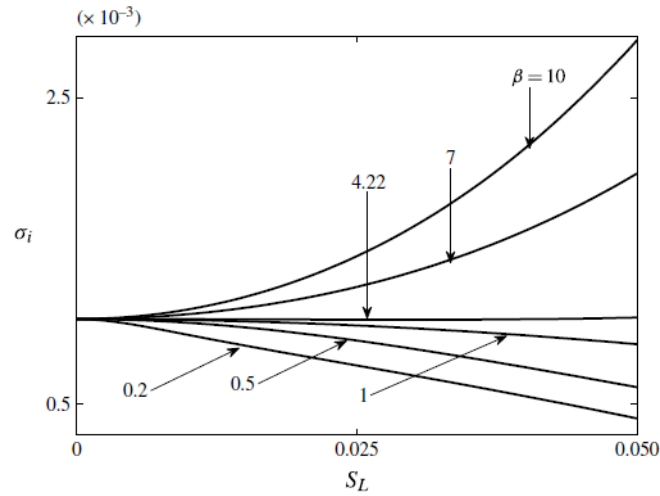


Figure 1.5: Variation of the growth rate of disturbances as function of the grooves amplitude S_L , disturbance streamwise wavenumber $\delta = 1.02$ and $Re = 6500$. Figure taken from Moradi and Floryan [32].

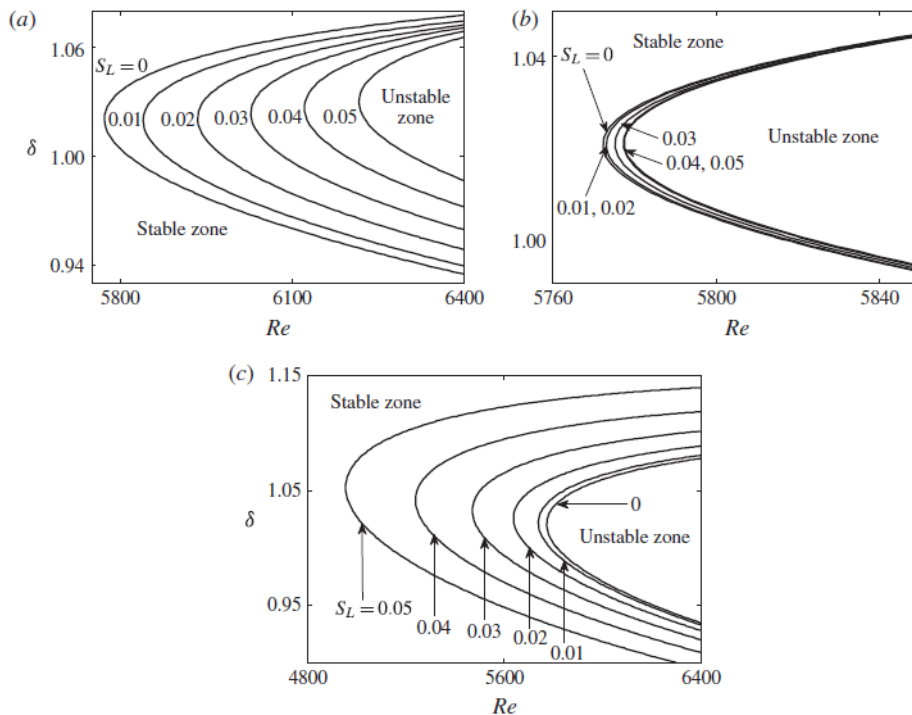


Figure 1.6: Neutral curves in the $(Re - \delta)$ plane. Groove wavenumbers $\beta = 0.2, 4.22, 10$ respectively. Figure taken from Moradi and Floryan [32].

1.02 (denoted κ in the present work), which is the critical wavenumber in a plane channel. Mohammadi *et al.* [31] discovered a new instability mode for the grooved channel, triggered with disturbances of wavenumber $\delta = 0.3$. With disturbances of this kind, the most unstable eigenvalue moves from the A branch to the P branch of the spectrum. Moreover, its location is strongly affected by the groove amplitude. It has been demonstrated that the growth rate becomes independent from the Reynolds number, once Re is large enough, therefore this instability mode must be driven by an inviscid mechanism. The velocity field corresponding to this mode is made up of rows of counter-rotating rolls oriented across the channel and propagating streamwise.

1.4 The present work

The present work is aimed to investigate the influence of longitudinal grooves on the development of hydrodynamic linear instabilities in the flow in a plane channel. The motivation lies in the effort of designing a surface that combines the drag reduction effects of riblets and SH surfaces. To this end, grooves of different shapes have been taken into consideration. The rectangular grooves represent the geometry typical of SH surfaces while the riblets are usually made of triangular grooves. Their dimension has been chosen so that they are able to trap an air bubble with high contact angles θ . A linear stability analysis of the single-phase problem with only water has been carried out. We mainly focused on locating the critical Reynolds number for grooves of different shape and dimension and on investigating how the amplitude of the grooves affects the growth rate of the dominant eigenvalue. In addition, for some of the geometries considered, the approximate neutral curve in the $(Re - \kappa)$ has been drawn. The analysis has been completed with the visualization of the normalized eigenfunctions. The results obtained constitute a solid knowledge base to interpret the results for the complete multi-phase problem with air bubbles. Moreover, a qualitative analysis of the base flow for the complete problem has also been performed, even though the present work mainly concerns the single-phase problem.

The flow has been described with the incompressible Navier-Stokes equations, completed with appropriate boundary conditions for the considered geometries. The configuration of the interface between water and air is determined by the Young-Laplace equation, which has been solved numerically. The discretization of the linearized Navier-Stokes equations is achieved by the application of the Finite Element Method (FEM) which, with appropriate refinement of the mesh, guarantees an adequate accuracy of the results. The boundary conditions have been imposed directly in the construction of the matrices of the linear system representing the eigenvalue problem. The code is written in mixed *C++/Fortran90* language and exploits the features of the *FEniCS*[39] package for the finite element discretization and of the *ARPACK*[27] library to solve the eigenvalue problem.

Chapter 2

Mathematical formulation

In this chapter the equations governing the flow inside a grooved channel are presented. The simplifications allowed by the problem geometry have been applied to the dimensionless Navier-Stokes equation to obtain the system of partial differential equations describing the base flow. Particular attention has been made on the definition of the boundary conditions, considering the potential presence of an air bubble pinned inside the grooves. The Navier-Stokes have then been linearized around the base flow and, inserting the disturbance in the form of wavelike solutions, the system representing the eigenvalue problem to be solved to study the linear stability of the flow has been obtained. To complete the description of the boundary conditions, the shape of the bubble interface has been described with the Young-Laplace equation, firstly without considering the gravity and then introducing the hydrostatic term. The mathematical formulation of the problem is concluded by the definition of the involved physical parameters and a dimensional analysis with the Buckingham theorem.

2.1 Navier-Stokes equations

The dynamics of Newtonian fluids, such as air and water, at low Mach numbers is accurately described by the incompressible Navier-Stokes equations

$$\begin{cases} \frac{\partial \mathbf{u}}{\partial t} + (\mathbf{u} \cdot \nabla) \mathbf{u} - \nu \nabla^2 \mathbf{u} + \frac{\nabla P}{\rho} = \mathbf{g}, \\ \nabla \cdot \mathbf{u} = 0, \end{cases} \quad (2.1)$$

where \mathbf{u} , ρ and P are the fluid velocity, density and pressure respectively; \mathbf{g} is an external force field, for example gravity, and t is time.

For our purposes, it is more useful to treat these equations in their dimensionless form. Choosing appropriate length and speed scales, the system (2.1) becomes

$$\begin{cases} \frac{\partial \mathbf{u}}{\partial t} + (\mathbf{u} \cdot \nabla) \mathbf{u} - \frac{1}{Re} \nabla^2 \mathbf{u} + \nabla P = \mathbf{g}, \\ \nabla \cdot \mathbf{u} = 0, \end{cases} \quad (2.2)$$

where, with a slight notation abuse, \mathbf{u} , P and \mathbf{g} are now the dimensionless velocity, pressure and external force field respectively. The equivalence of the dimensionless results

obtained for two problems with the same geometry and different scales, is the matching of the non-dimensional quantity Re , the Reynolds number. The Reynolds number can be thought of as the ratio between the inertial forces and the viscous forces acting in the fluid, and is expressed by

$$Re = \frac{UL}{\nu}, \quad (2.3)$$

where U , L are respectively the speed and length scales used to obtain the dimensionless form of the Navier-Stokes equations and $\nu = \frac{\mu}{\rho}$ is the kinematic viscosity of the fluid.

2.1.1 Boundary conditions

The system of PDEs must be completed with appropriate boundary conditions. In the present case the flow geometry is shown in figure 2.1.

For water we must impose the no-slip condition on both Γ_{up} and Γ_{down} delimiting the channel while for air the same no-slip condition must be imposed for Γ_{groove} , that is the wall of the groove. The dashed lines mean that this geometry is repeated in the xy plane, therefore we must impose the periodicity condition on the velocity field, $\mathbf{u}|_{\Gamma_{left}} = \mathbf{u}|_{\Gamma_{right}}$. On the interface between the fluids we impose the equality of the velocities of the two fluids, the equality of the stresses along the two tangential directions and the Young-Laplace equation for the stress normal to the surface, which will be described in detail in Section 2.3. Summarizing, all the boundary conditions are:

$$\left\{ \begin{array}{ll} \mathbf{u}|_{\Gamma_{left}} = \mathbf{u}|_{\Gamma_{right}}, & \\ \mathbf{u}^w = 0 & \mathbf{x} \in \Gamma_{up} \cup \Gamma_{down}, \\ \mathbf{u}^a = 0 & \mathbf{x} \in \Gamma_{groove}, \\ \mathbf{u}^w = \mathbf{u}^a & \mathbf{x} \in \Gamma_{bubble}, \\ \sigma_{\mathbf{t}_{xy}}^w = \sigma_{\mathbf{t}_{xy}}^a & \mathbf{x} \in \Gamma_{bubble}, \\ \sigma_{\mathbf{t}_z}^w = \sigma_{\mathbf{t}_z}^a & \mathbf{x} \in \Gamma_{bubble}, \\ \sigma_{\mathbf{n}}^w - \sigma_{\mathbf{n}}^a = \frac{\gamma}{r} & \mathbf{x} \in \Gamma_{bubble}. \end{array} \right. \quad (2.4)$$

The superscript w refers to water and the superscript a to air. \mathbf{n} represents the vector normal to the interface between the fluids and it lies on the xy plane. \mathbf{t}_{xy} represents the tangential vector that lies on the same plane as \mathbf{n} while \mathbf{t}_z is the second tangential vector, perpendicular to the xy plane.

2.1.2 Base flow

The base flow considered for the problem shown in figure 2.1 is a steady flow with a single non-zero component, the z -component. Furthermore, the flow must be invariant in the z direction so that the section xy can be chosen arbitrarily. According to these considerations, the velocity field of both air and water can be written in the form $\mathbf{u}(x, y) = w(x, y)\hat{\mathbf{z}}$.

To better understand the simplifications that a flow of this form introduces in the

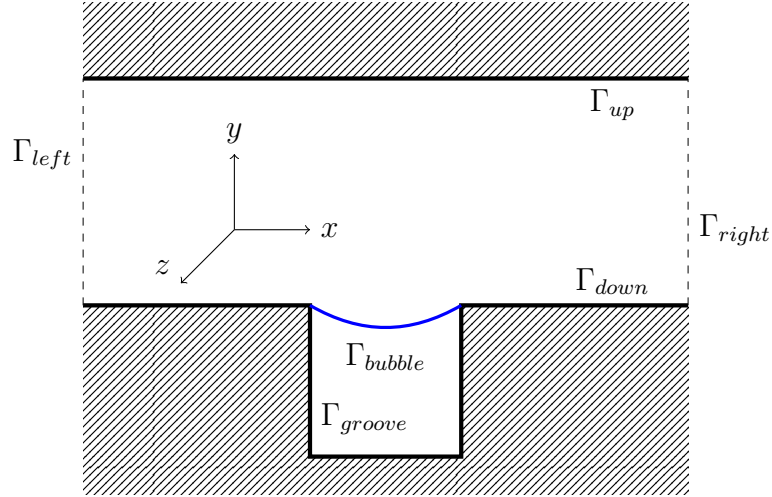


Figure 2.1: Geometry of the problem and reference system.

Navier-Stokes equations (2.2), it is better to rewrite them for each velocity component

$$\begin{cases} \frac{\partial u}{\partial t} + u \frac{\partial u}{\partial x} + v \frac{\partial u}{\partial y} + w \frac{\partial u}{\partial z} - \frac{1}{Re} \left(\frac{\partial^2 u}{\partial x^2} + \frac{\partial^2 u}{\partial y^2} + \frac{\partial^2 u}{\partial z^2} \right) + \frac{\partial P}{\partial x} = 0, \\ \frac{\partial v}{\partial t} + u \frac{\partial v}{\partial x} + v \frac{\partial v}{\partial y} + w \frac{\partial v}{\partial z} - \frac{1}{Re} \left(\frac{\partial^2 v}{\partial x^2} + \frac{\partial^2 v}{\partial y^2} + \frac{\partial^2 v}{\partial z^2} \right) + \frac{\partial P}{\partial y} = g_y, \\ \frac{\partial w}{\partial t} + u \frac{\partial w}{\partial x} + v \frac{\partial w}{\partial y} + w \frac{\partial w}{\partial z} - \frac{1}{Re} \left(\frac{\partial^2 w}{\partial x^2} + \frac{\partial^2 w}{\partial y^2} + \frac{\partial^2 w}{\partial z^2} \right) + \frac{\partial P}{\partial z} = 0, \\ \frac{\partial u}{\partial x} + \frac{\partial v}{\partial y} + \frac{\partial w}{\partial z} = 0. \end{cases} \quad (2.5)$$

The base flow discussed above allows us to impose that $u, v = 0$ and to assume that all the derivatives with respect to t and to z are null since the base flow is independent on time and on the z coordinate. The equations are therefore considerably simplified and become

$$\begin{cases} \frac{\partial P}{\partial x} = 0, \\ \frac{\partial P}{\partial y} = g_y, \\ \frac{\partial P}{\partial z} = \frac{1}{Re} \left(\frac{\partial^2 w}{\partial x^2} + \frac{\partial^2 w}{\partial y^2} \right). \end{cases} \quad (2.6)$$

The incompressibility constraint is identically satisfied. From equations (2.6) we observe that, for the base flow, there is no pressure gradient along the x direction and the pressure gradient along the y direction is only determined by the gravitational field.

2.1.3 Linearization of the Navier-Stokes equations

Once the base flow has been computed, we can analyse the behaviour of the system if a small perturbation is applied, in particular we are interested in discovering how the contact surface between air and water is deformed.

The Navier-Stokes equations (2.2) must be linearized around the base-flow solution. The velocity and pressure field are rewritten as the sum of the base flow and a perturbation, that is $\mathbf{u} = \mathbf{U} + \tilde{\mathbf{u}}$ and $P = p + \tilde{p}$.

$$\begin{cases} \frac{\partial(\mathbf{U} + \tilde{\mathbf{u}})}{\partial t} + ((\mathbf{U} + \tilde{\mathbf{u}}) \cdot \nabla)(\mathbf{U} + \tilde{\mathbf{u}}) - \frac{1}{Re} \nabla^2(\mathbf{U} + \tilde{\mathbf{u}}) + \nabla(p + \tilde{p}) = \mathbf{g}, \\ \nabla \cdot (\mathbf{U} + \tilde{\mathbf{u}}) = 0. \end{cases} \quad (2.7)$$

By dropping the second order terms in the previous equation and using the equation for the base flow, we finally obtain the final form of the linearized Navier-Stokes equations

$$\begin{cases} \frac{\partial \tilde{\mathbf{u}}}{\partial t} + (\tilde{\mathbf{u}} \cdot \nabla)\mathbf{U} + (\mathbf{U} \cdot \nabla)\tilde{\mathbf{u}} - \frac{1}{Re} \nabla^2 \tilde{\mathbf{u}} + \nabla \tilde{p} = 0, \\ \nabla \cdot \tilde{\mathbf{u}} = 0. \end{cases} \quad (2.8)$$

Since the base flow is parallel, i.e. $U, V = 0$, the previous equation can be further simplified. We can no longer assume that the flow is steady and invariant in the z direction because we do not know a priori the form of the perturbation. Rewriting equations (2.8) for each component we obtain

$$\begin{cases} \frac{\partial \tilde{u}}{\partial t} + W \frac{\partial \tilde{u}}{\partial z} - \frac{1}{Re} \left(\frac{\partial^2 \tilde{u}}{\partial x^2} + \frac{\partial^2 \tilde{u}}{\partial y^2} + \frac{\partial^2 \tilde{u}}{\partial z^2} \right) + \frac{\partial \tilde{p}}{\partial x} = 0, \\ \frac{\partial \tilde{v}}{\partial t} + W \frac{\partial \tilde{v}}{\partial z} - \frac{1}{Re} \left(\frac{\partial^2 \tilde{v}}{\partial x^2} + \frac{\partial^2 \tilde{v}}{\partial y^2} + \frac{\partial^2 \tilde{v}}{\partial z^2} \right) + \frac{\partial \tilde{p}}{\partial y} = 0, \\ \frac{\partial \tilde{w}}{\partial t} + \tilde{u} \frac{\partial W}{\partial x} + \tilde{v} \frac{\partial W}{\partial y} + W \frac{\partial \tilde{w}}{\partial z} - \frac{1}{Re} \left(\frac{\partial^2 \tilde{w}}{\partial x^2} + \frac{\partial^2 \tilde{w}}{\partial y^2} + \frac{\partial^2 \tilde{w}}{\partial z^2} \right) + \frac{\partial \tilde{p}}{\partial z} = 0, \\ \frac{\partial \tilde{u}}{\partial x} + \frac{\partial \tilde{v}}{\partial y} + \frac{\partial \tilde{w}}{\partial z} = 0. \end{cases} \quad (2.9)$$

This system must be completed with appropriate boundary conditions, which are the same as equations (2.4) but applied to the perturbation velocity field $\tilde{\mathbf{u}}(x, y, z, t)$ instead of the base flow.

2.2 Linear stability analysis

The main purpose of the present work is to evaluate the stability of the flow in a channel with longitudinal grooves. The linear stability study consists in forcing a certain solution in the linearized Navier-Stokes equations, thus obtaining the system that must be resolved with the finite elements method.

Taking as reference the results obtained for the Poiseuille flow in a plane channel available in the literature [21, 40], we focus on studying the stability of the base flow to a specific form of disturbance, that is a wavelike velocity and pressure perturbation. Such a perturbation can be written in the form

$$\tilde{\mathbf{u}}(x, y, z, t) = \hat{\mathbf{u}}(x, y) e^{\omega t + i\kappa z} \quad \tilde{p}(x, y, z, t) = \hat{p}(x, y) e^{\omega t + i\kappa z}, \quad (2.10)$$

with $\omega \in \mathbb{C}$ and $\kappa \in \mathbb{R}$. Substituting the wavelike disturbances in system (2.9) and simplifying the exponential part of each term, one obtains:

$$\begin{cases} \omega \hat{u} + i\kappa W \hat{u} - \frac{1}{Re} \left(\frac{\partial^2 \hat{u}}{\partial x^2} + \frac{\partial^2 \hat{u}}{\partial y^2} - \kappa^2 \hat{u} \right) + \frac{\partial \hat{p}}{\partial x} = 0, \\ \omega \hat{v} + i\kappa W \hat{v} - \frac{1}{Re} \left(\frac{\partial^2 \hat{v}}{\partial x^2} + \frac{\partial^2 \hat{v}}{\partial y^2} - \kappa^2 \hat{v} \right) + \frac{\partial \hat{p}}{\partial y} = 0, \\ \omega \hat{w} + i\kappa W \hat{w} + \frac{\partial W}{\partial x} \hat{u} + \frac{\partial W}{\partial y} \hat{v} - \frac{1}{Re} \left(\frac{\partial^2 \hat{w}}{\partial x^2} + \frac{\partial^2 \hat{w}}{\partial y^2} - \kappa^2 \hat{w} \right) + i\kappa \hat{p} = 0, \\ \frac{\partial \hat{u}}{\partial x} + \frac{\partial \hat{v}}{\partial y} + i\kappa \hat{w} = 0. \end{cases} \quad (2.11)$$

The system must be completed with no-slip boundary conditions at the channel walls and periodic conditions in the x direction.

The solution must be sought in an infinite-dimensional space, that is $\tilde{\mathbf{u}} \in H^1(\Omega)$. To be solved with the finite element method, the weak formulation of system (2.11) must be obtained and discretized into a finite-dimensional space. Our main interest lies into solving the temporal eigenvalue problem $\omega_j = \omega_j(\kappa)$ where the wavenumber κ is known: the spatial structure of the wavelike perturbation is unchanged and the amplitude of the wave grows or decays as time progresses, with a temporal growth rate represented by $c_r = \frac{\omega_{j,r}}{\kappa}$. Instead, $c_i = -\frac{\omega_{j,i}}{\kappa}$ represents the phase velocity with which these freely evolving waves travel. It is worth noticing that perturbations (2.10) are defined in the same way as Ehrenstein [12], which is slightly different from the definition used by Schmid and Henningson [40]. Therefore, when comparing the results, we must take into account the following relations:

$$\omega_r = \omega_i^{SH}, \quad (2.12a)$$

$$\omega_i = -\omega_r^{SH}. \quad (2.12b)$$

where $\omega^{SH} \in \mathbb{C}$ are the eigenvalues solution of the Orr-Sommerfeld equation, described in Appendix A, computed with the Schmid and Henningson notation.

2.3 Young-Laplace equation

The configuration of the interface between two fluids is determined by their pressure difference in each point of the contact surface. The equation modelling the physics of this problem is obtained studying the equilibrium of the forces acting on the surface. Figure 2.2 represent the situation, in two dimensions, of an air bubble trapped inside a solid wall groove.

In the horizontal direction the equilibrium is identically satisfied for symmetry reasons. In the vertical direction the pressure difference $\Delta P = P_A - P_H$ must be balanced by surface tension

$$\begin{aligned} \int_0^\theta \Delta P r \hat{\mathbf{n}} d\theta + \gamma = 0, \\ \Delta P \int_0^\theta \cos \tilde{\theta} r d\tilde{\theta} + \gamma \sin \theta = 0. \end{aligned} \quad (2.13)$$

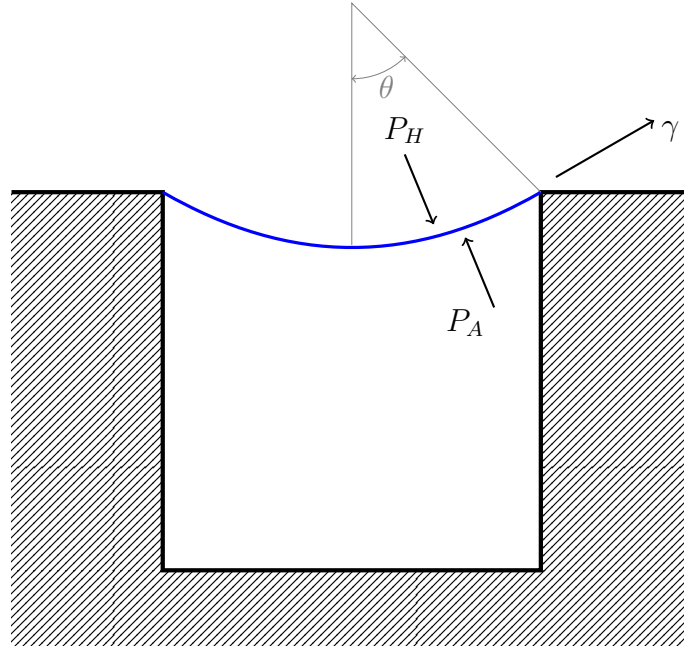


Figure 2.2: Air bubble equilibrium.

Imposing force equilibrium, we obtain the Young-Laplace equation, which relates the pressure difference between the fluids and the curvature of the contact surface. In the two-dimensional case, the contact surface reduces to a line described by one curvature radius r

$$\Delta P = \frac{\gamma}{r}. \quad (2.14)$$

In this study, the unknown is the curve describing the interface, that will be needed to compute the base flow. A plane curve can be written in the form $\mathbf{r}(x) = x\mathbf{i} + y(x)\mathbf{j}$, from which its curvature can be obtained

$$\frac{1}{r} = \frac{y''(x)}{[1 + y'(x)^2]^{\frac{3}{2}}}. \quad (2.15)$$

If (2.15) is substituted into (2.14) we obtain an ordinary differential equation for $y(x)$. This equation, being non linear and of the second order, cannot be solved in the closed form, in general. The problem can be simplified if gravity is neglected.

2.3.1 Approximation without gravity

This approximation consists in neglecting the hydrostatic pressure gradient, therefore the pressure difference between the two fluids is constant along the contact line. According to Young-Laplace equation (2.14) a constant pressure difference implies a constant curvature radius and thus the curve $y(x)$ representing the interface is a circumference arc. The ODE equation to be resolved is:

$$\frac{\Delta P}{\gamma} = \frac{y''(x)}{[1 + y'(x)^2]^{\frac{3}{2}}}. \quad (2.16)$$

By virtue of this simplification, the solution can be found analytically. For the first integration we can use the substitution $y'(x) = z(x)$ to obtain a first order, separable equation and $\frac{\Delta P}{\gamma} = \sigma$ to lighten the notation. By letting $z(x) = y'(x)$ in (2.16), we obtain

$$\frac{dz}{dx} = \sigma [1 + z(x)^2]^{\frac{3}{2}}. \quad (2.17)$$

That can be integrated immediately to give

$$\frac{z}{\sqrt{1 + z^2}} = \sigma(x + C). \quad (2.18)$$

From (2.18) the explicit expression of $y'(x)$ is obtained, which is another first order, separable equation.

$$\frac{dy}{dx} = \pm \frac{\sigma(x + C)}{\sqrt{1 - \sigma^2(x^2 + 2Cx + C^2)}}. \quad (2.19)$$

Its solution is

$$y(x) = \mp \frac{\sqrt{1 - (x + C)^2 \sigma^2}}{\sigma} + D. \quad (2.20)$$

If we place the axis origin in one of the two triple points and considering s the span of the groove, the constants of integration C and D are determined with the boundary conditions (2.21)

$$y(0) = 0, \quad y(s) = 0. \quad (2.21)$$

As predicted, the final solution is a circumference arc

$$y(x) = \frac{1}{\sigma} \left(\sqrt{1 - \frac{s^2}{4} \sigma^2} - \sqrt{1 - \left(x - \frac{s}{2}\right)^2 \sigma^2} \right). \quad (2.22)$$

In equation (2.22), the first one of the two solutions (2.20) has been considered.

2.3.2 Complete equation

The gravitational field may change the solution noticeably since the pressure difference between the two fluids at the interface can no longer be considered constant; as a consequence, the shape of the contact line is no more a circumference arc but it has a variable curvature.

The pressure of the two fluids in each point can be calculated from Stevin's law, known $g = 9.81 \text{ m/s}^2$ and the density of the fluids. Placing the reference system as described in the previous paragraph:

$$P_A = P_{A0} - \rho_A g y, \quad (2.23a)$$

$$P_H = P_{H0} - \rho_H g y. \quad (2.23b)$$

Using (2.23a) and (2.23b), the Young-Laplace equation (2.14) becomes (with ΔP defined as $\Delta P = P_{A0} - P_{H0}$ now):

$$\Delta P + (\rho_A - \rho_H) g y = \frac{\gamma}{r} \quad (2.24)$$

We finally obtain the complete ordinary differential equation for the contact line

$$y''(x) - \left(\frac{(\rho_A - \rho_H) g}{\gamma} y(x) + \frac{\Delta P}{\gamma} \right) [1 + y'(x)^2]^{\frac{3}{2}} = 0. \quad (2.25)$$

2.4 Dimensional analysis

A very important part of every engineering research is to understand which are the physical parameters governing the phenomenon under study. In the present work we ask ourselves on which parameters the linear stability characteristics of the flow depend. Eventually, with the help of dimensional analysis and of the Buckingham theorem, the physical parameters can be recast in a smaller number of dimensionless parameters, more useful to obtain results valid at different scales.

We can divide the physical parameters that control the phenomenon in two main groups: the geometric parameters and the fluid parameters. The first group includes all the parameters defining the geometry of the section and of the grooves. The second group includes the properties of the involved fluids.

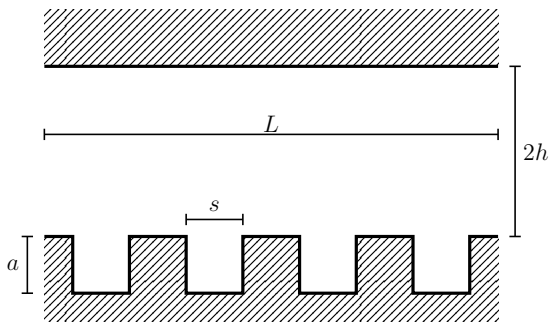


Figure 2.3: Geometric parameters of a channel with rectangular grooves.

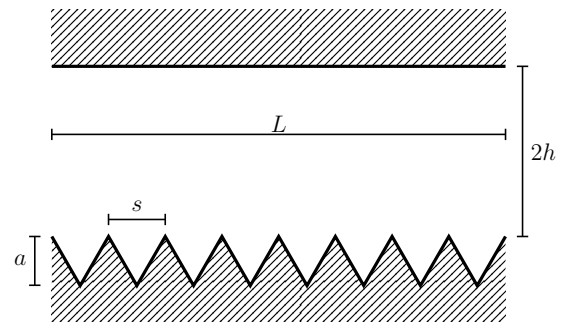


Figure 2.4: Geometric parameters of a channel with triangular grooves.

Figures 2.3 and 2.4 show the relevant dimensions defining the geometry of the channel section representing the considered domain. We can identify five parameters:

- The span of the grooves s .
- The amplitude of the grooves a ; for the triangular grooves this parameter can be substituted with the inclination of the walls (once s is defined).
- The half-height of the main channel h .
- The span of the channel section L ; it can be replaced by the number of grooves N in the considered section. The relation between N , s and L depends on the groove shape: it is $L = 2Ns$ for the rectangular grooves and $L = Ns$ for the triangular grooves.
- The contact angle measured in the air α ; it is the supplementary angle of the conventional contact angle measured in the water. We can also consider this parameter part of the fluid properties group.

The properties of the fluids include the two densities, ρ_H and ρ_A for water and air respectively, the two dynamic viscosities, μ_H and μ_A , and the surface tension γ .

The only physical parameter that does not fall into one of the two previous categories is the pressure gradient along the z direction G_z , which is imposed externally. The pressure

gradient is also important to scale the Navier-Stokes equations. Another important physical parameter is the gravity g , however in this study it is not taken into consideration, except for the calculation of the free surface with the Young-Laplace equation.

According to section 2.1, we need a reference length and a reference velocity to obtain the dimensionless form of the equations. In literature [40], the common choices for a parallel flow in a plane channel are the channel half-height $h = \frac{H}{2}$ and the centre-line velocity U_{cl} , which is expressed by

$$U_{cl} = -\frac{G_z h^2}{2\mu_H}. \quad (2.26)$$

To obtain coherent results, for this study we choose the same references. The only difference is that the centre-line velocity U_{cl} is not exactly the maximum velocity, as it is in the parallel flow in a plane channel, invariant in the x and z directions. In the present study, the flow is invariant only in the z direction, due to the cavities or riblets. Therefore U_{cl} should be interpreted as the equivalent centre-line velocity of a plane channel of the same half-height h .

From equation (2.26), it must be noticed that the centre-line velocity $U_{cl} = U_{cl}(G_z)$ depends on the pressure gradient, therefore it is not an independent physical parameter. By setting the pressure gradient, and choosing the appropriate channel height, we are also indirectly imposing the centre-line velocity.

The Buckingham theorem states that $p = n - k$ dimensionless parameters can be obtained in a problem featuring n physical variables and k physical dimensions. In the present case, the physical variables are the properties of the two fluids, the dimension defining the geometry and the pressure gradient for a total of $n = 11$. The fundamental physical dimensions involved are only three (thus $k = 3$): length, time and mass. According to Buckingham's theorem, we should be able to find $p = 8$ dimensionless parameters. The first four parameters are purely geometrical and correspond to the aspect ratio of the considered section, the dimensionless wavelength of the grooves, the ratio between the amplitude of the grooves and the channel half-height, which can be interpreted as the roughness of the channel wall, and the contact angle which is already a dimensionless variable itself. We can then write:

$$\pi_1 = AR = \frac{L}{h}, \quad \pi_2 = \lambda = \frac{2s}{h}, \quad \pi_3 = d = \frac{a}{h}, \quad \pi_4 = \alpha. \quad (2.27)$$

As an alternative, we can consider the groove wavenumber $\beta = \frac{2\pi}{\lambda}$ instead of the groove wavelength. The groove wavelength is defined differently depending on the shape. The relation for λ shown in (2.27) is valid for the rectangular grooves. For the triangular ones it is $\lambda = \frac{s}{h}$. Furthermore, in all the results regarding triangular riblets, the roughness d is actually $d = \frac{2}{\sqrt{3}} \frac{a}{h}$, in order to obtain values directly comparable with the rectangular grooves while preserving the equilateral triangle shape of their section.

The other four parameters depend on the properties of the two fluids. The most important is the Reynolds number, essential to understand the fluid behaviour and the flow stability. Since water is the prevalent fluid, it is natural to define the Reynolds number based on the water properties (density and viscosity); the reference length and velocity are h and U_{cl} , used to scale the Navier-Stokes equations. The problem involves the interaction between two immiscible fluids therefore we can also define a Weber number,

Physical parameters	Dimensions	Dimensionless parameters
L	l	
h	l	AR
s	l	λ or β
a	l	d
α	-	α
ρ_H	ml^{-3}	
ρ_A	ml^{-3}	Re_h
μ_H	$ml^{-1}t^{-1}$	We
μ_A	$ml^{-1}t^{-1}$	m
γ	mt^{-2}	η
G_z	$ml^{-2}t^{-2}$	
11	3	8

Table 2.1: Buckingham theorem summary.

which represents the ratio of inertial force to surface tension force. In this case it is natural to take as reference length a parameter linked to the interface, such as the groove span s . The final two dimensionless parameters are the ratios between the properties of the two fluids, density and viscosity. We can then write:

$$\pi_5 = Re_h = \frac{U_{cl}h}{\nu_H}, \quad \pi_6 = We = \frac{\rho_H U_{cl}^2 s}{\gamma}, \quad \pi_7 = m = \frac{\rho_A}{\rho_H}, \quad \pi_8 = \eta = \frac{\nu_A}{\nu_H}. \quad (2.28)$$

It could seem that the pressure gradient never appears in the definition of the dimensionless parameters, but it must be taken into account that the centre-line velocity is a function of the pressure gradient and of the channel thickness. Table 2.1 presents the summary of the dimensional analysis and the exploitation of Buckingham's theorem. With the definition of these dimensionless parameters, the results obtained at different scales can be compared.

In the problem with just one fluid, that is water, we do not have to consider the viscosity and density of the second fluid, the surface tension and the contact angle, therefore the relevant physical parameters reduce to $n = 7$ and consequently the dimensionless parameters reduce to $p = 4$. They are AR , λ , and d from (2.27) and Re_h from (2.28).

Chapter 3

Numerical formulation

In this chapter, we describe the numerical methods used in the present work. To solve the Young-Laplace equation, a specific software implemented with the *Mathematica* interface has been developed. This software combines a soothing method to integrate the ODE equation and a quasi-Newton iterative method to find the correct pressure-difference value corresponding to the sought contact angle. The equations for the base flow and the eigenvalue problem have been solved with the Finite Element Method (FEM), which is described in detail. By applying the Galerkin method on the weak formulation of system 2.11, the structure of the matrices that constitute the algebraic system representing the eigenvalue problem is obtained. This procedure has been implemented in the Unified Form Language (*UFL*). A description of the structure of the developed software is also provided, with particular attention on the *FEniCS* package [39] and the other libraries used.

3.1 Solution of the Young-Laplace equation

As mentioned in Section 2.3, this equation cannot be resolved in closed form due to the non-linearity. To find the solution $y(x)$, a numerical integration of the equation is needed. Moreover, there is a further complication: the heavier fluid, water, is above the lighter fluid, air. For this configuration, unlike the opposite situation with water below air, not all the pressure-difference values are possible. If the pressure difference is too high the water occupies the groove moving away the trapped air and the equilibrium cannot exist. In particular, the solution for a specific contact angle is sought, therefore the numerical integration must be connected with a quasi-Newton iterative method to solve the nonlinear relation $\sigma = \sigma(\alpha)$, where $\sigma = \frac{\Delta P}{\gamma}$, and obtain the correct pressure-difference value to be put into equation (2.25).

An effective way to solve this equation is to split the domain of integration. For symmetry reasons we can focus on just half of the groove span and use a shooting method to solve the boundary-value problem reducing it to an initial-value problem. Instead of imposing the values at the extremes of the groove, we impose

$$y(0) = 0, \quad y'(0) = 0. \tag{3.1}$$

Conditions (3.1) mean that the lowest point of the interface, which is the middle one, is taken as $y = 0$ and that in this point the tangent line to the curve is horizontal. Equation

(2.25) is then numerically solved in its dimensionless form using the groove half-span as reference length. The solution is then computed for $0 < x < 1$.

A software to solve the Young-Laplace equation for a specific angle of attack has been developed with the *Mathematica* package. For each iteration, the software integrates the ODE equation and corrects the pressure term with Newton's method. Since the initial guess on the pressure term could correspond to a contact angle very far from the target, the convergence is facilitated with a continuation. As input, the user provides the final target α_t and an intermediate target $\bar{\alpha}_t$. The software moves to a second intermediate target only upon reaching the first one and so on until convergence. The algorithm of the *Mathematica* software is reported in Algorithm 1. With a slight notation abuse, σ represents now the dimensionless pressure term and \hat{g} is the dimensionless hydrostatic term. They read

$$\sigma = \bar{s} \frac{\Delta P}{\gamma} \quad \hat{g} = \bar{s}^2 \frac{(\rho_A - \rho_H)g}{\gamma} \quad (3.2)$$

where \bar{s} is the groove half-span $\bar{s} = \frac{s}{2}$.

Algorithm 1 Newton's method for the Young-Laplace equation

- 1: Provide initial data $d\sigma$, \hat{g} , $\bar{\alpha}_t$, $d\bar{\alpha}_t$
 - 2: Provide initial guess σ and α_t
 - 3: **while** $|\bar{\alpha}_t - \alpha_t| > toll_{target}$ **do** ▷ Needed to obtain convergence
 - 4: $\bar{\alpha}_t \leftarrow \bar{\alpha}_t - d\bar{\alpha}_t$
 - 5: **while** $|\alpha - \alpha_t| > toll_{newton}$ **do**
 - 6: 1st numerical integration: computed solution $y(x)$
 - 7: $\bar{\sigma} = \sigma + d\sigma$
 - 8: 2nd numerical integration: computed solution $y_{\bar{\sigma}}(x)$
 - 9: $\alpha = 90 - 180 \arctan\left(\frac{dy}{dx}\right)$
 - 10: $\alpha_{\bar{\sigma}} = 90 - 180 \arctan\left(\frac{dy_{\bar{\sigma}}(x)}{dx}\right)$ ▷ $d\alpha = \alpha_{\bar{\sigma}} - \alpha$
 - 11: $\sigma \leftarrow \sigma - \frac{d\sigma}{d\alpha}(\alpha - \alpha_t)$ ▷ Newton's iteration for $\sigma = \sigma(\alpha)$
 - 12: **end while**
 - 13: **end while**
-

Figure 3.1 shows the solution obtained: the convergence to the sought contact angle $\alpha = 10^\circ$ has been obtained. The data is re-elaborated with *Matlab*: the solution is re-scaled and mirrored to cover the whole groove span. This procedure works for every groove span and it has been used to produce the curves used in the construction of the meshes for the numerical simulations. In figure 3.2, the bubble interface in a groove of unitary length is shown.

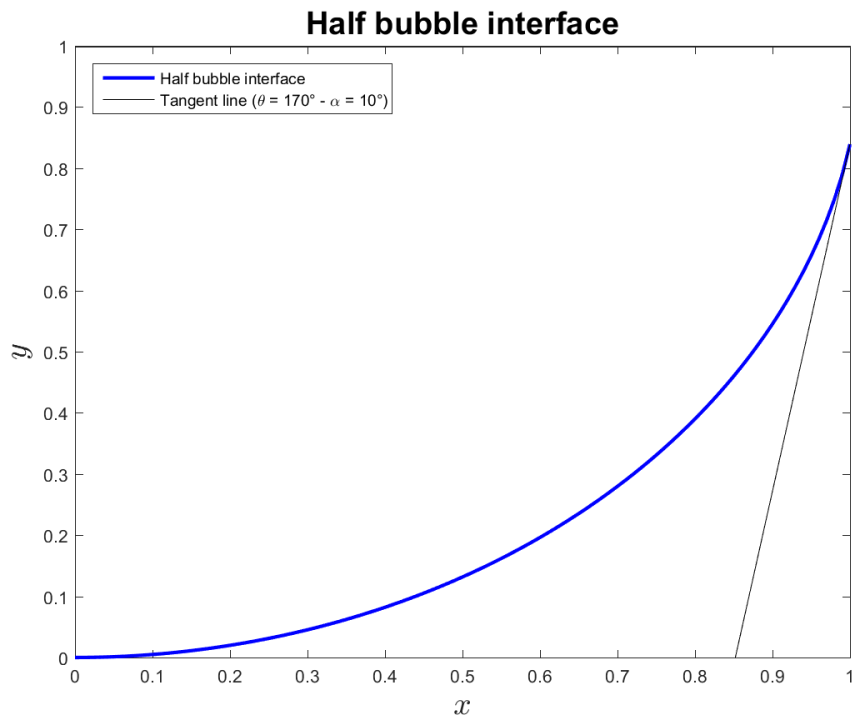


Figure 3.1: Solution for half of the groove obtained with the *Mathematica* software.

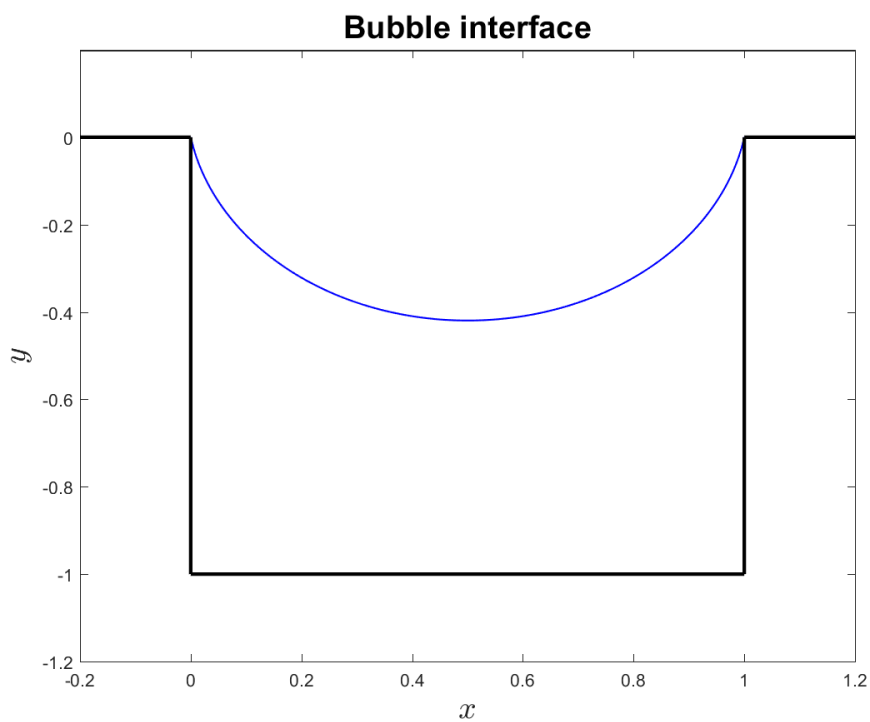


Figure 3.2: Bubble interface visualized inside a groove of unitary span.

3.2 Finite Element Method

The Finite Element Method (or FEM) is a numerical method for the solution of partial differential equations. The success of this method can be attributed to its generality and its flexibility. A prototypical application of the FEM is the Poisson equation, which is a second-order partial differential equation. In the present work the equation for the base flow (2.6), both single-phase and multi-phase, corresponds to a Poisson equation. Rewritten in a more compact form, it becomes:

$$-\nabla^2 w = f \quad \text{in } \Omega. \quad (3.3)$$

Equation (3.3) is completed with homogeneous boundary conditions $w = 0$ on the channel walls, corresponding to the no-slip condition, and periodicity condition on the lateral sides of the domain. The right-hand side f is a given function, $f = -Re \frac{\partial P}{\partial z}$ in the present case. The domain Ω is the cross section of the considered channel and we denote by $\partial\Omega_D$ the Dirichlet boundary, that is the boundaries where the no-slip condition is applied.

To apply the Finite Element Method, the weak formulation of equation (3.3) must first be obtained. In the weak formulation, the PDE is no longer required to hold pointwise but its projection on the test functions is imposed instead. Indeed, the weak formulation of a PDE such as (3.3) is obtained by multiplying the equation by a test function ϕ and integrating over the domain Ω

$$-\int_{\Omega} (\nabla^2 w) \phi \, dx = \int_{\Omega} f \phi \, dx. \quad (3.4)$$

This operation corresponds to an inner product. The term with the second-order derivative can be integrated by parts, thus transferring one derivative on the test function and decreasing the regularity required for the solution

$$-\int_{\Omega} (\nabla^2 w) \phi \, dx = \int_{\Omega} \nabla w \nabla \phi \, dx - \int_{\partial\Omega} \frac{\partial w}{\partial n} \phi \, ds. \quad (3.5)$$

Since we chose a test function which vanishes on the boundary, that is $\phi = 0$ on $\partial\Omega$, or by virtue of the periodicity conditions, the last term simplifies, therefore the weak formulation of equation (3.3) becomes:

Find $w \in H_D^1(\Omega)$ such that:

$$\int_{\Omega} \nabla w \nabla \phi \, dx = \int_{\Omega} f \phi \, dx \quad \forall \phi \in H_D^1(\Omega). \quad (3.6)$$

where $f \in L^2(\Omega)$ and $H_D^1(\Omega) = \{\phi \in H^1(\Omega) : \phi = 0 \text{ on } \partial\Omega_D\}$.

Now the problem (3.6) can be discretized, thus looking for an approximation of the solution in a finite-dimensional subspace of the functional space chosen for the test ϕ and trial w functions. The approximate solution is $w_h \in H_h^1(\Omega)$, where $H_h^1(\Omega) \subseteq H_D^1(\Omega)$ is a finite-dimensional functional space. The domain Ω is partitioned into cells, which are usually triangles in a two-dimensional problem. With each triangle \mathcal{K}_i , we associate a polynomial space \mathbb{P}^K and a number of degrees of freedom \mathcal{L} . The triplet $(\mathcal{K}_i, \mathbb{P}^K, \mathcal{L})$ defines a finite element. To compute the solution to the Poisson problem for the base flow, second order Lagrange polynomials \mathbb{P}^2 have been used.

Choosing the basis for the finite-dimensional functional spaces as $\{\phi_j\}_{j=1}^N$, where N is the dimension of the space, it follows that

$$w_h = \sum_{j=1}^N w_j \phi_j. \quad (3.7)$$

Substituting the approximation (3.7) into (3.6), and taking the test function $\phi = \phi_i$ for $i = 1, 2, \dots, N$, we obtain the final finite-dimensional form of the problem

$$\sum_{j=1}^N w_j \int_{\Omega} \nabla \phi_j \nabla \phi_i \, dx = \int_{\Omega} f \phi_i \, dx. \quad (3.8)$$

The finite element solution w_h can be now computed solving the linear system $A\mathbf{w} = \mathbf{b}$, where

$$A_{ij} = \int_{\Omega} \nabla \phi_j \nabla \phi_i \, dx, \quad b_i = \int_{\Omega} f \phi_i \, dx. \quad (3.9)$$

The procedure for the computation of the base flow with two fluids is exactly the same, with the exception that now the domain Ω is divided into two subdomains, Ω_c for the channel and Ω_b for the air bubble. Each subdomain has his own Poisson problem, but we can consider the same unknown, the velocity of the fluid, in a single domain. The right hand side will be discontinuous since the two Reynolds numbers are different and thus the given function changes. Without any particular complication, equation (3.6) becomes

$$\int_{\Omega_c} \nabla w \nabla \phi \, dx + \int_{\Omega_b} \nabla w \nabla \phi \, dx = \int_{\Omega_c} f_w \phi \, dx + \int_{\Omega_b} f_a \phi \, dx \quad \forall \phi \in H_D^1(\Omega). \quad (3.10)$$

where $f_w = -Re_w \frac{\partial P}{\partial z}$ and $f_a = -Re_a \frac{\partial P}{\partial z}$. Introducing the discrete spaces, the linear system to be solved is obtained. The solution corresponds to the velocity of water in Ω_c and the velocity of air in Ω_b . The continuity of the tangential velocities at the interface is automatically considered during the computation process.

Problem (3.10) can alternatively be considered a unique Poisson equation, defined on the whole domain Ω , with a discontinuous known function f . This is the approach used during the development of the code. A totally equivalent formulation of (3.10) is then

$$\int_{\Omega} \nabla w \nabla \phi \, dx = \int_{\Omega} f \phi \, dx \quad \forall \phi \in H_D^1(\Omega). \quad (3.11)$$

with f defined as follows:

$$\begin{cases} f = -Re_w \frac{\partial P}{\partial z} & \text{in } \Omega_c, \\ f = -Re_a \frac{\partial P}{\partial z} & \text{in } \Omega_b. \end{cases} \quad (3.12)$$

3.3 Eigenvalue problem for the water flow

The study of the linear stability of the flow to a wavelike perturbation requires solving system (2.11). This is achieved by applying the Galerkin method and exploiting the finite element method to obtain the eigenvalues $\omega_i = \omega_i(\kappa)$ and the corresponding eigenfunctions. The procedure is similar to the previous one presented for the Poisson problem, with the complication that now the trial function is a vector and not a scalar function. To obtain the weak formulation of system (2.11), a vector test function must be chosen. Using $\Phi = \{\phi^x, \phi^y, \phi^z, \psi\}$ as test function, the weak formulation reads:

$$\begin{aligned}
 & \text{Find } \hat{\mathbf{u}} \in H^1(\Omega) \text{ and } \hat{p} \in L^2(\Omega) \text{ such that:} \\
 & \left\{ \begin{aligned}
 & \int_{\Omega} \phi^x \omega \hat{u} + \int_{\Omega} \phi^x i\kappa W \hat{u} + \frac{1}{Re} \int_{\Omega} \nabla_{\mathbf{xy}} \phi^x \cdot \nabla_{\mathbf{xy}} \hat{u} + \frac{1}{Re} \int_{\Omega} \phi^x \kappa^2 \hat{u} - \int_{\Omega} \hat{p} \frac{\partial \phi^x}{\partial x} = 0, \\
 & \int_{\Omega} \phi^y \omega \hat{v} + \int_{\Omega} \phi^y i\kappa W \hat{v} + \frac{1}{Re} \int_{\Omega} \nabla_{\mathbf{xy}} \phi^y \cdot \nabla_{\mathbf{xy}} \hat{v} + \frac{1}{Re} \int_{\Omega} \phi^y \kappa^2 \hat{v} - \int_{\Omega} \hat{p} \frac{\partial \phi^y}{\partial y} = 0, \\
 & \int_{\Omega} \phi^z \omega \hat{w} + \int_{\Omega} \phi^z i\kappa W \hat{w} + \int_{\Omega} \frac{\partial W}{\partial x} \phi^z \hat{u} + \int_{\Omega} \frac{\partial W}{\partial y} \phi^z \hat{v} + \frac{1}{Re} \int_{\Omega} \nabla_{\mathbf{xy}} \phi^z \cdot \nabla_{\mathbf{xy}} \hat{w} \\
 & \quad + \frac{1}{Re} \int_{\Omega} \phi^z \kappa^2 \hat{w} + \int_{\Omega} \phi^z i\kappa \hat{p} = 0, \\
 & - \int_{\Omega} \psi \frac{\partial \hat{u}}{\partial x} - \int_{\Omega} \psi \frac{\partial \hat{v}}{\partial y} - \int_{\Omega} \psi i\kappa \hat{w} = 0.
 \end{aligned} \right. \quad (3.13)
 \end{aligned}$$

The pressure term has been integrated by parts to transfer the derivative on the test function. This expedient is not strictly necessary but, along with the change of the sign in the last equation, it helps obtain a final stiffness matrix with symmetric real part, but for the convection terms. To lighten the notation, all the differentials $d\Omega$ have been omitted and $\nabla_{\mathbf{xy}}$ indicates the two-dimensional gradient operator (with respect to x and y).

Similarly to what done for the Poisson problem, we introduce now the finite-dimensional approximation of the solution $\{\hat{u}_h, \hat{v}_h, \hat{w}_h, \hat{p}_h\} \in H_h^1(\Omega)$, namely

$$\hat{u}_h = \sum_{j=1}^N \hat{u}_j \phi_j^x, \quad \hat{v}_h = \sum_{j=1}^N \hat{v}_j \phi_j^y, \quad \hat{w}_h = \sum_{j=1}^N \hat{w}_j \phi_j^z, \quad \hat{p}_h = \sum_{j=1}^N \hat{p}_j \psi_j. \quad (3.14)$$

Substituting (3.14) into (3.13), we obtain the linear system corresponding to the temporal eigenvalue problem, which is of the form:

$$A(\kappa) \Theta = \omega(\kappa) M \Theta, \quad (3.15)$$

where Θ is the eigenvector, $\Theta = \{\hat{u}_1, \dots, \hat{u}_N, \hat{v}_1, \dots, \hat{v}_N, \hat{w}_1, \dots, \hat{w}_N, \hat{p}_1, \dots, \hat{p}_N\}$, M is the mass matrix and A is the Jacobian matrix. These two matrices have the following structure:

$$M = \begin{bmatrix} M^x & 0 & 0 & 0 \\ 0 & M^y & 0 & 0 \\ 0 & 0 & M^z & 0 \\ 0 & 0 & 0 & 0 \end{bmatrix}, \quad A = - \begin{bmatrix} A^x & 0 & 0 & P^x \\ 0 & A^y & 0 & P^y \\ C^u & C^v & A^z & -P^z \\ P^{xT} & P^{yT} & P^{zT} & 0 \end{bmatrix}. \quad (3.16)$$

The mass matrix is Hermitian but the Jacobian matrix is not, due to the convection terms and the imaginary part. The elements of the matrix blocks read as follows:

$$M_{ij}^x = \int_{\Omega} \phi_i^x \phi_j^x, \quad M_{ij}^y = \int_{\Omega} \phi_i^y \phi_j^y, \quad M_{ij}^z = \int_{\Omega} \phi_i^z \phi_j^z, \quad (3.17)$$

$$\begin{aligned} A_{ij}^x &= \int_{\Omega} \phi_i^x \phi_j^x i\kappa W + \frac{1}{Re} \int_{\Omega} \phi_i^x \phi_j^x \kappa^2 + \frac{1}{Re} \int_{\Omega} \nabla_{\mathbf{xy}} \phi_i^x \cdot \nabla_{\mathbf{xy}} \phi_j^x \\ A_{ij}^y &= \int_{\Omega} \phi_i^y \phi_j^y i\kappa W + \frac{1}{Re} \int_{\Omega} \phi_i^y \phi_j^y \kappa^2 + \frac{1}{Re} \int_{\Omega} \nabla_{\mathbf{xy}} \phi_i^y \cdot \nabla_{\mathbf{xy}} \phi_j^y \\ A_{ij}^z &= \int_{\Omega} \phi_i^z \phi_j^z i\kappa W + \frac{1}{Re} \int_{\Omega} \phi_i^z \phi_j^z \kappa^2 + \frac{1}{Re} \int_{\Omega} \nabla_{\mathbf{xy}} \phi_i^z \cdot \nabla_{\mathbf{xy}} \phi_j^z \end{aligned} \quad (3.18)$$

$$P_{ij}^x = - \int_{\Omega} \psi_j \frac{\partial \phi_i^x}{\partial x}, \quad P_{ij}^y = - \int_{\Omega} \psi_j \frac{\partial \phi_i^y}{\partial y}, \quad P_{ij}^z = - \int_{\Omega} i\kappa \psi_j \phi_i^z, \quad (3.19)$$

$$C_{ij}^u = \int_{\Omega} \frac{\partial W}{\partial x} \phi_i^z \phi_j^x, \quad C_{ij}^v = \int_{\Omega} \frac{\partial W}{\partial y} \phi_i^z \phi_j^y. \quad (3.20)$$

3.4 Software architecture

The final software developed to solve the complex eigenvalue problem has a quite complicate structure, result of the mixed programming with *C++* and *Fortran90*. The numerical solution of the base flow and the assembly of the matrices has been performed with the *FEniCS* library. Instead, to solve the eigenvalue problem, an already available eigenvalue solver implemented in *Fortran90* has been used. The solver has been integrated in the *Fortran90* module which builds the complex jacobian matrix and that is interfaced with the *C++* code. Hereafter, a brief description of all the components of the software is provided.

3.4.1 FEniCS library

The *FEniCS* library is a *C++* and *Python* package for the automated solution of partial differential equation using the finite element method [39]. By virtue of its components it allows one to write the variational form of a PDE equation in high-level mathematical description and to discretize it with different kinds of finite elements.

UFL and FFC

The Unified Form Language (*UFL*) is a domain specific language for the declaration of finite element discretizations of variational form and functionals. It allows one to choose finite element spaces and define the expression of the weak form of PDE equations in a notation close to mathematical notation. It is also possible to define integrals over subdomains and over external and internal boundaries (release 1.6.0). The FEniCS Form Compiler (*FFC*) generates efficient low-level *C++* code from the high-level mathematical

description in *UFL* and produces a *C++* header containing all the information for the finite element discretization of the form. The header must be included into the main program. A detailed description of the UFL code concerning the present work is given in Appendix B

Dolfin

Dolfin is the core library of the package in which a large part of the functionality of *FEniCS* is implemented. The *Dolfin C++* interface is designed as a standard object-oriented *C++* library. It provides classes which model important concepts for finite element computing and the routines for the sparse assembly of the forms defined in the FFC headers. It also provides linear and nonlinear algebra tools and wrappers to external libraries such as *PETSc*, which has been used in the present work. *Dolfin* set of input-output procedures allows one to read complex meshes in XML format and to save functions, vector and matrices to file.

3.4.2 Other libraries

In addition to the *FEniCS* package, the developed software required the use of native functionalities of the wrapped *PETSc* library and the use of the subroutines provided by the *ARPACK* library[27].

PETSc

The Programming Extensible Toolkit for Scientific Computation (*PETSc*) consist in a variety of libraries, each one manipulating a specific class of object and related operations. In the present work it has been used to store the matrices of the eigenvalue problem in CRS format and to store the data saved by the *Fortran90* code in order to define the *Dolfin* function containing the eigenfunction associated with the dominant eigenvalue.

ARPACK

The ARnoldi PACKage (*ARPACK*) is a collection of *Fortran77* subroutines designed to solve large eigenvalue problems. It is capable of solving large scale Hermitian, non-Hermitian, standard or generalized eigenvalue problems. The software is designed to compute k eigenvalues with user specified features, such as largest real part or largest magnitude. In the present work the given *Fortran90* module applies the requested shift to the matrices of the generalized eigenvalue problem and then uses the *ARPACK* subroutines to compute the number of eigenvalues, and the corresponding eigenfunctions, requested by the user from a configuration file.

Chapter 4

Validation of the code

This chapter provides the description of the validation process of the code developed to study the stability of the multi-phase flow in a channel with a grooved wall. This specific geometry has received particular attention only recently, due to the growing interest in potential application of SH surfaces. For this reason, specific results are not available in literature, therefore there are no reference results for the computed flow to date. The validation process will follow a step by step procedure. First, the base flow for a simplified version of the problem is computed, that is a water flow in a plane channel. This situation corresponds to the well known Poiseuille flow, which can be analytically solved [36]. The obtained solution is compared with the exact solution. The second step is to compute the base flow for a water flow in a channel with the grooved wall. The same water flow is then recomputed introducing the bubble interface as a fake interface between two flows of the same fluid. This result is then compared with the previous one. Lastly, the multi-phase, air and water, base flow is computed for an approximate combination of physical parameters and compared to the single-phase flow.

The software developed to solve the eigenvalue problem has been validated solving the well-studied problem of the linear stability in a plane channel [21]. The results obtained with the developed software have been compared with the results provided by a reliable software that solves the Orr-Sommerfeld equation with Legendre polynomials. The Orr-Sommerfeld equation constitutes an eigenvalue problem for the wall-normal velocity component of a parallel flow, such as the Poiseuille flow in a plane channel. Successively, the influence of the width of the considered portion of channel in the xy plane has been investigated. Eventually the dependency of the growth rate and phase velocity of the dominant eigenvalue on the refinement of the mesh has been examined: the same eigenvalue problem has been solved on meshes with a different number of elements.

4.1 Poisson problem

This section is dedicated to the validation of the *FEniCS/C++* code for the solution of the Poisson problem corresponding to the base flow. The base flow solution, though fairly simple, is necessary to assemble the matrices of the eigenvalue problem.

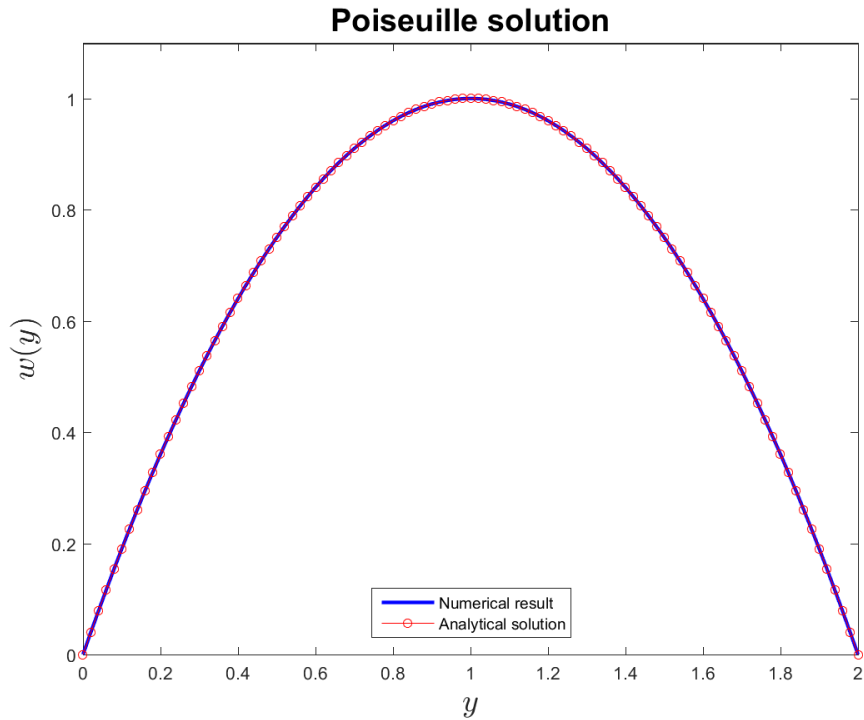


Figure 4.1: Comparison of the computed flow with the analytical solution of the Poiseuille flow.

4.1.1 Poiseuille flow

The lack of results available in literature for the problem we want to address compels us to find an indirect way to validate the code. First of all we will ascertain that the code works in a simplified situation which, despite not being the studied problem, can still give reliable indications about the correctness and accuracy of the code itself.

As a first test case, we computed the single-phase, steady flow between two plane surfaces subject to a constant pressure gradient. In fact for this flow an exact solution of the Navier-Stokes equations exists, the renowned plane Poiseuille flow, that can be assumed as a reference.

In the Poiseuille flow, the velocity field is parallel and invariant in the spanwise and streamwise directions. Using the same reference system described in section 2.1, with x as the spanwise direction and z as the streamwise direction, the Navier-Stokes equations for the Poiseuille flow reduce to:

$$\frac{d^2w}{dy^2} = Re \frac{dP}{dz}. \quad (4.1)$$

Denoting the channel height by H , the equation is completed by the boundary conditions

$$w(0) = 0, \quad w(H) = 0. \quad (4.2)$$

Observing equation (4.1), it is immediately evident that it is quite similar to the third equation of system (2.6). The only difference is the two-dimensional Laplacian operator instead of the second derivative, however if we test the code on a plane channel eliminating

the groove, the results must agree with the Poiseuille exact solution. Considering a constant pressure gradient $\frac{dP}{dz} = G_z$, the solution to equation (4.1) is:

$$w(y) = -\frac{G_z Re H^2}{2} \frac{y}{H} \left(1 - \frac{y}{H}\right), \quad (4.3)$$

where G_z is the dimensionless pressure gradient and Re the Reynolds number. Equation (4.4) represents a parabola arc which must be reproduced by the code.

The Reynolds number has been defined on the channel half-height $h = 1$ and with the centre-line velocity U_{cl} . The imposed dimensionless pressure gradient is $G_z = -\frac{2}{Re}$, needed to obtain a centre-line velocity $U_{cl} = 1$. Equation 4.4 then becomes:

$$w(y) = y(2 - y). \quad (4.4)$$

From figure 4.1 we deduce that the computed flow and the analytical solution almost perfectly match. The computed profile has been taken at the spanwise midline of the rectangular section. We can assume that the code is fully capable of solving the single-phase base flow on a simple geometry.

4.1.2 Poisson problem with two subdomains

As second step in the validation process, a channel with a grooved wall is considered. In this case, the flow is no longer invariant in the spanwise direction. The main objective of this section is to ascertain the capability of the code to successfully compute the base flow, which corresponds to a Poisson equation, on two different subdomains connected by an interface.

First, the water flow in a single domain will be computed to provide a reference for comparison. In this case, in fact, there is no analytical solution. Nevertheless, since the periodic boundary condition holds, we expect the computed flow to be at least symmetrical with respect to the midspan line. The no-slip Dirichlet boundary condition is applied to the top, bottom and groove walls. The set of parameters used in this calculation is the same described in Section 4.1.1.

Figure 4.2 shows the computed solution. As predicted, due to the presence of the groove, the flow is not spanwise invariant, even though, away from the groove, the solution tends to become identical to the Poiseuille flow.

The second step is the computation of the same flow, but this time with two subdomains introducing the interface between the two regions. In this case, the interface is an artefact, since the same fluid is present on each side of the interface. The code solves two different Poisson equations, each one applied only in its own subdomain.

Each Poisson equation has its own boundary conditions, homogeneous Dirichlet and periodicity for the channel domain Ω_c and homogeneous Dirichlet only for the bubble domain Ω_b . Considering the problem formulated as in (3.11) - (3.12), the imposition of interface condition is not required since the continuity of the tangential velocity is automatically obtained by the resolution process.

Figure 4.3 demonstrates that the two solutions are exactly the same, thus validating the code for multiple domains.

To further verify the quality of the code, the comparison between the velocity profiles at the midspan line is presented in figure 4.4. It is similar to the Poiseuille profile in the upper part of the channel but it now has two inflection points inside the groove.

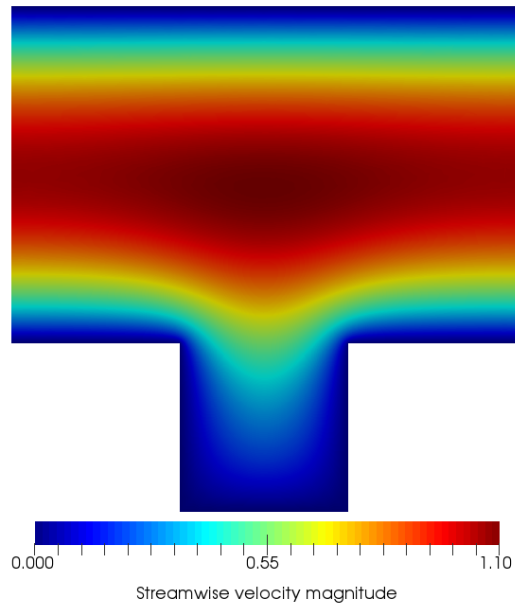


Figure 4.2: Solution to the Poisson equation for the water flow with only one subdomain.

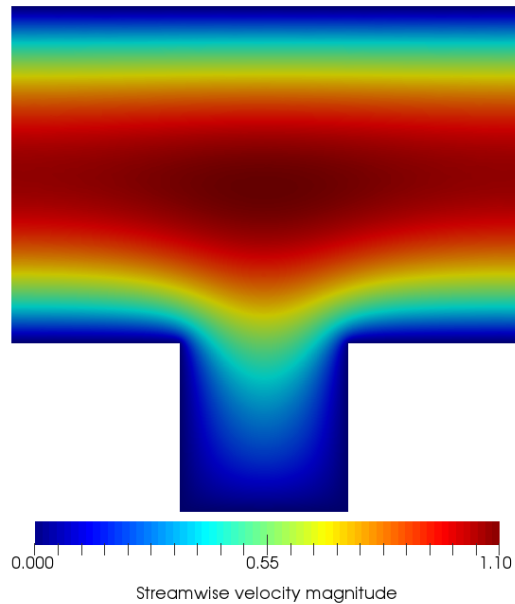


Figure 4.3: Solution to the Poisson equation for the water flow computed in two subdomains.

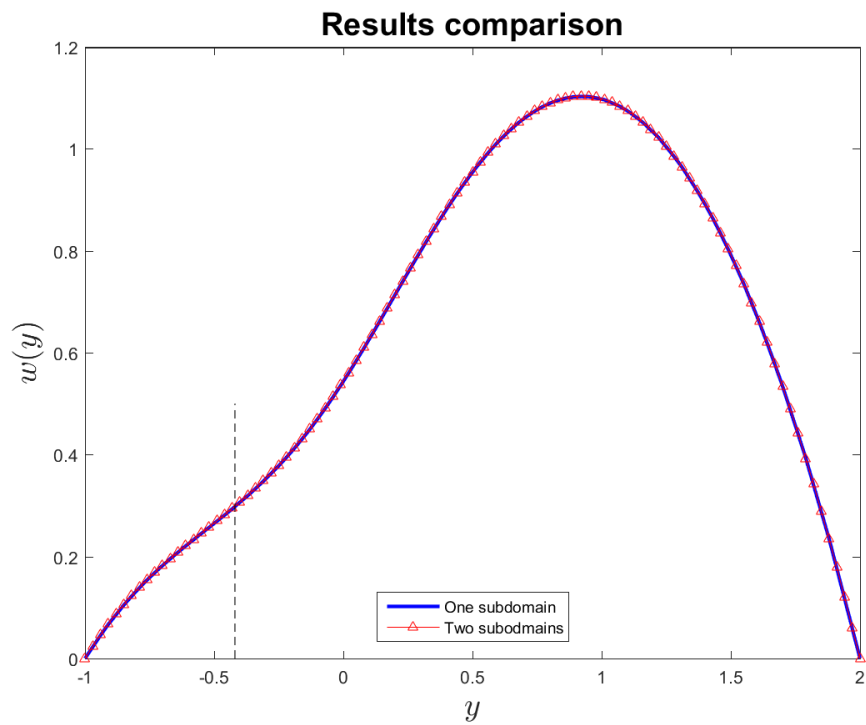


Figure 4.4: Comparison between the velocity profiles of the water flow in the grooved channel obtained with a single or two subdomains. The black dashed line shows the fake interface location.

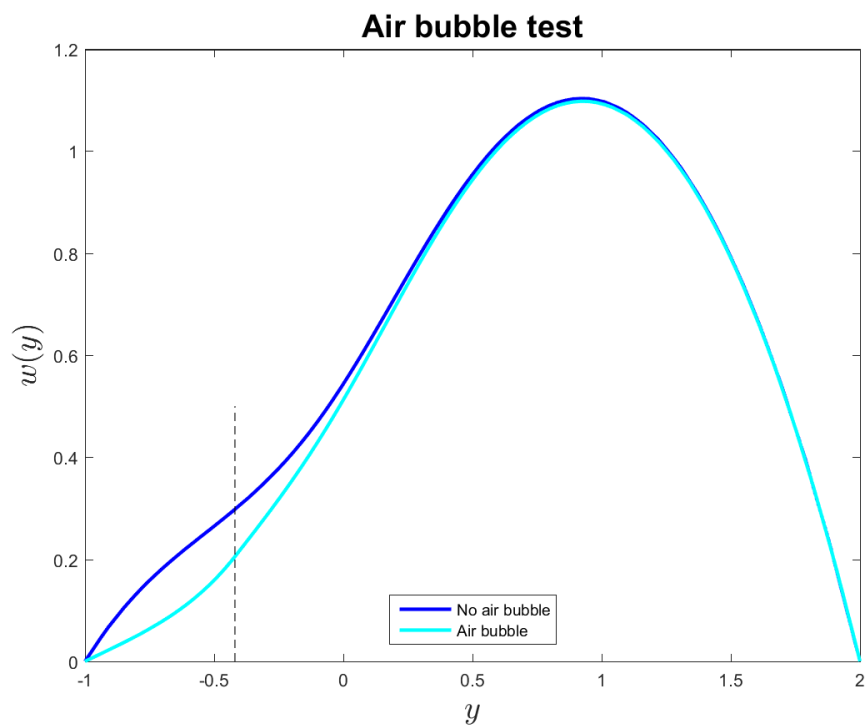


Figure 4.5: Comparison between the velocity profiles of the water flow without air bubble and with air bubble. The black dashed line shows the interface location.

4.1.3 Test with air bubble

Since the code has already been validated, the simulation with the air bubble is just a qualitative test. The channel section is divided into two subdomains by the interface between the two fluids. Water occupies the channel domain Ω_c and air occupies the bubble domain Ω_b . The procedure is exactly the same adopted in Section 4.1.2, however the viscosities, and therefore the Reynolds numbers, in the two subdomains are now different. We expect the fluid velocity inside the bubble to be lower with respect to the previous case, due to the higher kinematic viscosity of air with respect to water. Figure 4.5 confirms the theoretical expectations.

4.2 Eigenvalue problem

This section describes the validation of the combined *FEniCS/C++* and *Fortran90* code dedicated to the formulation and solution of the eigenvalue problem of a mono-phase flow. The eigenvalue solver is the most important part of the developed software, therefore it needs accurate validation. First, we compare the results with that available in literature. Second, we analyse how the refinement and the geometry of the mesh influences the results.

4.2.1 Eigensolutions

The complete development of the eigenvalue solver, from the weak formulation of the equations to saving the results, has required the testing of many pieces of code. Particularly laborious has been the interface between the *C++* code and the *Fortran90* code. The main reason that lead to the choice of a mixed programming approach is the complex nature of the jacobian matrix. *FEniCS* is not capable of dealing with complex numbers, therefore the real and imaginary part of the jacobian matrix have been assembled separately and merged with the *Fortran90* code. No-slip boundary conditions have been imposed in all matrices by annihilating the rows and columns corresponding to the nodes on the boundary and setting the diagonal element to one.

Like in the Poisson problem, the validation of the code has been performed on a well-known problem, that is the linear stability of a flow in a plane channel, for which plenty of data is available in the literature. We know that this is a parallel flow that becomes unstable to two-dimensional Tollmien-Schlichting waves with wavenumber $\kappa = 1.02$ at $Re = 5772$, if the Reynolds number is based on the the channel half-height and the centre-line velocity [31, 32].

To validate the developed software, the obtained results for the plane channel problem have been compared with the results provided by a reliable and well-tested *Fortran90* software that solves the Orr-Sommerfeld equation, described in Appendix A.

Figure 4.6 shows that the developed software computes correctly the eigenvalue spectrum of the linear stability problem for the Poiseuille flow in a plane channel. Even if not all eigenvalues match, the three branches $A(c_i \rightarrow 0)$, $P(c_i \rightarrow 1)$, $S(c_i \approx 2/3)$ are clearly visible. Moreover, the dominant eigenvalue $\omega = -3.4020 \cdot 10^{-7} - 0.2692i$ almost perfectly matches the reference result.

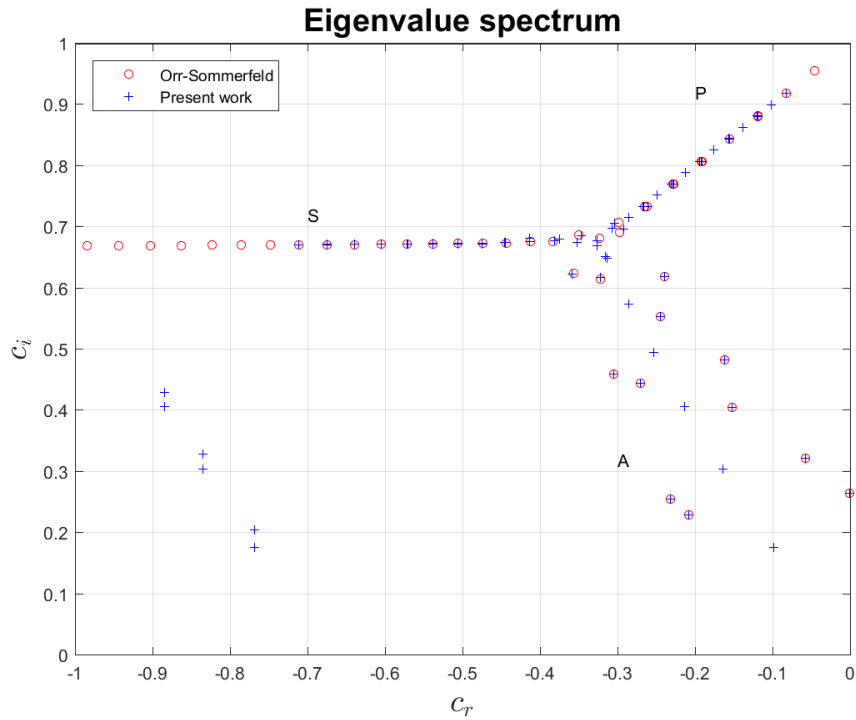


Figure 4.6: Comparison of the eigenvalues spectrum computed with the Orr-Sommerfeld software and the software developed for the present work.

The last step of the validation process of the eigenvalue solver is to check the shape of the eigenfunction corresponding to the dominant eigenvalue, which belongs to the A branch of the spectrum. The Orr-Sommerfeld software directly computes the profile of the vertical perturbation velocity \hat{v} . Instead, the developed software computes the complete eigenfunction Θ field on the whole two-dimensional domain representing the plane channel section. To compare the results, the profile of \hat{v} at the channel spanwise midline has been extracted. To make the results compatible, the real and imaginary part of the computed eigenfunction have been switched. Moreover, both profiles have been scaled with the respective integral evaluated with the trapezoidal rule.

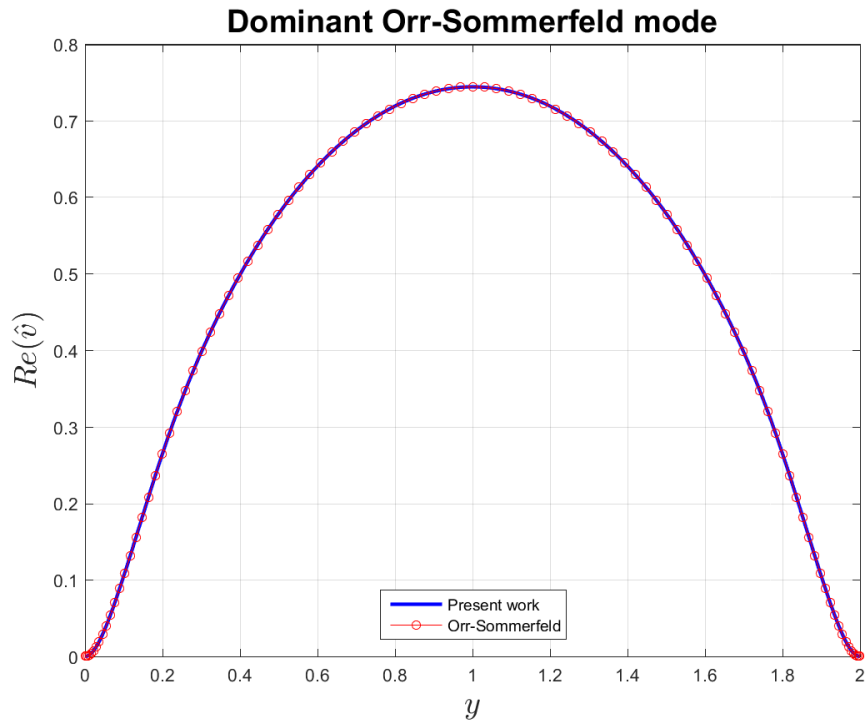


Figure 4.7: Comparison of the real part of the eigenfunction \hat{v} computed with the Orr-Sommerfeld software and the software developed for the present work.

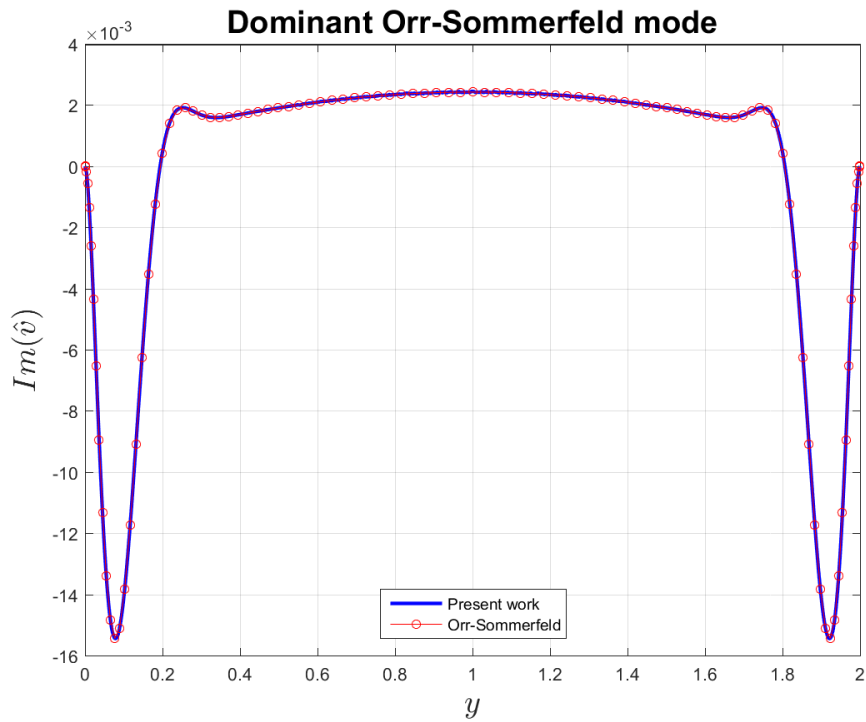


Figure 4.8: Comparison of the imaginary part of the eigenfunction \hat{v} computed with the Orr-Sommerfeld software and the software developed for the present work.

4.2.2 Sensitivity to channel width and mesh refinement

To evaluate if different sizes of the mesh may produce variations in the solution and to evaluate their magnitude, the eigenvalue spectrum has been calculated for different widths of the plane-channel section and three shifts, $\xi_P = 0.01 - i$, $\xi_S = -0.3 - 0.67i$ and $\xi_A = 0.01 - 0.264i$. The number of requested eigenvalues is $k = 100$ in all cases. This value has been chosen to obtain meaningful results while keeping the requested CPU time and memory affordable. From figure 4.9 we can deduce that the choice of shift strongly affects the portion of spectrum that is computed. In all cases, not all of the original eigenvalues of the Orr-Sommerfeld spectrum are computed because some of them are hidden by new eigenvalues closer to the shift value. This is due to the fact that the Orr-Sommerfeld equation is a one-dimensional problem while the developed software solves a 3D problem on a two-dimensional domain. With a very narrow section only the instability modes with null or very high wavenumbers are permitted. By increasing the section width, more and more modes with low wavenumber are detected. As a consequence new eigenvalues appear in the Orr-Sommerfeld spectrum. In particular, the new modes seem to enrich the A branch of the spectrum and to form secondary P branches parallel to the original one.

To evaluate the dependency of the solution on the mesh refinement, the same test case of the channel with rectangular grooves has been repeated for different meshes, listed in Table 4.1. The results for the dominant eigenvalue are presented in figure 4.11 and 4.12. The phase velocity, that is the imaginary part of the eigenvalue, shows a decreasing variation with increasing refinement of the mesh. The growth rate, that is the real part, stabilizes with absolute variations of 10^{-7} if more than 100000 elements are used. For these reasons, and with the aim of keeping an acceptable CPU time, all the meshes used hereafter have a number of elements in the range 100000 - 400000. It must be remarked that the elements are not uniformly distributed in the mesh but they are coarser in the centre of the channel and finer near the channel walls, especially close to the groove edges and the interface between air and water where high accuracy is required.

Mesh	n_{nodes}	$n_{elements}$	$u_{elements}$	$p_{elements}$	t_{CPU} [s]
M50	24362	48750	$P2$	$P1$	476.31
M100	56520	113066	$P2$	$P1$	1209.49
M200	95490	191006	$P2$	$P1$	2178.40
M250	137618	275262	$P2$	$P1$	3151.96

Table 4.1: Characteristics of the meshes used to test the convergence of the leading eigenvalue. CPU time refers only to the eigenvalue solver and it does not take into account the CPU time needed for the base-flow computation and matrix assembly.

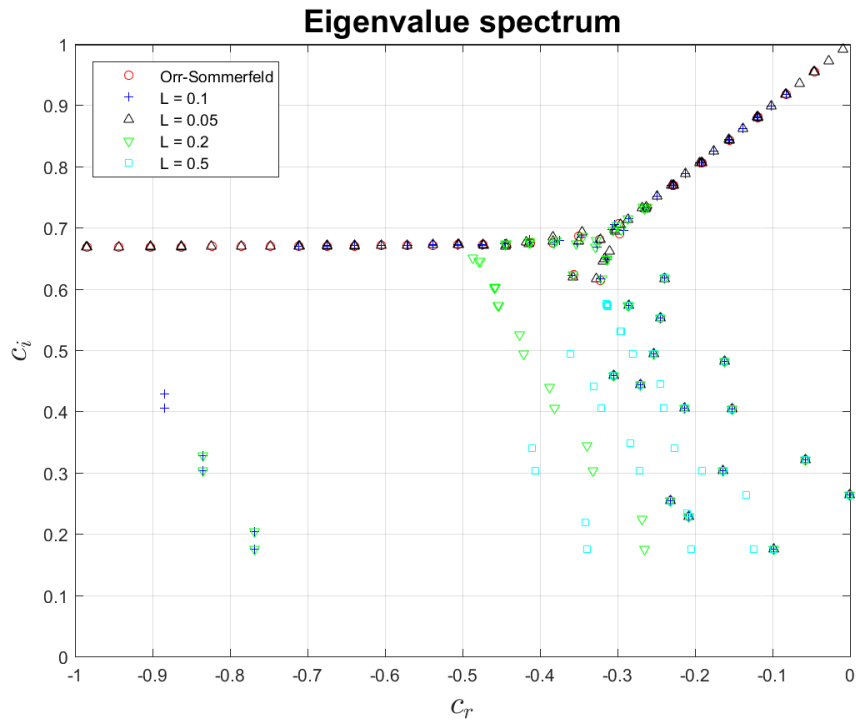


Figure 4.9: Eigenvalue spectra computed with different channel-section widths. Shift ξ_A and $k = 100$.

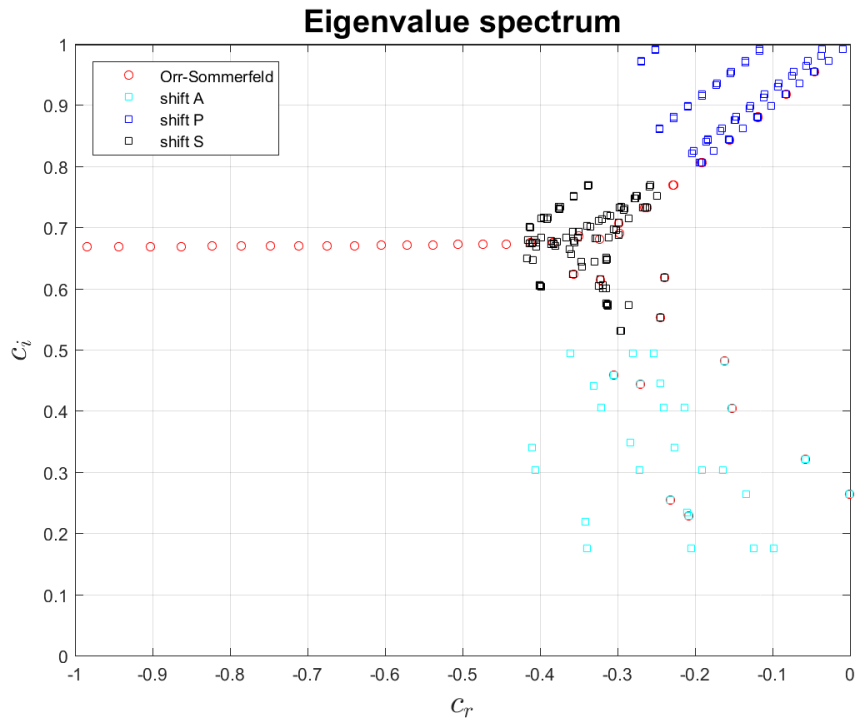


Figure 4.10: Eigenvalue spectra computed with different shifts. Channel with $L = 0.5$ and $k = 100$.

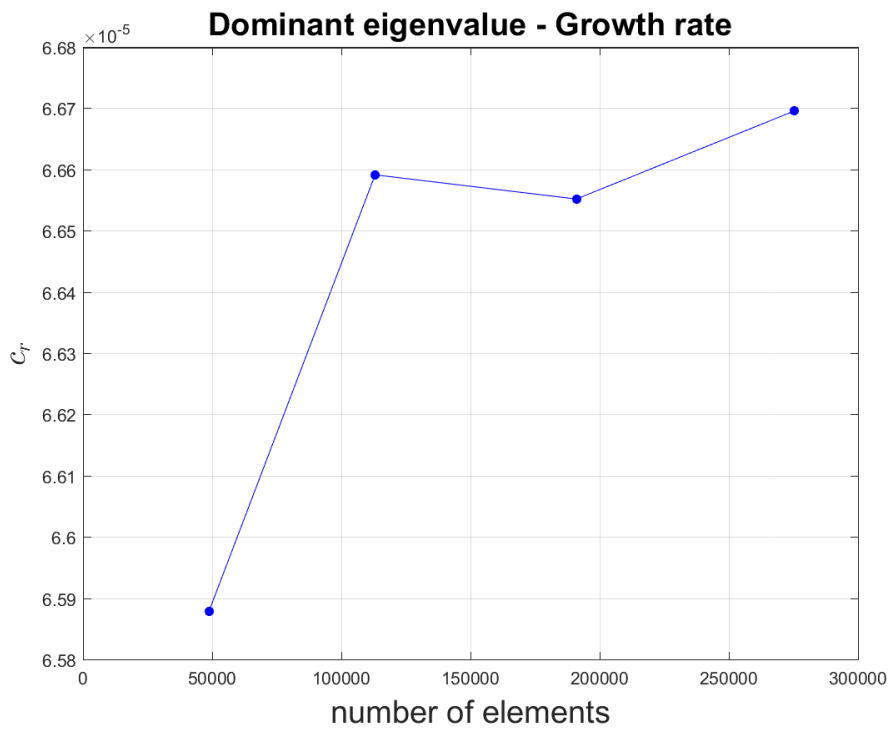


Figure 4.11: Value of the growth rate of the dominant eigenvalue computed with different meshes.

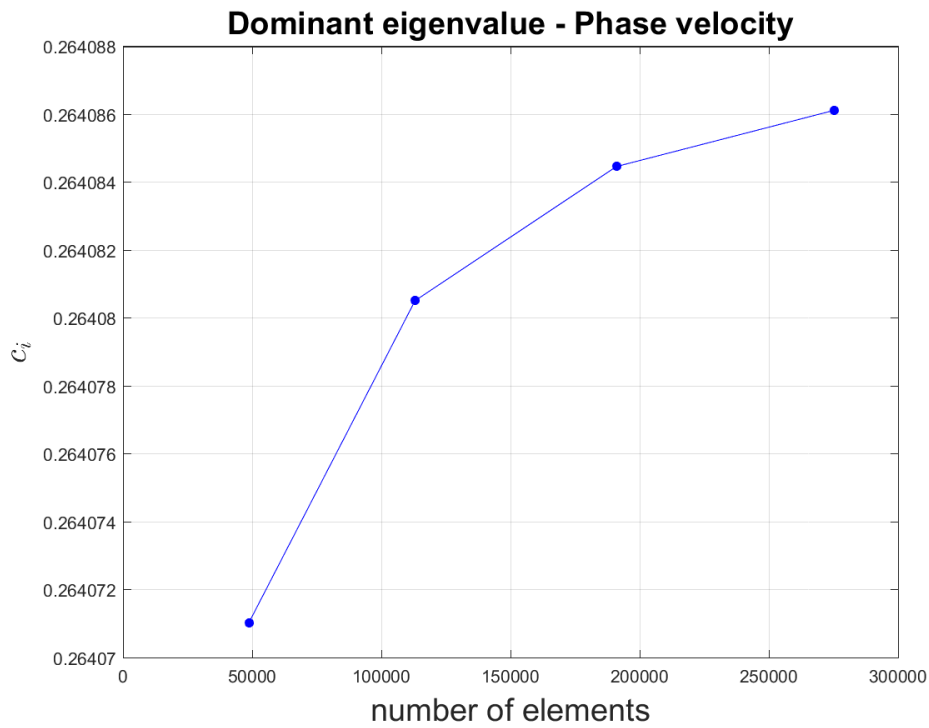


Figure 4.12: Value of the phase velocity of the dominant eigenvalue computed with different meshes.

Chapter 5

Results

This chapter presents all the results of the linear stability analysis. Firstly, we investigated how the amplitude of the grooves affects the flow stability by tracking the dominant eigenvalue for different low values of wall roughness, but imposed groove wavelength. Then, we located the critical Reynolds of the flow in a channel with grooves of different dimension and shape, namely rectangular and triangular grooves and wall roughness $d = 0.01$, $d = 0.02$, $d = 0.05$, $d = 0.1$. These values have been chosen by establishing an analogy with the Blasius boundary layer flow, which could represent realistic scenarios of possible applications of riblets and SH surfaces. In addition, the approximate neutral curves for $d = 0.02$ and $d = 0.05$ have been drawn from the essential sample points. The analysis of the real part of the normalized eigenfunction in the xy plane has also been carried out. Lastly, as a preparatory phase for the investigation of the complete problem, the velocity profiles of the multi-phase base flow have been obtained.

5.1 Eigenvalue tracking

An interesting analysis is the eigenvalue tracking for different values of wall roughness d . The main objective is to understand how the groove amplitude affects the stability of the flow. The eigenvalue spectrum has been computed for increasing roughness values and an imposed wavelength, $\lambda = 0.02$ for the rectangular grooves and $\lambda = 0.01$ for the triangular grooves. In this way the section increase of the overall channel due to the grooves is comparable for both geometries and so it is the increase of the flow rate. To examine the fluid behaviour for the same critical parameters of a plane channel, the Reynolds number is $Re = 5772$ and the disturbance streamwise wavenumber is $\kappa = 1.02$.

Figure 5.1 and 5.2 show the position of the dominant eigenvalue in the $(c_r - c_i)$ plane, for the rectangular and the triangular grooves, respectively. In both cases, the grooves have a similar unstabilizing effect on the channel flow. These results are compatible with those obtained by Moradi and Floryan [32] and Ehrenstein [12]. The wavelengths $\lambda = 0.02$ and $\lambda = 0.01$ correspond to groove wavenumbers $\beta = 314$ and $\beta = 628$ respectively, which are both abundantly above the transition wavenumber $\beta_{trans} = 4.22$. However, this value is purely a qualitative reference, since it is relative to sinusoidal grooves. Even though the flow is destabilized, the increase in growth rate c_r is very small, due to the fact that the considered roughness values are also very small, with the limit case of $c_r \approx 0$ for $d = 0.0002$, that is almost a plane channel.

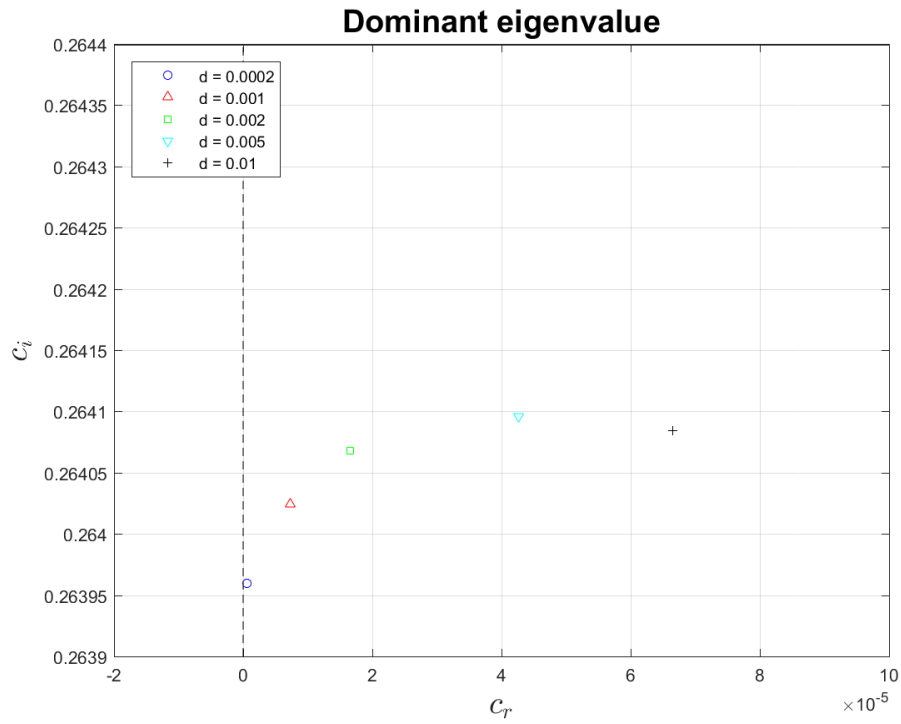


Figure 5.1: Dominant eigenvalue for rectangular grooves of different amplitude and $\lambda = 0.02$. $Re = 5772$ and $\kappa = 1.02$.

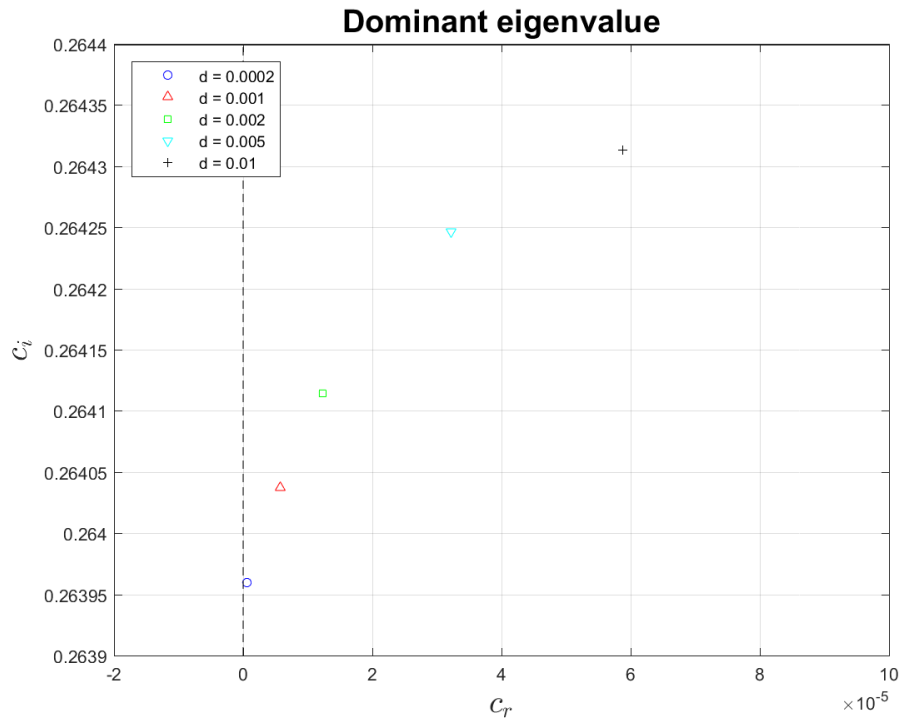


Figure 5.2: Dominant eigenvalue for triangular grooves of different amplitude and $\lambda = 0.01$. $Re = 5772$ and $\kappa = 1.02$.

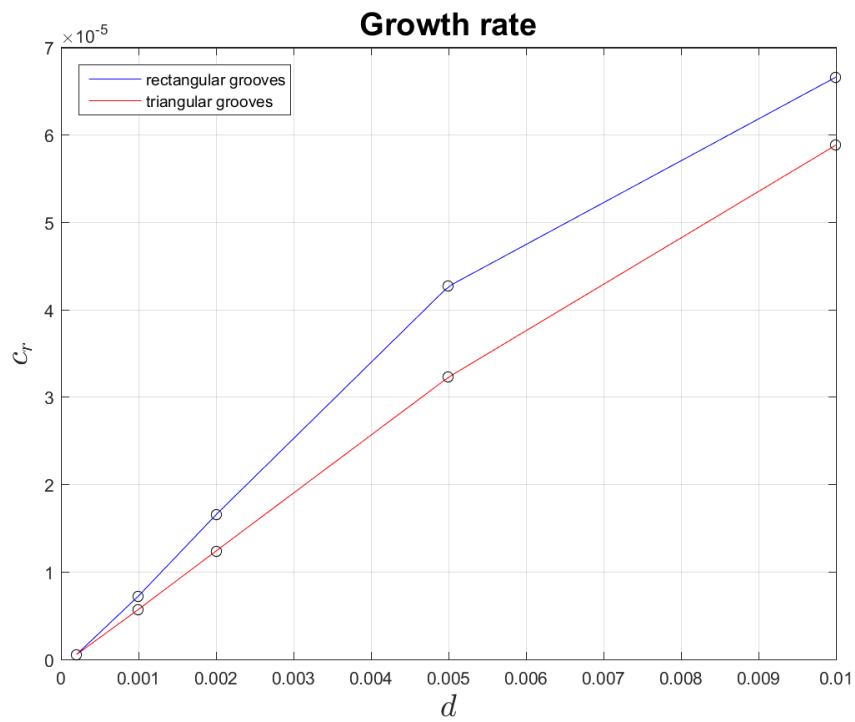


Figure 5.3: Growth rate of the dominant eigenvalue as a function of the wall roughness. $Re = 5772$ and $\kappa = 1.02$.

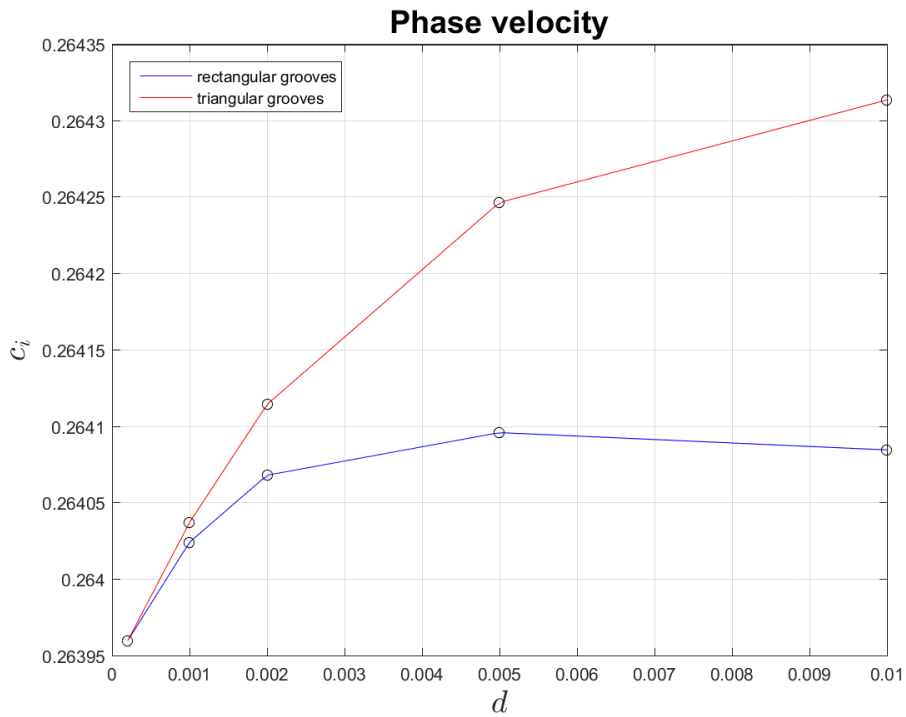


Figure 5.4: Phase speed of the dominant eigenvalue as a function of the wall roughness. $Re = 5772$ and $\kappa = 1.02$.

The roughness of the channel wall and the growth rate of the dominant eigenvalue are almost linearly proportional, as we can see in figure 5.3. The destabilization rate is slightly greater for the rectangular grooves. On the other hand, the phase velocity increases more rapidly for the triangular grooves, and not in a linear way (figure 5.4). From the available data it seems that it tends to a constant value as the roughness increases. This result must be interpreted as a trend, since the slightly different number of elements in the mesh can also play a role, as we have already seen in figure 4.12

We can conclude that the results of Moradi and Floryan obtained for sinusoidal grooves can be extended to rectangular and triangular grooves.

5.2 Flow in a channel with SH geometry

This section is dedicated to investigate the stability of the flow in a channel with longitudinal grooves similar to those which characterize SH surfaces, neglecting the nano-structured roughness and the air bubble. The problem is strongly simplified with respect to the multi-phase problem. Nonetheless, the results presented in this section constitute a solid knowledge base necessary to interpret the results for the complete problem with the air bubble.

5.2.1 Boundary layer analogy

The control parameters must be chosen wisely, for the results to be meaningful for possible applications. To this end, we could establish an analogy between the channel flow and the boundary layer flow around a flat plate aligned with the stream. Even though the behaviour of these flows is substantially different and the boundary layer problem better represents possible applications of regular riblets and SH surfaces, the channel flow is by far simpler and it is therefore adopted in this work. The conventional reference length for the boundary layer is the displacement thickness δ^* and the free-stream speed U_∞ is the reference velocity. Unlike the channel flow, which is driven by the pressure gradient, the Blasius boundary layer flow is driven by the free-stream speed of the external flow. Moreover, the disturbances are not spatially confined by the channel walls and they can propagate more freely. For these reasons, the critical Reynolds number $Re_{\delta^*} = 519$ and disturbance wavenumber $\kappa_{\delta^*} = 0.3$ [40], based on U_∞ and δ^* , are quite different from the ones for channel flow, $Re_h^{CH} = 5772$ and $\kappa_h^{CH} = 1.02$.

Despite the abovementioned caveats, the analogy is useful to obtain reasonable orders of magnitude for the control parameters, in particular the roughness d and therefore the channel half-height h . If we consider a solid body moving through water, for example a ship hull, the boundary layer becomes thicker as the water flows from bow to stern. The grooves have constant amplitude and span, therefore the thicker the boundary layer the smaller the roughness with respect to it: once the size of the grooves is fixed, different values of roughness represent different streamwise stations on the solid body. If we impose the free-stream speed, we can evaluate the displacement thickness of the boundary layer corresponding to the critical Reynolds number and therefore the associated roughness value. However, this value must be then adjusted to evaluate its equivalent for the plane channel.

	average speed		d^{BL}	d
	kn	m/s	-	-
cruiser ship	20	10.19	0.28	0.09
oil tanker	13	6.69	0.18	0.06
container ship	25	12.86	0.25	0.08
icebreaker	18	9.26	0.35	0.11
patrol boat	23	11.83	0.31	0.10
air carrier	30	15.43	0.42	0.13
submarine	35	18.01	0.50	0.16
white shark	-	10.00	0.28	0.09

Table 5.1: Average speed for different ship types and the white shark with the corresponding channel roughness.

Firstly we estimated the ratio between the two reference lengths δ^* and h by comparing a Poiseuille parabolic profile and a Blasius profile with the same reference speed $U_{cl} = U_\infty$ and the same wall stress $\tau_w = \mu_H \frac{\partial w}{\partial y} \Big|_{y=0}$. Then, the critical Reynolds number and disturbance wavenumber of the Blasius flow have been rescaled with the ratio $\frac{h}{\delta^*} \approx 3.5$, obtaining

$$Re_h^{BL} = 1818 \quad \kappa_h^{BL} = 1.06. \quad (5.1)$$

We observe that the critical disturbance wavenumbers of the channel flow and the boundary layer flow are approximately the same $\kappa_h^{CH} \approx \kappa_h^{BL}$, but the critical Reynolds numbers are still quite different. For this reason, to compare two flows in the same quasi-unstable conditions and with the same reference speed, the value of the reference length h must be different. Considering the average speed of different types of ships, we computed the half-height h^{BL} and the roughness d^{BL} corresponding to Re_h^{BL} . Then, we corrected the obtained values with the ratio $\frac{Re_h^{BL}}{Re_h^{CH}} = 0.31$ to estimate a suitable roughness d for the channel flow. Table 5.1 presents a brief summary. The swimming speed of the white shark has also been considered.

Instead, table 5.2 is a summary of the parameters used to obtain the present results. The pressure gradient and the centre-line velocity have been calculated with the kinematic viscosity of the water $\nu_H = 10^{-6} m^2/s$ and with $Re = 5772$.

5.2.2 Rectangular grooves

The results obtained are, once again, compatible with the researches of Moradi and Floryan [32] and Ehrenstein [12]. The longitudinal grooves cause a destabilization of the flow in the channel, reducing the critical Reynolds number. The destabilization effect is more significant as the dimension of the grooves increases, that is for greater roughness values and groove wavelengths. The critical Reynolds number for $d = 0.01$ and $d = 0.02$ is slightly lower with respect to the plane channel, however, for $d = 0.05$, it drops to $Re \approx 5000$ and to $Re < 4500$ for $d = 0.1$ (see figure 5.7).

Parameters	Rectangular grooves					Triangular grooves										
	h	s	λ	β	a	d	G_z	U_d	h	s	λ	β	a	d	G_z	U_d
Channel half-height	mm															
Groove span	μm	50	50	50	50	50	50	50	50	50	50	50	50	50	50	50
Groove wavelength	-	0.02	0.04	0.1	0.2	0.01	0.02	0.05	0.1	0.01	0.02	0.05	0.1	0.01	0.02	0.05
Groove wavenumber	-	314	157	62.8	31.4	628	314	125.6	62.8	628	314	125.6	62.8	628	314	125.6
Groove amplitude	μm	50	50	50	50	43.3	43.3	43.3	43.3	43.3	43.3	43.3	43.3	43.3	43.3	43.3
Roughness	-	0.01	0.02	0.05	0.1	0.01	0.02	0.05	0.1	0.01	0.02	0.05	0.1	0.01	0.02	0.05
Pressure gradient	Pa/m	-92	-739	-11544	-92352	-92	-739	-11544	-92352	-92	-739	-11544	-92352	-92	-739	-11544
Centre-line velocity	m/s	1.15	2.31	5.77	11.54	1.15	2.31	5.77	11.54	1.15	2.31	5.77	11.54	1.15	2.31	5.77

Table 5.2: Reference table of dimensional problems and corresponding dimensionless parameters.

In figure 5.5 we see the eigenvalue spectra. It is clearly visible the dependency of the eigenvalues distribution on the size of the mesh, especially the section width L , as already discussed in Section 4.2.2. In the dimensionless problem, the channel half-height is fixed, therefore if the groove dimension varies, the section width L must also vary to consider the same number of grooves. However, even with the introduction of new modes, the shift $\xi_A = 0.01 - 0.264i$ guarantees that the dominant eigenvalue is always among the calculated eigenvalues.

5.2.3 Triangular grooves

The results obtained for the triangular grooves are almost the same as for the rectangular ones. The channel flow is destabilized by the longitudinal grooves, however the critical Reynolds number decrease seems to be less significant than for the rectangular grooves. While it is similar for the roughness values $d = 0.01$ and $d = 0.02$, for $d = 0.05$ it is around $Re \approx 5250$ and for $d = 0.1$ it drops to $Re \approx 4500$ (see figure 5.8).

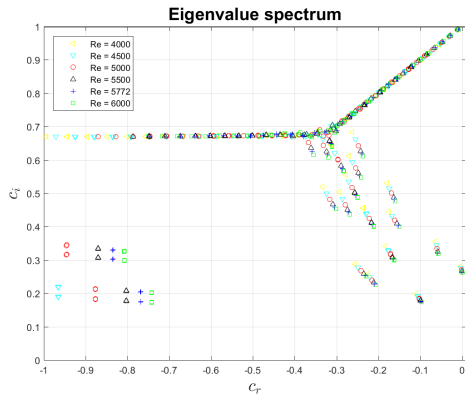
From figure 5.6 we notice that the deformation of the spectrum is less evident than that for the rectangular grooves with the same roughness. This is just because the triangular grooves have half the wavelength of the rectangular ones for fixed d and therefore the considered section has also half width. This fact is also highlighted by figure 5.5a and figure 5.6b, where the superposition of the original S and A branches by new modes is almost the same.

5.3 Neutral curve

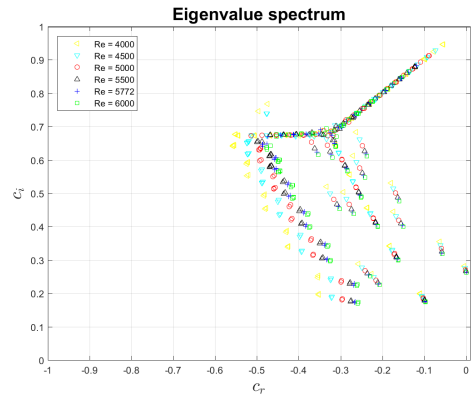
The results presented in Section 5.2 are enriched by drawing the approximate neutral curves in the $(Re - \kappa)$ plane. Each curve has been linearly interpolated from five sample points, with the exception of the curve for the rectangular grooves of roughness $d = 0.05$ for which seven sample points have been used. The linear interpolation is the less accurate, but it has been chosen to underline the fact that these are just approximated curves, due to the large amount of calculations required to increase the resolution and the accuracy.

For Reynolds numbers greater than the critical value, there are two points in the $(Re - \kappa)$ plane which lie on the neutral curve. For some Reynolds numbers these points have been located by approximating the function $\omega_r = \omega_r(\kappa)|_{Re=const}$ from three samples computed for $\kappa_1 > 1.02$ and $\kappa_2 < 1.02$ in the stable zone and $\kappa_3 = 1.02$ in the unstable zone. This choice has been made to ensure that the two points of the neutral curve $\omega_r(\kappa)|_{Re=const} = 0$ belonged to the considered κ interval. Instead, the critical Reynolds number for $\kappa = 1.02$ has been evaluated from the results presented in Section 5.2.

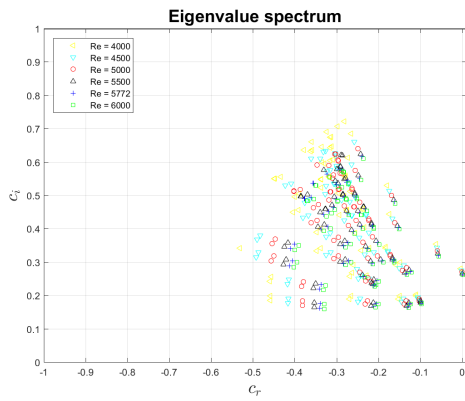
The neutral curves are fairly similar to the analogous curves for the plane channel. The critical Reynolds number decreases as the roughness d and the groove wavelength λ increase. Furthermore, for a given Reynolds number, the range of disturbance wavenumber κ in the unstable zone is wider for higher roughness. As we already observed from the results presented in Section 5.2, the difference in critical Reynolds number between the rectangular grooves and the triangular grooves is more evident for $d = 0.05$ than $d = 0.02$. Moreover, the approximate slope of the neutral curve for the rectangular grooves is slightly higher than for the triangular ones.



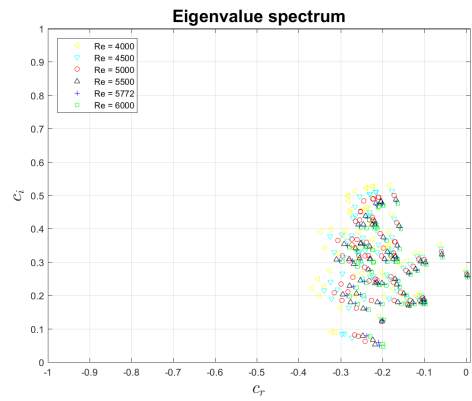
(a) Eigenvalue spectrum for $d = 0.01$ and $\lambda = 0.02$.



(b) Eigenvalue spectrum for $d = 0.02$ and $\lambda = 0.04$.

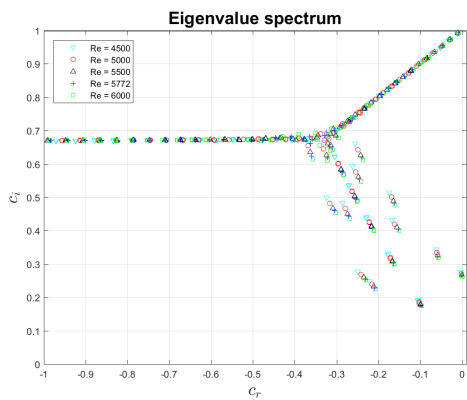


(c) Eigenvalue spectrum for $d = 0.05$ and $\lambda = 0.1$.

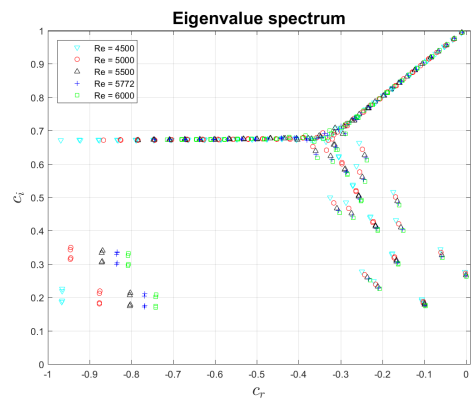


(d) Eigenvalue spectrum for $d = 0.1$ and $\lambda = 0.2$.

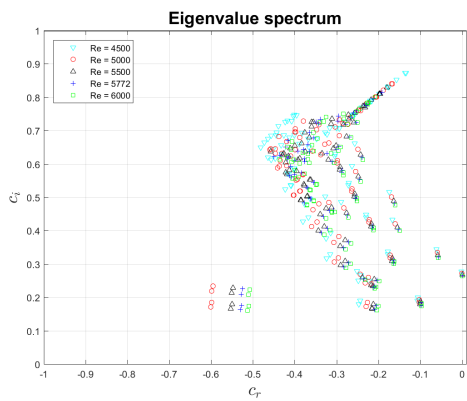
Figure 5.5: Eigenvalue spectra for the channel flow with longitudinal rectangular grooves for different roughness values.



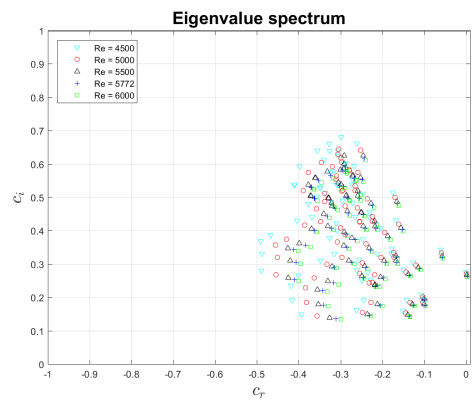
(a) Eigenvalue spectrum for $d = 0.01$ and $\lambda = 0.01$.



(b) Eigenvalue spectrum for $d = 0.02$ and $\lambda = 0.02$.



(c) Eigenvalue spectrum for $d = 0.05$ and $\lambda = 0.05$.



(d) Eigenvalue spectrum for $d = 0.1$ and $\lambda = 0.1$.

Figure 5.6: Eigenvalue spectra for the channel flow with longitudinal triangular grooves for different roughness values

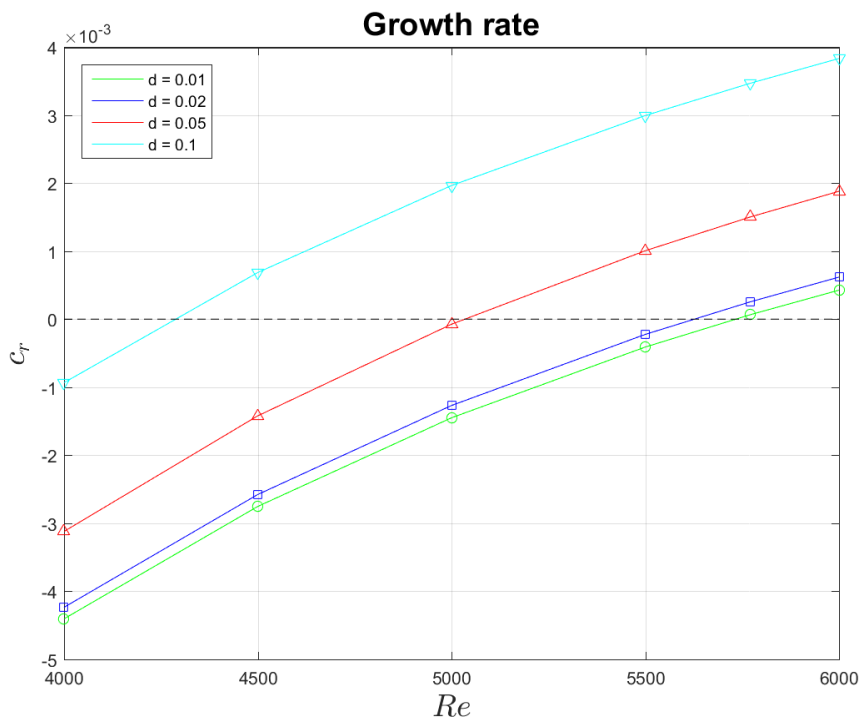


Figure 5.7: Growth rate of the most unstable eigenvalue as a function of the Reynolds number for several roughness values. Rectangular grooves. $\kappa = 1.02$.

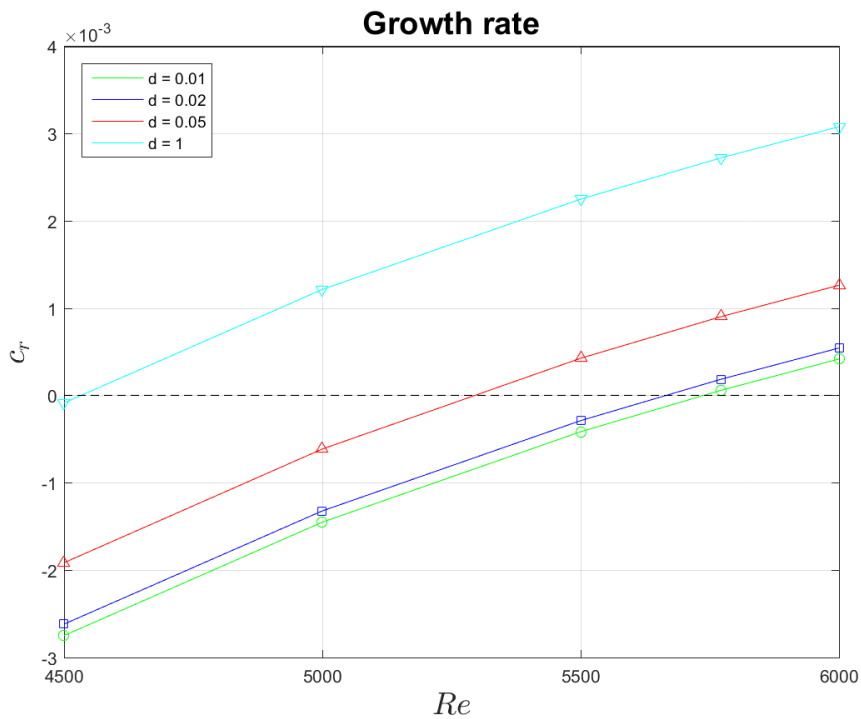


Figure 5.8: Growth rate of the most unstable eigenvalue as a function of the Reynolds number for several roughness values. Triangular grooves. $\kappa = 1.02$.

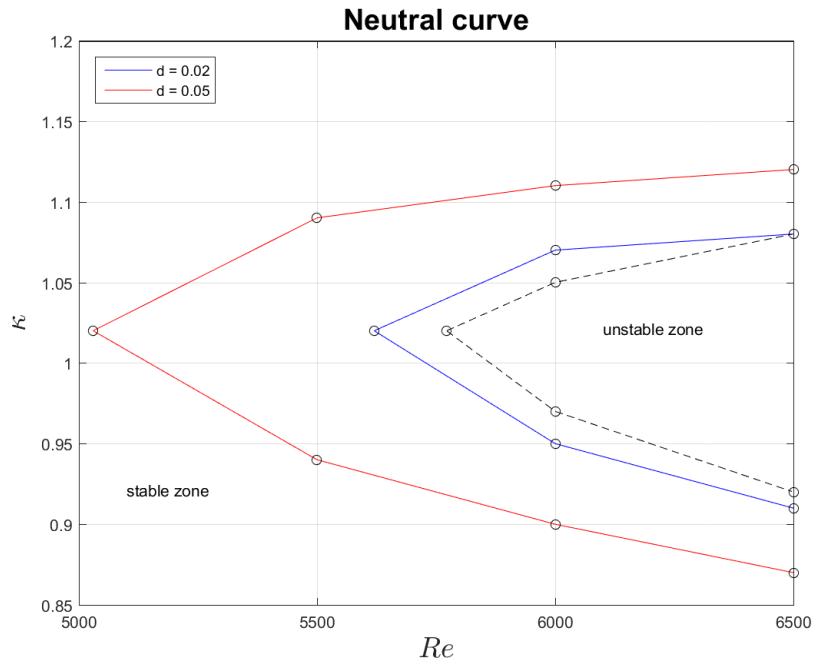


Figure 5.9: Neutral curve in the $(Re - \kappa)$ plane for rectangular grooves of roughness $d = 0.02$ and $d = 0.05$. The black dashed line represents the approximate neutral curve of the channel with smooth walls.

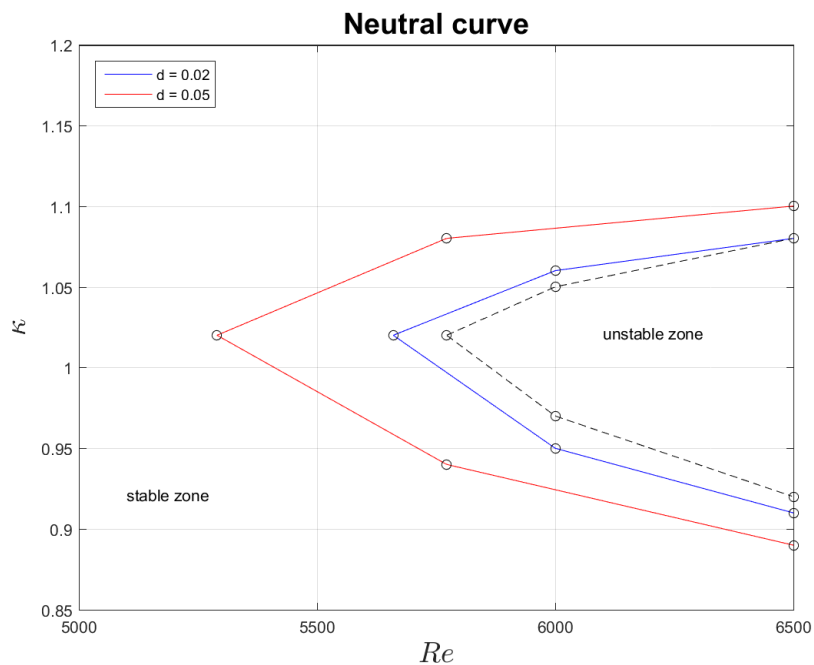


Figure 5.10: Neutral curve in the $(Re - \kappa)$ plane for triangular grooves of roughness $d = 0.02$ and $d = 0.05$. The black dashed line represents the approximate neutral curve of the channel with smooth walls.

5.4 Eigenfunctions

This section is dedicated to the analysis of the dominant eigenfunction. To carry out a meaningful comparison of the results obtained with different geometries, the three components of the eigenfunction have been normalized, in fact they are defined up to a complex multiplicative constant. The most convenient choice is the integral mean of the wall-normal component \hat{v} , whose real and imaginary part read

$$I_r = \frac{1}{\Omega} \int_{\Omega} \hat{v}_r, \quad I_i = \frac{1}{\Omega} \int_{\Omega} \hat{v}_i, \quad (5.2)$$

where Ω is the two-dimensional domain corresponding to the channel section. With equations (5.2) we can then write

$$\bar{\mathbf{u}} = \bar{\mathbf{u}}_r + i\bar{\mathbf{u}}_i = \frac{\hat{\mathbf{u}}_r + i\hat{\mathbf{u}}_i}{I_r + iI_i}, \quad (5.3)$$

where $\hat{\mathbf{u}}_r$ and $\hat{\mathbf{u}}_i$ represent the real and imaginary part of the unnormalized eigenfunction. By multiplying and dividing by the complex conjugate of the normalization coefficient, we can separate the real and imaginary part obtaining

$$\bar{\mathbf{u}}_r + i\bar{\mathbf{u}}_i = \frac{\hat{\mathbf{u}}_r I_r + \hat{\mathbf{u}}_i I_i}{I_r^2 + I_i^2} + i \frac{\hat{\mathbf{u}}_i I_r - \hat{\mathbf{u}}_r I_i}{I_r^2 + I_i^2}. \quad (5.4)$$

The results presented in this section regard only the real part $\bar{\mathbf{u}}_r$ of the normalized eigenfunction. Even if the perturbation of the flow is three-dimensional, we limit our analysis to the xy plane, that is the domain on which the results have been obtained.

In all the examined cases, the profile of the wall-normal component \bar{v}_r is almost identical, as shown in figure 5.11, with the exception of the area near and inside the grooves. \bar{v}_r is the predominant component in the central part of the channel. On the other hand, we can observe from figure 5.12 that close to the channel walls the streamwise component becomes predominant instead, especially inside the grooves. The extent of the peak of the streamwise component \bar{w}_r depends on shape and dimension of the grooves, to the point of becoming comparable to the maximum of the wall-normal component for rectangular grooves with $d = 0.1$. It can be also noticed that, as the dimension of the grooves increases, the location of the \bar{w}_r maximum moves inside the grooves themselves. For $d = 0.05$ and $d = 0.1$, the outcome is the formation of zones inside the grooves where the flow is practically directed in the z direction. These structures can be clearly observed in figures 5.15b, 5.16b, 5.19b and 5.20b. For $d = 0.01$ and $d = 0.02$ instead, the streamwise component peak is just above the groove tip and it is spanwise constant, as shown in figures 5.13b, 5.14b, 5.17b and 5.18b.

Figure 5.21 is the representation of the three components separately for $d = 0.1$. The spanwise component is null almost everywhere, except for alternate negatives and positive peaks around the edges of the grooves. However, these peaks remain under the level of 5% of the maximum of the wall-normal component, therefore we can assert that the spanwise component does not contribute to the magnitude of the eigenfunction vector $\bar{\mathbf{u}}_r$. In figures 5.21e and 5.21f we can observe that the negative peak of the streamwise component is still spanwise constant for the triangular grooves while it is not for the rectangular ones.

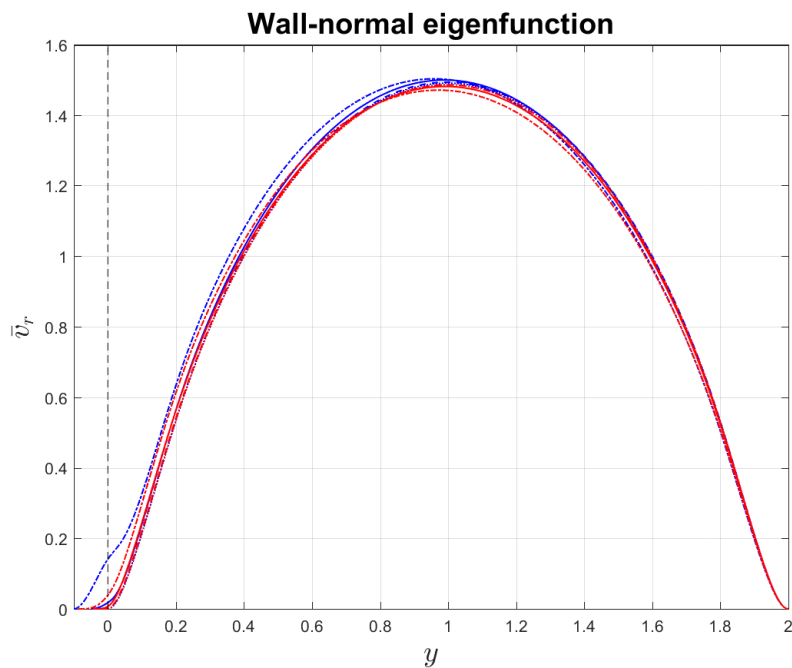


Figure 5.11: Profile of the normalized wall-normal component \bar{v}_r taken at the midspan line of the section. Rectangular grooves (blue) and triangular grooves (red). Roughness $d = 0.01$ (dotted line), $d = 0.02$ (dashed line), $d = 0.05$ (solid line), $d = 0.1$ (dashed-dotted line). The black dashed line shows the groove-tip height.

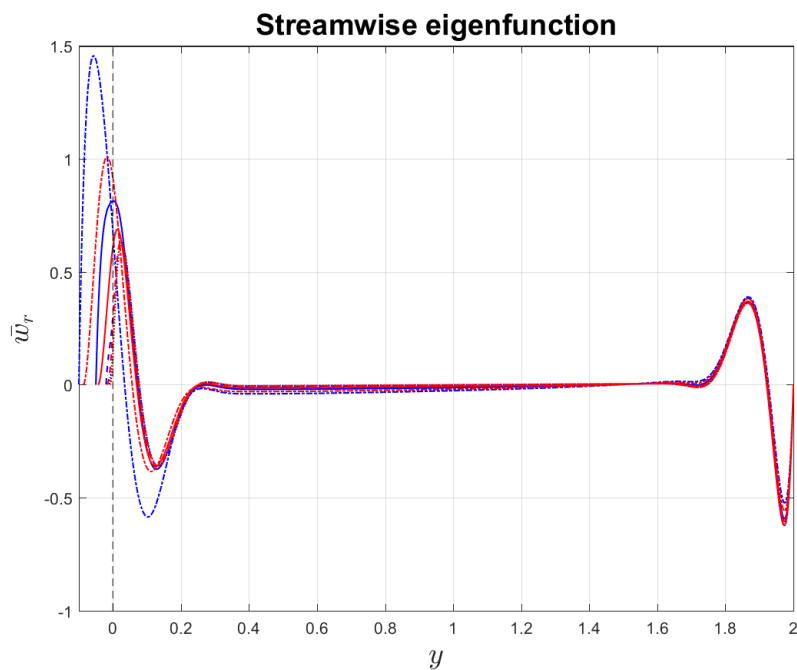


Figure 5.12: Profile of the normalized streamwise component \bar{w}_r taken at the midspan line of the section. Rectangular grooves (blue) and triangular grooves (red). Roughness $d = 0.01$ (dotted line), $d = 0.02$ (dashed line), $d = 0.05$ (solid line), $d = 0.1$ (dashed-dotted line). The black dashed line shows the groove-tip height.

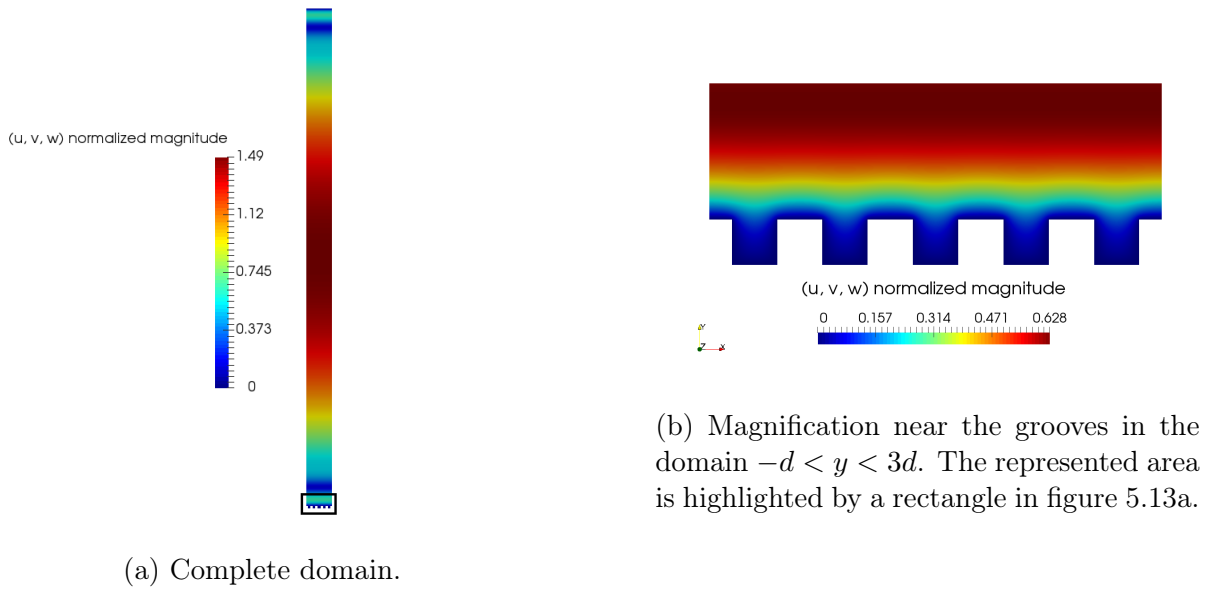


Figure 5.13: Magnitude of the normalized eigenfunction $\bar{\mathbf{u}}_{\mathbf{r}}$. Rectangular grooves with $d = 0.01$ and $\lambda = 0.02$.

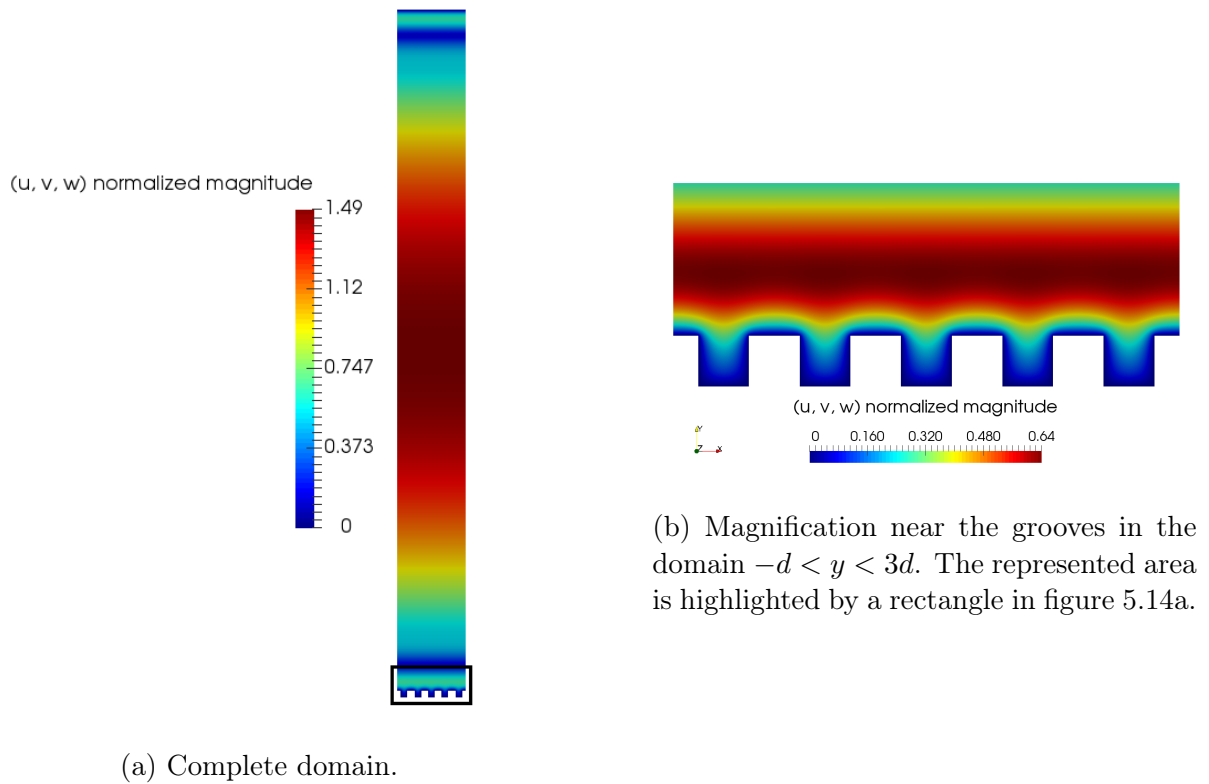
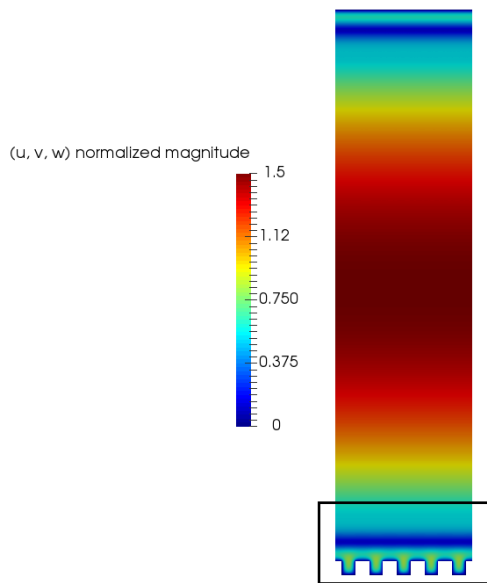
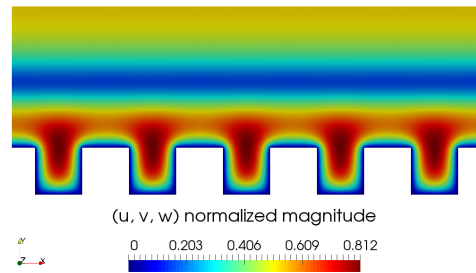


Figure 5.14: Magnitude of the normalized eigenfunction $\bar{\mathbf{u}}_{\mathbf{r}}$. Rectangular grooves with $d = 0.02$ and $\lambda = 0.04$.

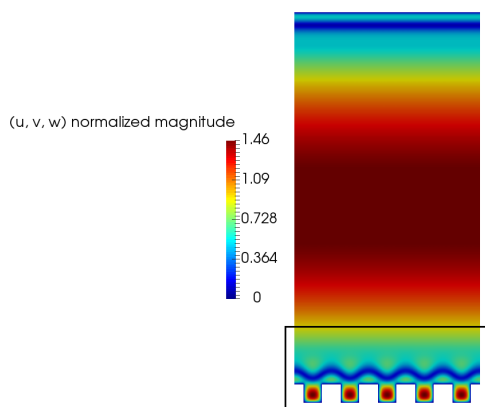


(a) Complete domain.

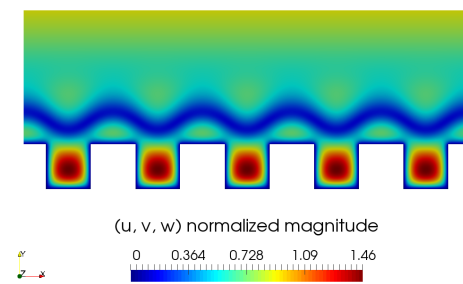


(b) Magnification near the grooves in the domain $-d < y < 3d$. The represented area is highlighted by a rectangle in figure 5.15a.

Figure 5.15: Magnitude of the normalized eigenfunction $\bar{\mathbf{u}}_{\mathbf{r}}$. Rectangular grooves with $d = 0.05$ and $\lambda = 0.1$.



(a) Complete domain.



(b) Magnification near the grooves in the domain $-d < y < 3d$. The represented area is highlighted by a rectangle in figure 5.16a.

Figure 5.16: Magnitude of the normalized eigenfunction $\bar{\mathbf{u}}_{\mathbf{r}}$. Rectangular grooves with $d = 0.1$ and $\lambda = 0.2$.

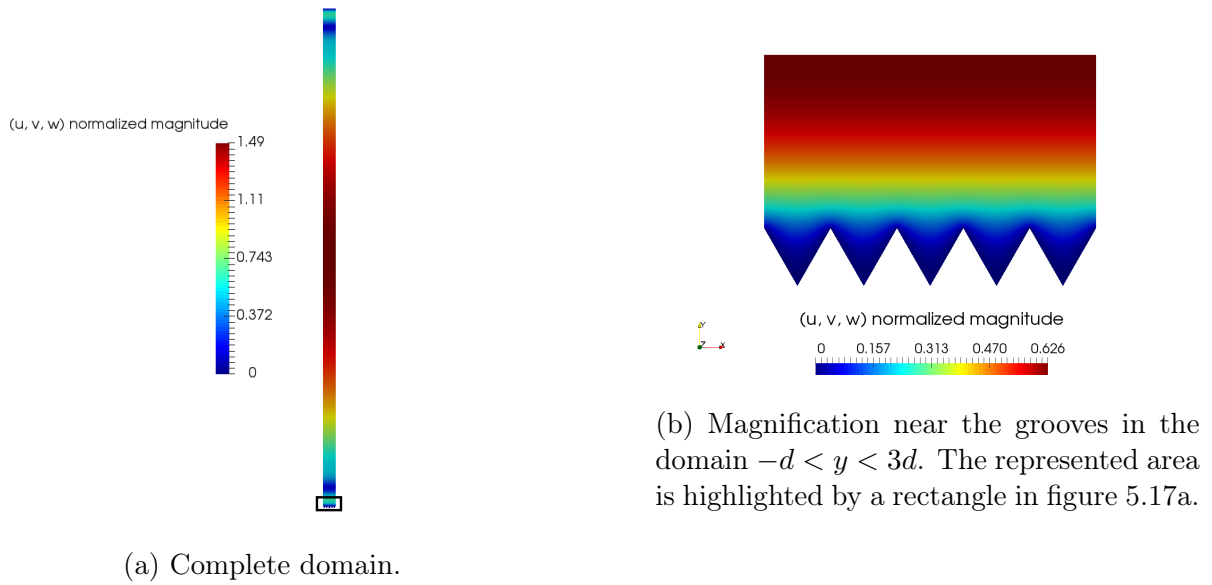


Figure 5.17: Magnitude of the normalized eigenfunction $\bar{\mathbf{u}}_{\mathbf{r}}$. Triangular grooves with $d = 0.01$ and $\lambda = 0.01$.

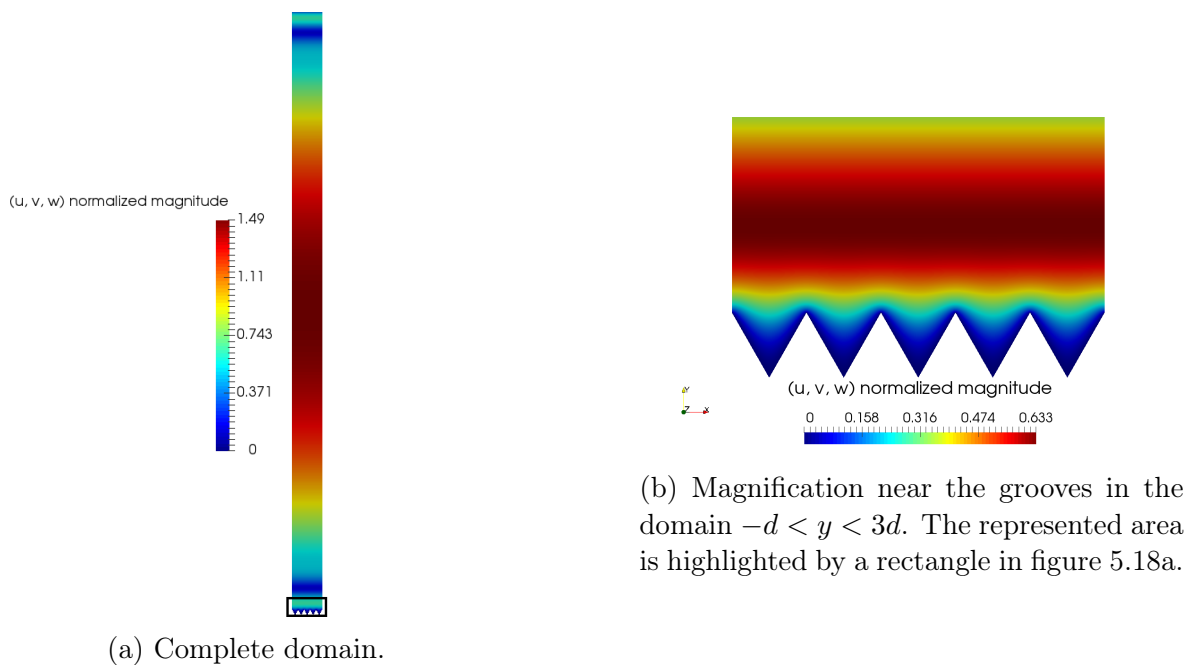
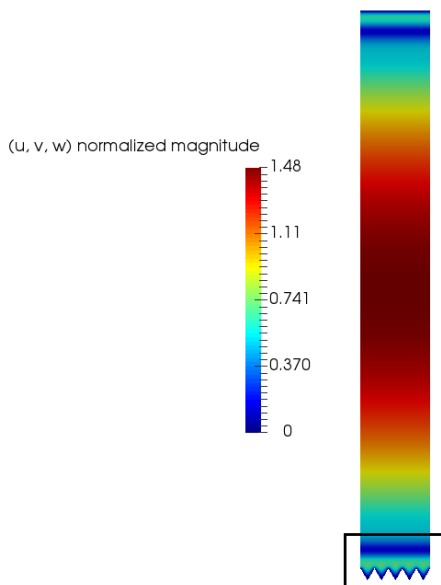
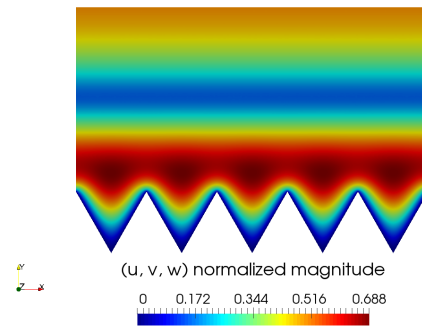


Figure 5.18: Magnitude of the normalized eigenfunction $\bar{\mathbf{u}}_{\mathbf{r}}$. Triangular grooves with $d = 0.02$ and $\lambda = 0.02$.

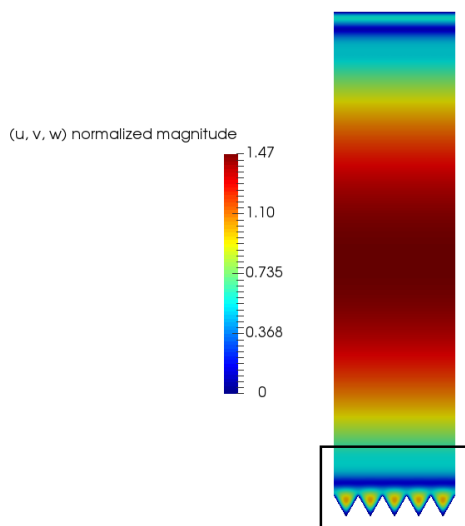


(a) Complete domain.

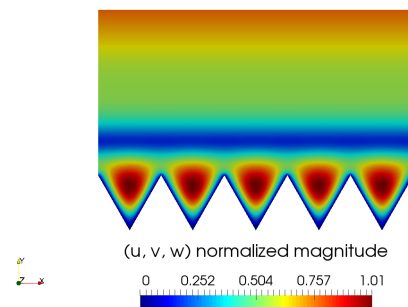


(b) Magnification near the grooves in the domain $-d < y < 3d$. The represented area is highlighted by a rectangle in figure 5.19a.

Figure 5.19: Magnitude of the normalized eigenfunction $\bar{\mathbf{u}}_{\mathbf{r}}$. Triangular grooves with $d = 0.05$ and $\lambda = 0.05$.

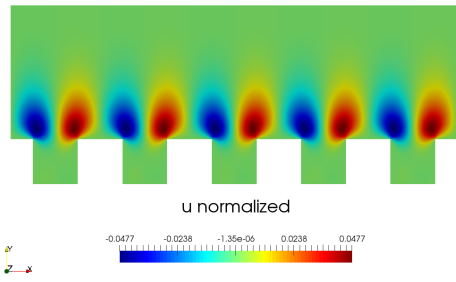


(a) Complete domain.

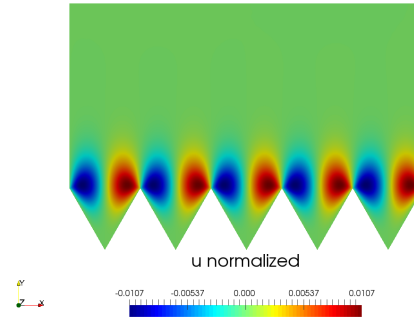


(b) Magnification near the grooves in the domain $-d < y < 3d$. The represented area is highlighted by a rectangle in figure 5.20a.

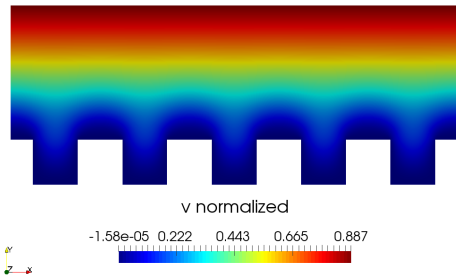
Figure 5.20: Magnitude of the normalized eigenfunction $\bar{\mathbf{u}}_{\mathbf{r}}$. Triangular grooves with $d = 0.1$ and $\lambda = 0.1$.



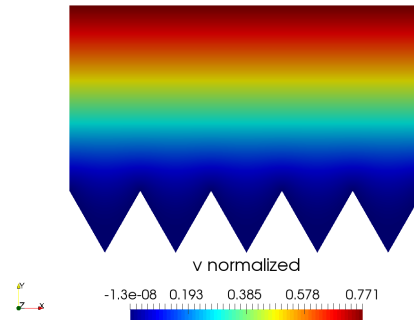
(a) Spanwise component \bar{u}_r . Rectangular grooves $d = 0.1$.



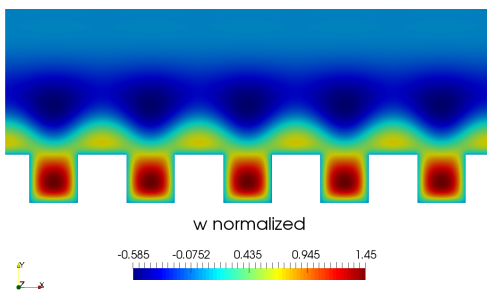
(b) Spanwise component \bar{u}_r . Triangular grooves $d = 0.1$.



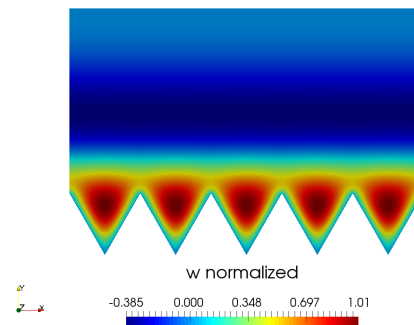
(c) Wall-normal component \bar{v}_r . Rectangular grooves $d = 0.1$.



(d) Wall-normal component \bar{v}_r . Triangular grooves $d = 0.1$.



(e) Streamwise component \bar{w}_r . Rectangular grooves $d = 0.1$.



(f) Streamwise component \bar{w}_r . Triangular grooves $d = 0.1$.

Figure 5.21: Normalized eigenfunction components \bar{u}_r , \bar{v}_r and \bar{w}_r for rectangular and triangular grooves with $d = 0.1$ near the grooved wall.

5.5 SH channel base flow

This section focuses on the analysis of the base flow in a channel with SH longitudinal grooves, that is the longitudinal grooves filled with air bubbles. In this analysis we consider only the micro-structured roughness and we suppose that the nano-structured roughness of the grooves has been appropriately designed to obtain a contact angle $\theta = 170^\circ$ ($\alpha = 10^\circ$). The analysis of the base flow is a mandatory step, before proceeding to the linear stability analysis of the flow: modifications in the base-flow profile induced by the air bubble could have great influence on the stability characteristics of the flow. All the results presented in this section have been obtained with $d = 0.05$ and $\lambda = 0.1$ for rectangular grooves or $\lambda = 0.05$ for triangular grooves. Figures 5.22 and 5.23 show the spanwise stations for which the base flow profile has been examined.

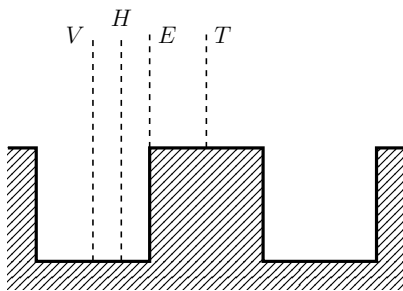


Figure 5.22: Spanwise stations reference used for plotting the velocity profiles for rectangular grooves.

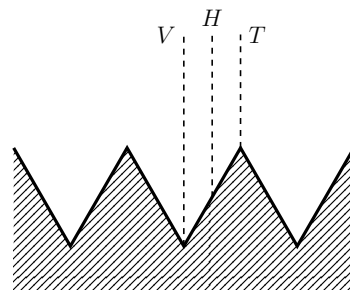


Figure 5.23: Spanwise stations used for plotting the velocity profiles for triangular grooves.

A first look of the profile on the whole channel height reveals that it is quite similar to the parabolic Poiseuille profile. If we compare the profile corresponding to the midspan line of a groove valley, that is station V, and the midspan line of a groove tip, that is station T, they are practically the same, with the exception of the area around the groove. If the grooves are small enough, the velocity profile far from them is not affected. In the validation process 4.5, the groove dimension was exaggerated on purpose to check the accuracy of the result, therefore the modification of the whole profile was more apparent. These considerations are valid for both the rectangular grooves (figure 5.24) and the triangular grooves (figure 5.25).

It is more interesting to observe more closely how the base-flow profile differs from the Poiseuille profile in the area near the grooved wall. In figure 5.26 and 5.27 we can see the comparison between the profiles in a channel with grooves and a single fluid and a channel with a multi-phase flow over SH surfaces. In the case of triangular grooves the profiles taken at different spanwise stations are practically the same. However, in the case of rectangular grooves, the difference between the profiles is more evident, especially inside the valley of the groove. It is also worth noticing that, at the edge of the groove (station E), $W(y) = 0$ for $y = 0$ is reached more slowly than station T. This profile is similar to the one for the triangular grooves, where the only point at the tip is also the edge point.

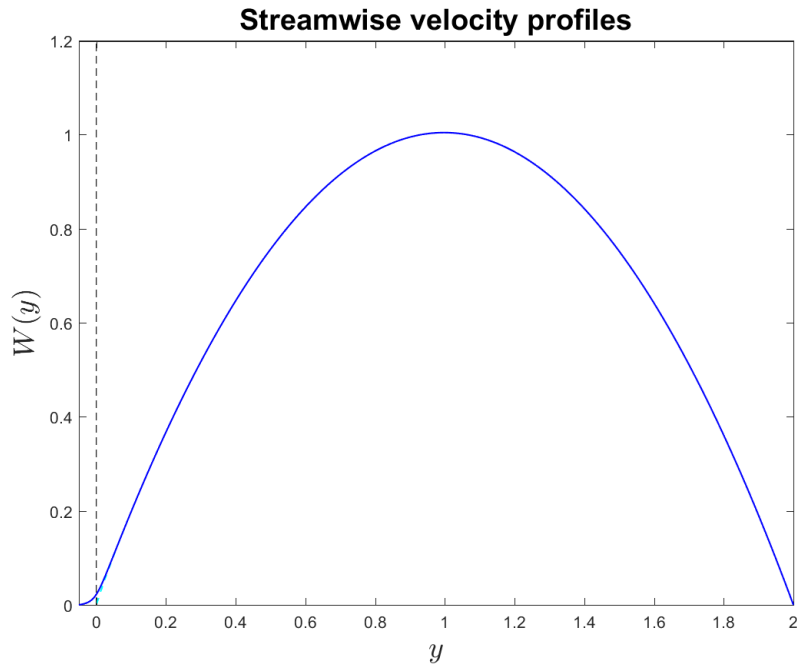


Figure 5.24: Velocity profiles in a channel with SH rectangular grooves. Profiles taken at station V (blue solid line) and station T (cyan dashed line). The black dashed line shows the grooves tip height.

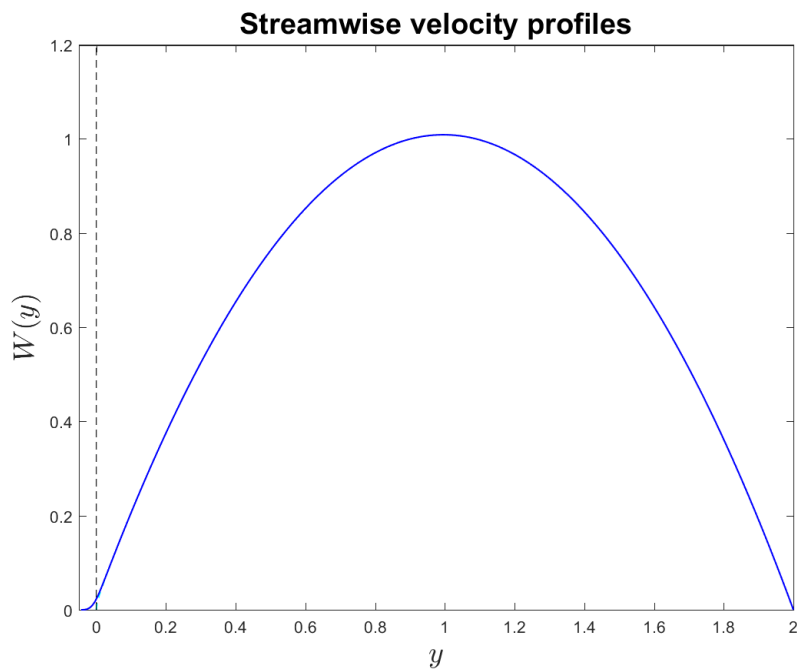


Figure 5.25: Velocity profiles in a channel with SH triangular grooves. Profiles taken at station V (blue solid line) and station T (cyan dashed line). The black dashed line shows the grooves tip height.

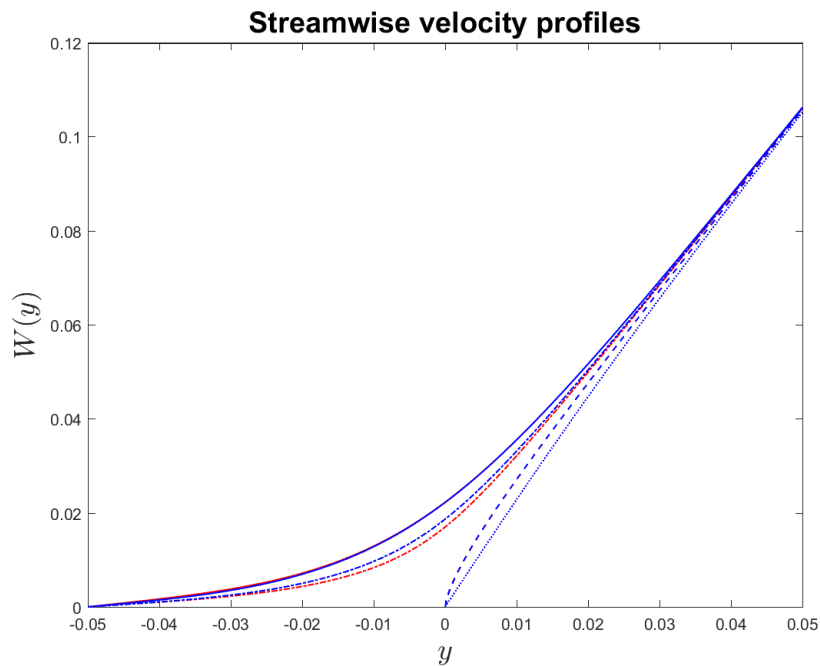


Figure 5.26: Magnification of the velocity profiles near the grooved wall (rectangular grooves). Comparison between the single-phase flow (red) and the multi-phase flow (blue). Profiles taken at station V (solid line), station H (dashed-dotted line), station E (dashed line) and station T (dotted line).

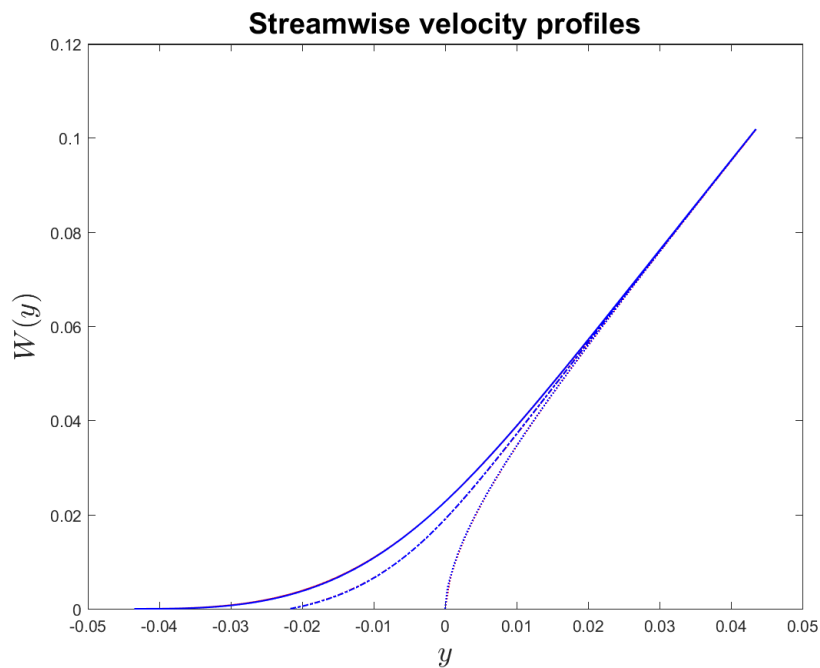


Figure 5.27: Magnification of the velocity profiles near the grooved wall (triangular grooves). Comparison between the single-phase flow (red) and the multi-phase flow (blue). Profiles taken at station V (solid line), station E (dashed-dotted line) and station T (dotted line).

Chapter 6

Conclusions and future work

In the present work we performed a linear stability analysis of the flow in a plane channel with a grooved wall. This study was motivated by the need of an in-depth analysis of the stability of the flow over longitudinal grooves with the purpose of designing a surface that combines the drag reduction properties of riblets and SH surfaces. For SH surfaces, this property derives from a double-hierarchical roughness, which is capable of trapping air bubbles inside the asperities of the solid wall and maintaining a stable Cassie wetting state.

The flow dynamics has been modeled with the incompressible dimensionless Navier-Stokes equations. The first step was to introduce into the equations the simplification allowed by the problem geometry, thus obtaining the Poisson problem for the base flow. Then the equations have been linearized and the eigenvalue problem has been defined. We have then applied the Finite Element Method to the weak formulation and built the matrices necessary to solve the eigenvalue problem. The whole procedure has been implemented in a mixed *C++/Fortran90* software exploiting the features of the *FEniCS* package [39]. The base-flow solver has been validated on the Poiseuille flow, whose analytical solution is well known [36]. The eigenvalue solver instead has been validated with established solutions of the Orr-Sommerfeld equation. In the multi-phase problem, the interface between the fluids has been modelled with the Young-Laplace equation. This equation is non-linear and required a numerical integration that combines a shooting method and a quasi-Newton iterative method to be solved.

The present work demonstrated that the results obtained for rectangular and triangular longitudinal grooves are compatible with the results obtained for sinusoidal grooves by Moradi and Floryan [32] and for semicircular riblets by Ehrenstein [12]. The longitudinal grooves with reasonable amplitude and wavelength promote instability by reducing the critical Reynolds number and by enlarging the unstable zone delimited by the neutral curve in the $(Re - \kappa)$ plane. The control parameters have been estimated by establishing an analogy between the channel flow and the boundary layer flow. The computation of the base flow for the multi-phase problem with the air bubbles inside the grooves revealed that the velocity profiles are quite similar to the single-phase problem.

The results obtained in the present work represent the first phase of the study of this complex problem and they are fundamental for the development of drag reduction methods with SH longitudinal grooves. Hereafter, we provide a brief description of possible extensions to the present work.

-
- **Linear stability analysis of the multi-phase problem.** This is the clearest extension of this work, already outlined with the computation of the base flow. The presence of air bubbles trapped inside the grooves involves rewriting system 2.11 taking into account two different subdomains Ω_c and Ω_b on which two different Reynolds numbers are defined, Re_{water} and Re_{air} respectively. It must be also taken into consideration that the interface between the two fluids, that is the internal boundary, can distort. This can be achieved by transforming the reference frame moving with the fluids \mathbf{x} into a fixed reference frame \mathbf{x}_0 introducing into the equations all the required differential operators in transformed coordinates. To apply all these considerations in the *C++/Fortran90* software, the UFL file of the weak formulation must be modified suitably. If needed, the *FEniCS* package includes tools to modify already built meshes.
 - **Linear stability analysis of the boundary layer flow.** The analysis of the boundary layer problem is necessary to develop the SH surface concept and to obtain enough data for practical applications in the naval or aeronautical industry. The developed software can be adapted by modifying the UFL file and the boundary conditions appropriately.
 - **Linear stability analysis of the pipe flow.** This scenario involves considering a pipe flow instead of a plane channel flow. The longitudinal grooves are no more located on a flat surface but on a circular surface, therefore it is useful to write the equations in cylindrical coordinates. Particularly interesting could be the analysis of the multi-phase problem for which the main fluid is not water but oil or natural gas.
 - **Space-time analysis.** The flow can have three types of responses to a localized initial disturbance. The amplitude may asymptotically decay in time in the entire domain, the flow is then stable. The flow is linearly absolutely unstable if the disturbance is amplified at the source and gradually contaminates the entire domain. If the disturbance is advected away from the source the flow is then said to be linearly convectively unstable. The analysis performed in the present work identifies if the flow is stable or not but cannot distinguish between absolute instability and convective instability. To make this distinction, the wavelike disturbances 2.10 must be rewritten with $\omega \in \mathbb{C}$ and $\kappa \in \mathbb{C}$ and then the asymptotic behaviour of the impulse response has to be examined. The impulse response is dominated by the complex absolute wavenumber κ_0 and the complex absolute frequency ω_0 [21]. If the basic state is unstable ($\omega_{r,\max} > 0$) and $\omega_{0,r} < 0$ the instability is convective. If the basic state is unstable ($\omega_{r,\max} > 0$) and $\omega_{0,r} > 0$ the instability is absolute.
 - **Drag reduction comparison between riblets and SH surfaces.** The riblets and the SH surfaces, as already mentioned, could reduce the skin-friction drag portion of the total drag force. An interesting analysis could be a direct comparison of the drag reducing effect of the riblets in a single phase problem and of the SH grooves. To achieve this, we could evaluate the local wall viscous stress τ_w and consequently the friction coefficient c_f . To obtain comparable results, these values must be integrated over a control domain.

The described extensions demonstrate how the problem of drag reduction exploiting riblets and SH surfaces, and in general the problem of hydrodynamic instability, is still fairly unexplored and a suitable theoretical knowledge must be built before actual technological applications can be taken into consideration.

Appendix A

Orr-Sommerfeld equation

The Orr-Sommerfeld equation is an eigenvalue equation describing the two-dimensional modes of disturbance in a viscous parallel flow. To be coherent with the notation of Schmid and Henningson [40], we write this flow as $U = U(y)$, with U the streamwise component of the velocity. Adapting equations (2.9) to this notation, the system becomes:

$$\begin{cases} \frac{\partial \tilde{u}}{\partial t} + U \frac{\partial \tilde{u}}{\partial x} + \tilde{v} \frac{dU}{dy} - \frac{1}{Re} \nabla^2 \tilde{u} + \frac{\partial \tilde{p}}{\partial x} = 0, \\ \frac{\partial \tilde{v}}{\partial t} + U \frac{\partial \tilde{v}}{\partial x} - \frac{1}{Re} \nabla^2 \tilde{v} + \frac{\partial \tilde{p}}{\partial y} = 0, \\ \frac{\partial \tilde{w}}{\partial t} + U \frac{\partial \tilde{w}}{\partial x} - \frac{1}{Re} \nabla^2 \tilde{w} + \frac{\partial \tilde{p}}{\partial z} = 0, \\ \frac{\partial \tilde{u}}{\partial x} + \frac{\partial \tilde{v}}{\partial y} + \frac{\partial \tilde{w}}{\partial z} = 0. \end{cases} \quad (\text{A.1})$$

Taking the divergence of the linearized momentum equations and using the continuity equation yields an equation for the perturbation pressure:

$$\nabla^2 \tilde{p} = -2 \frac{dU}{dy} \frac{\partial \tilde{v}}{\partial x} \quad (\text{A.2})$$

This equation may be used with the second equation of system (A.1), thus eliminating \tilde{p} , to obtain an equation for the normal velocity, \tilde{v} :

$$\left[\left(\frac{\partial}{\partial t} + U \frac{\partial}{\partial x} \right) \nabla^2 - \frac{d^2 U}{dy^2} \frac{\partial}{\partial x} - \frac{1}{Re} \nabla^4 \right] \tilde{v} = 0. \quad (\text{A.3})$$

Introducing in equation (A.3) a solution of the form

$$\tilde{v}(x, y, z, t) = \hat{v}(y) e^{i(\alpha x - \omega t)}, \quad (\text{A.4})$$

with $\omega \in \mathbb{C}$ the frequency and $\alpha \in \mathbb{R}$ the streamwise wavenumber, we obtain the following equation for \hat{v} :

$$\left[(-i\omega + i\alpha U)(\mathcal{D}^2 - \alpha^2) - i\alpha \frac{d^2 U}{dy^2} - \frac{1}{Re} (\mathcal{D}^2 - \alpha^2)^2 \right] \hat{v} = 0, \quad (\text{A.5})$$

with the boundary conditions $\hat{v} = 0$ and $\mathcal{D}\hat{v} = 0$ at the solid walls; \mathcal{D} represents the derivative with respect to the wall-normal direction y .

The equation for the normal velocity (A.5) is called Orr-Sommerfeld equation. The frequency ω appears as the eigenvalue. Each eigenvalue ω_j , together with the corresponding eigenfunction \hat{v}_j , represents an Orr-Sommerfeld mode.

To solve the three-dimensional problem, equation (A.3) must be coupled with the equation for the normal vorticity, which, with the introduction of a wavelike solution, leads to the Squire equation. The Squire equation, differently from the Orr-Sommerfeld equation, is non-homogeneous and is forced by the Orr-Sommerfeld solutions.

Appendix B

UFL code

This section is dedicated to the description of the UFL code corresponding to the weak formulation of the eigenvalue problem (3.13). To better understand how the UFL language works and why it is so useful to express complex mathematical problems, each section of the UFL code concerning the development of the software used in the present work will be described in detail.

- The first operation is the definition of a mixed discrete function space V as a set of function spaces for each variable. For programming convenience, in the present case we chose to consider the vectorial velocity field as three separate scalar unknowns. For each function space, we must specify the cell shape, the finite element family and the number of degrees of freedom. The mixed function space is then defined by the combination of three functions spaces suitable for the velocity field PU (\mathbb{P}^2 Lagrange polynomials) and one function space suitable for the pressure field PP (\mathbb{P}^1 Lagrange polynomials).

```
PU = FiniteElement("Lagrange",triangle,2)
PP = FiniteElement("Lagrange",triangle,1)

V = MixedElement([PU, PU, PU, PP])
```

- The next step is the definition of the trial and test functions over the function space V .

```
(u, v, w, p) = TrialFunctions(V)
(phix, phiy, phiz, psi) = TestFunctions(V)
```

The variable notation is the same used in system (3.13).

- Before writing the equations we must also define all the necessary coefficients and constants. In the present case they are the base-flow velocity field, computed with its own UFL form, the Reynolds number and the disturbance wavenumber. The value of these variables must defined and assigned to the forms in the main *C++* code.

```
W = Coefficient(PU)
Re = Constant(triangle)
kappa = Constant(triangle)
```

-
- The UFL language is not capable of dealing with complex numbers, therefore the real and imaginary parts of the jacobian matrix have been implemented in two separate forms and later merged with the *Fortran90* code. The mass matrix has its own form as well. The basic algebraic operations can be used freely in UFL expressions. Basic nonlinear functions and spatial derivatives are also available. The integration over a domain is expressed by multiplication with a measure, and UFL defines the measure dx for the cell integral. Many other features are available but were not necessary in the present work [39].

```

A =-( 1/Re*phix.dx(0)*u.dx(0)*dx + 1/Re*phix.dx(1)*u.dx(1)*dx +
      1/Re*phix*pow(kappa,2)*u*dx - p*phix.dx(0)*dx\

      + 1/Re*phiy.dx(0)*v.dx(0)*dx + 1/Re*phiy.dx(1)*v.dx(1)*dx +
      1/Re*phiy*pow(kappa,2)*v*dx - p*phiy.dx(1)*dx\

      + W.dx(0)*phiz*u*dx + W.dx(1)*phiz*v*dx +
      1/Re*phiz.dx(0)*w.dx(0)*dx + 1/Re*phiz.dx(1)*w.dx(1)*dx +
      1/Re*phiz*pow(kappa,2)*w*dx\

      - psi*u.dx(0)*dx - psi*v.dx(1)*dx)

C =-( phix*kappa*W*u*dx\
      + phiy*kappa*W*v*dx\
      + phiz*kappa*W*w*dx + phiz*kappa*p*dx\
      - psi*kappa*w*dx)

M = phix*u*dx + phiy*v*dx + phiz*w*dx

```

In the code segment above, the lines of the form A have been split for clarity.

- The final line of the UFL file is the definition of the forms, so that the $C++$ header file is produced correctly by the FFC.

```
forms = [A, C, M]
```

Appendice C

Estratto in italiano

In questo lavoro di tesi ci si propone di effettuare un'analisi di stabilità lineare per la corrente in un canale piano, del quale una parete possiede una geometria tipica delle superfici superidrofobiche. Il crescente interesse in questo tipo di superfici è motivato dalla loro capacità di ridurre la resistenza di attrito e dalle loro proprietà di che prevengono la formazione di ghiaccio e che impediscono l'adesione di alghe e altri organismi acquatici, che le rendono adatte per possibili applicazioni soprattutto nel settore navale e aeronautico. Le proprietà delle superfici superidrofobiche sono dovute al mantenimento di bolle di gas all'interno delle asperità della parete solida in modo da ridurre l'area di contatto liquido-solido. A partire dallo studio di Barthlott e Neinhuis [1] sulla foglia di loto, si è osservato che questo particolare stato di bagnabilità della superficie, detto stato di bagnabilità di Cassie, è ottenuto grazie alla sovrapposizione di una rugosità micro-strutturata e una rugosità nano-strutturata. La rugosità microstrutturata può mimare la geometria delle riblets, ovvero microcavità longitudinali della parete solida, per cercare di trarre vantaggio da due meccanismi differenti di riduzione di attrito. Mentre sono già state studiate abbastanza estensivamente le proprietà di riduzione dell'attrito turbolento delle superfici superidrofobiche, altrettanto non si può dire per quanto riguarda i loro effetti sulla stabilità della corrente laminare. Un tale studio deve necessariamente comprendere però, in via preliminare, un approfondimento dei risultati già disponibili riguardo la stabilità delle correnti sopra scanalature longitudinali, ottenuti da Ehrenstein [12] e da Moradi e Floryan [32]. Il principale obiettivo di questo lavoro di tesi è quindi quello di produrre dei risultati che possano costituire una conoscenza di base per il miglioramento delle riblets e la loro eventuale trasformazione in superfici superidrofobiche con il fine di incrementare le loro prestazioni di riduzione di resistenza.

C.1 Formulazione matematica

La dinamica della corrente è stata modellata per mezzo delle equazioni incomprimibili di Navier-Stokes. Sono state imposte le condizioni al contorno di perfetta adesione sulle pareti del canale e delle scanalature, le condizioni di periodicità sui bordi laterali della sezione considerata. Considerando la presenza di una bolla d'aria intrappolata nelle cavità, sull'interfaccia tra i due fluidi sono state imposte le condizioni di continuità delle componenti tangenziali di sforzo e velocità. La condizione sulla componente normale dello sforzo è rappresentata dall'equazione di Young-Laplace che è stata ricavata a partire dal-

l'equilibrio di pressione sia nel caso di approssimazione senza effetti idrostatici sia nel caso completo. Introducendo nelle equazioni di Navier-Stokes le semplificazioni relative alla geometria considerata, si sono ricavate le equazioni del problema di Poisson che descrive il flusso base. Successivamente le equazioni di Navier-Stokes sono state linearizzate attorno alla soluzione del flusso base. Introducendo nelle equazioni linearizzate delle perturbazioni dei campi di velocità e pressione sotto forma di onde, si è giunti alla formulazione del sistema costituente il problema agli autovalori che descrive le caratteristiche di stabilità della corrente esaminata. La formulazione matematica del problema è stata completata con la definizione dei parametri fisici rilevanti e la loro trasformazione in parametri adimensionali tramite il teorema di Buckingham.

C.2 Formulazione numerica

L'equazione di Young-Laplace è stata risolta numericamente tramite un software implementato in *Mathematica* che combina un metodo di shooting, che integra l'equazione adimensionalizzata su metà della larghezza della cavità, e un metodo di Newton per correggere il termine di pressione in modo da ottenere l'angolo di contatto ricercato. Innanzitutto sono state ricavate le formulazioni deboli del problema di Poisson per il flusso base e del sistema costituente il problema agli autovalori. La loro discretizzazione è stata quindi condotta con il metodo degli Elementi Finiti. La soluzione discreta approssimata è cercata in uno spazio finito-dimensionale costituito da funzioni polinomiali in ciascun sottodominio di discretizzazione. Per garantire l'adeguata precisione dei risultati, sono stati scelti dei polinomi di Lagrange del secondo ordine per il campo di velocità e polinomi di Lagrange del primo ordine per il campo di pressione. La procedura di discretizzazione è stata implementata con il pacchetto FEniCS[39] che, tramite *UFL* (Unified Form Language) e l'interfaccia *Dolfin*, permette una semplice gestione dei problemi alle derivate parziali rendendo disponibili un'ampia gamma di tipi diversi di elementi finiti. Il problema agli autovalori è stato infine risolto con la libreria *ARPACK*[27]. Il programma finale è il risultato di una programmazione mista in *C++*, che si interfaccia con FEniCS, e in *Fortran90*, che si interfaccia con *ARPACK*.

C.3 Validazione

Il processo di validazione del codice sviluppato è stato suddiviso in due fasi distinte. La prima fase è consistita nella validazione del solutore del flusso base, sia per il problema con un singolo fluido, acqua, sia nel problema con due fluidi, acqua e aria. La soluzione è stata calcolata per il caso classico della corrente di Poiseuille nel canale piano e confrontata con la soluzione analitica esatta. Successivamente è stata aggiunta una cavità di dimensioni molto grandi rispetto al canale per evidenziare meglio le modifiche del profilo di velocità. La soluzione è stata calcolata con un singolo dominio e poi ricalcolata con due sottodomini. L'uguaglianza delle due soluzioni ha confermato la capacità del codice di gestire due sottodomini distinti. Infine è stato eseguito un test qualitativo con due fluidi differenti. La seconda fase è stata la validazione del solutore del problema agli autovalori. Lo spettro degli autovalori è stato calcolato per una sezione di un canale piano per il numero di Reynolds $Re = 5772$ e il numero d'onda della perturbazione $\kappa = 1.02$, che sono i valori

critici ben noti in letteratura. I risultati sono stati confrontati con quelli forniti da un programma affidabile e già testato che risolve l'equazione di Orr-Sommerfeld [40]. Il calcolo è stato poi ripetuto per diverse larghezze della sezione di canale considerata per indagare l'effetto di quest'ultima. Infine è stata controllata la dipendenza dell'autovalore dominante dai parametri della mesh.

C.4 Risultati e conclusioni

La prima analisi effettuata è stata il tracciamento dell'autovalore dominante per diversi valori di rugosità di parete, ovvero di profondità delle scanalature, e con tutti gli altri parametri fissati. Visualizzando l'autovalore nel piano complesso e tracciando l'andamento del rateo di amplificazione in funzione della rugosità si è concluso che la relazione tra queste grandezze è approssimativamente lineare. Si è quindi proceduto all'analisi di stabilità lineare per scanalature con sezione quadrata e triangolare equilatera. I valori per i parametri di controllo sono stati stimati stabilendo un'analogia tra la corrente nel canale piano e lo strato limite di Blasius sopra una lastra piana. Dal momento che l'applicazione più probabile di queste superfici è in campo navale, lo spessore critico dello strato limite è stato calcolato utilizzando le velocità indicative di diverse tipologie di navi. Si è osservato che le scanalature, sia rettangolari sia triangolari, promuovono l'instabilità della corrente nel canale riducendo il numero di Reynolds critico a seconda della loro dimensione. Inoltre si è potuta osservare l'espansione dell'area della zona instabile delimitata dalle curve neutre nel piano ($Re - \kappa$). Le curve sono state approssimate con un'interpolazione lineare a causa dell'elevato costo computazionale richiesto per ottenere i punti di campionamento. L'analisi delle autofunzioni normalizzate ha evidenziato come i profili della componente perpendicolare alla parete siano molto simili e la presenza di un picco di entità crescente con la dimensione delle scanalature nel profilo della componente lungo la corrente. Quest'ultima è la componente dominante nella zona vicino alle scanalature dove, di conseguenza, le linee di corrente sono praticamente perpendicolari al piano della sezione. La componente trasversale invece è nulla ovunque con l'eccezione dell'area immediatamente vicina agli spigoli delle scanalature. Infine si è effettuata un'analisi qualitativa del flusso base del problema multi-fase considerando la presenza della bolla d'aria. Si è osservato come, per scanalature piccole rispetto al canale, il profilo di velocità non sia modificato sensibilmente.

I risultati ottenuti costituiscono il punto di partenza per l'analisi del problema completo e sono necessari per il proseguimento dello sviluppo di metodi di riduzione di resistenza che sfruttano le proprietà di scanalature longitudinali superidrofobiche.

Bibliography

- [1] W. Barthlott and C. Neinhuis. *Purity of the sacred lotus, or escape from contamination in biological surfaces*. *Planta*, 202:1-8, 1997.
- [2] B. Bhushan and Y. C. Jung. *Natural and biomimetic artificial surfaces for superhydrophobicity, self-cleaning, low adhesion, and drag reduction*. *Progress in Material Science*, 56:1-108, 2011.
- [3] R. Blossey. *Self-cleaning surfaces — virtual realities*. *Nature Materials*, 2(5):301-306, 2003.
- [4] A. V. Boiko, N. V. Klyushnev and Y. M. Nechepurenko. *On stability of Poiseuille flow in grooved channels*, *EPL*, 111:14001, 2015.
- [5] L. B. Boinovich and A. M. Emelyanenko. *Anti-icing potential of superhydrophobic coatings*. *Mendeleev Communications*, 23(1):3-10, 2013.
- [6] J. B. Boreyko, C. H. Baker, C. R. Poley and C. Chen. *Wetting and Dewetting Transitions on Hierarchical Superhydrophobic Surfaces*. *Langmuir*, 27:7502-7509, 2011.
- [7] J. Brassarda, D. K. Sarkarb and J. Perron. *Studies of drag on the nanocomposite superhydrophobic surfaces*. *Applied Surface Science*, 324:525-531, 2015.
- [8] L. Cao, A. K. Jones, V. K. Sikka, J. Wu and D. Gao. *Anti-Icing Superhydrophobic Coatings*. *Langmuir*, 25(21):12444-12448, 2009.
- [9] G. Casalis, B. Lécussan, F. Rogier, M. Salaün and P. Villedieu. *Analyse numérique et équations aux dérivées partielles*. *Formation Supaero*, 2013-2014.
- [10] A. B. D. Cassie and S. Baxter. *Wettability of porous surfaces*. *Transactions of the Faraday Society*, 40:546-551, 1944.
- [11] R. Dufour, N. Saad, J. Carlier, P. Campistron, G. Nassar, M. Toubal, R. Boukherroub, V. Senez, B. Nongaillard and V. Thomy. *Acoustic Tracking of Cassie to Wenzel Wetting Transitions*. *Langmuir*, 29:13129-13134, 2013.
- [12] U. Ehrenstein. *On the linear stability of channel flow over riblets*. *Physics of Fluids*, 8:3194-3196, 1996.
- [13] S. Farhadi, M. Farzaneh and S. A. Kulinich. *Anti-icing performance of superhydrophobic surfaces*. *Applied Surface Science*, 257:6264-6269, 2011.

-
- [14] D. Fratantonio. *Global linear stability analysis of the flow past a superhydrophobic cylinder*. Thesis, Politecnico di Milano, Academic Year 2013-2014.
- [15] L. Gao and T. J. McCarthy. *The “Lotus Effect” Explained: Two Reasons Why Two Length Scales of Topography Are Important*. *Langmuir*, 22:2966-2967, 2006.
- [16] L. Gao and T. J. McCarthy. *Contact Angle Hysteresis Explained*. *Langmuir*, 22:6234-6237, 2006.
- [17] L. Gao and T. J. McCarthy. *Wetting 101*. *Langmuir*, 25(24):14105-14115, 2009.
- [18] X. Gao and L. Jiang. *Biophysics: water-repellent legs of water striders*. *Nature*, 432(7013):36-36, 2004.
- [19] R. García-Mayoral and J. Jiménez. *Drag reduction by riblets*. *Philosophical Transactions of the Royal Society A*, 369:1412-1427, 2011.
- [20] R. García-Mayoral and J. Jiménez. *Hydrodynamic stability and breakdown of the viscous regime over riblets*. *Journal of Fluid Mechanics*, 678:317-347, 2011.
- [21] C. Godrèche and P. Manneville. *Hydrodynamics and Nonlinear Instabilities*. Cambridge University Press, 2009.
- [22] G. R. Grek, V. V. Kozlov and S. V. Titarenko. *An experimental study of the influence of riblets on transition*. *Journal of Fluid Mechanics*, 315:31-49, 1996.
- [23] H. S. Grewal, I. Cho and E. Yoon. *The role of bio-inspired hierarchical structures in wetting*. *Bioninspiration & Biomimetics*, 10, 026009, 2015.
- [24] Y. Kemal Demirel, M. Khorasanchi, O. Turan and A. Incecik. *On the importance of antifouling coatings regarding ship resistance and powering*. Low Carbon Shipping Conference, London, 2013.
- [25] S. S. Latthe, C. Terashima, K. Nakata and A. Fujishima. *Superhydrophobic Surfaces Developed by Mimicking Hierarchical Surface Morphology of Lotus Leaf*. *Molecules*, 19:4256-4283, 2014.
- [26] C. Lee and C. “CJ” Kim. *Maximizing the Giant Liquid Slip on Superhydrophobic Microstructures by Nanostructuring Their Sidewalls*. *Langmuir* 25(21):12812–12818, 2009.
- [27] R. B. Lehoucq, D. C. Sorensen and C. Yang. *ARPACK User’s guide: Solution of Large Scale Eigenvalue Problems with Implicitly Restarted Arnoldi Methods*. version October 8th, 1997.
- [28] P. Luchini and G. Trombetta. *Effects of Riblets upon Flow Stability*. *Applied Scientific Research*, 54:313-321, 1995.
- [29] A. Marmur. *The Lotus Effect: Superhydrophobicity and Metastability*. *Langmuir*, 20:3517-3519, 2004.

- [30] P. Meliga, D. Sipp and J. Chomaz. *Absolute instability in axisymmetric wakes: compressible and density variation effects*. Journal of Fluid Mechanics, 600:373-401, 2008.
- [31] A. Mohammadi, H. V. Moradi and J. M. Floryan. *New instability mode in a grooved channel*. Journal of Fluid Mechanics, 778:691-720, 2015.
- [32] H. V. Moradi and J. M. Floryan. *Stability of flow in a channel with longitudinal grooves*. Journal of Fluid Mechanics, 757:613-648, 2014.
- [33] D. Öner and T. J. McCarthy. *Ultrahydrophobic Surfaces. Effects of Topography Length Scales on Wettability*. Langmuir, 16:7777-7782, 2000.
- [34] N. A. Patankar. *Mimicking the Lotus Effect: Influence of Double Roughness Structures and Slender Pillars*. Langmuir, 20:8209-8213, 2004.
- [35] S. Pedraglio. *Linear stability analysis of FSI problems including large displacements*. Thesis, Politecnico di Milano, Academic Year 2014-2015.
- [36] L. Quartapelle and F. Auteri. *Fluidodinamica incompressibile*. Casa Editrice Ambrosiana, 2013.
- [37] A. Quarteroni. *Modellistica numerica per problemi differenziali*. Springer-Verlag, 2012.
- [38] M. A. Samaha, H. Vahedi Tafreshi and M. Gad-el-Hak. *Superhydrophobic surfaces: From the lotus leaf to the submarine*. Compte Rendu Mécanique, 340:18-34, 2012.
- [39] M. Sandve Alnæs, J. Hake, R. C. Kirby, H. Petter Langtangen, A. Logg and G. N. Wells. *FEniCS manual*. FEniCS Project, version October 31st, 2011.
- [40] P. J. Schmid and D. S. Henningson. *Stability and Transition in Shear Flows*. Springer-Verlag, 2001.
- [41] M. P. Schultz. *Effects of coating roughness and biofouling on ship resistance and powering*. Biofouling, 23(5):331-341, 2007.
- [42] X. Sheng and J. Zhang. *Air layer on superhydrophobic surface underwater*. Colloids and Surfaces A: Physicochemical and Engineering Aspects, 377:374-378, 2011.
- [43] Y. D. Shikhmurzaev. *Capillary Flows with Forming Interfaces*. Taylor & Francis Group, LLC, 2008.
- [44] J. E. Sprittles. *Dynamic wetting/dewetting processes in complex liquid-solid systems*. Ph.D Thesis, Univeristy of Birmingham, 2009.
- [45] U. Tuvshindorj, A. Yildirim, F. E. Ozturk and M. Bayindir. *Robust Cassie State of Wetting in Transparent Superhydrophobic Coatings*. Applied Materials & Interfaces, 6:9680-9688, 2014.
- [46] F. Wang, S. Yu, J. Ou and W. Li. *Anti-icing performance of transparent and superhydrophobic surface under wind action*. Journal of Sol-Gel Science and Technology, 75(3):625-634, 2015.

- [47] J. Wang, Y. Zheng, F. Nie, J. Zhai and L. Jiang. *Air Bubble Bursting Effect of Lotus Leaf*. *Langmuir*, 25(24):14129–14134, 2009.
- [48] G. S. Watson, D. W. Green, L. Schwarzkopf, X. Li, B. W. Cribb, S. Myhra and J. A. Watson. *A gecko skin micro/nano structure – A low adhesion, superhydrophobic, anti-wetting, self-cleaning, biocompatible, antibacterial surface*. *Acta Biomaterialia*, 21:109-122, 2015.
- [49] G. Whyman and E. Bormashenko. *How to Make the Cassie Wetting State Stable?*. *Langmuir*, 27:8171-8176, 2011.
- [50] J. H. Yan, X. B. Zhang, J. Zhao, G. F. Liu, H. G. Cai and Q. M. Pan. *A miniature surface tension-driven robot using spatially elliptical moving legs to mimic a water strider’s locomotion*. *Bioninspiration & Biomimetics*, 10, 046016, 2015.
- [51] S. Zhang, X. Ouyang, J. Li, S. Gao, S. Han, L. Liu and H. Wei. *Underwater Drag-Reducing Effect of Superhydrophobic Submarine Model*. *Langmuir*, 31:587-593, 2015.